Journal of Astrophysics and Astronomy

Subscription Rates
(Effective from 1989)

All countries except India	1 year	3 years	5 years
(Price includes AIR MAIL charges)	US$75	$200	$300
	1 year	10 years	
India	Rs 75	Rs. 400	

All correspondence regarding subscription should be addressed to **The Circulation Department** of the Academy

Editorial Office

Indian Academy of Sciences, C V Raman Avenue,	Telephone (080) 3342546
P B No 8005, Bangalore 560080, India	Telex 0845-2178 ACAD IN
	Telefax 91-80-3346094

Polarization-Mode Separation and the Emission Geometry of Pulsar 0823 + 26: A New Pattern of Pulsar Emission?

Joanna M. Rankin *Physics Department, University of Vermont, Burlington, Vermont 05405 USA*

N. Rathnasree *Raman Research Institute, Bangalore 560 080 India*

Abstract. We explore the detailed polarization behaviour of pulsar 0823 + 26 using the technique of constructing partial 'mode-separated' profiles corresponding to the primary and secondary polarization modes The characteristics of the two polarization modes in this pulsar are particularly interesting, both because they are anything but orthogonal and because the secondary mode exhibits a structure seen neither in the primary mode nor in the total profile The new leading and trailing features in the secondary mode, which appear to represent a conal component pair, are interpreted geometrically on the basis of their width and the associated polarization-angle traverse as an outer cone

If the secondary-mode features are, indeed, an outer cone, then questions about the significance of the pulsar's postcursor component become more pressing. It seems that 0823 + 26 has a very nearly equatorial geometry, in that both magnetic poles and the sightline all fall close to the rotational equator of the star We thus associate the postcursor component with emission along those bundles of field lines which are also equatorial and which continue to have a tangent in the direction of our sight line for a significant portion of the star's rotation cycle. It seems that in all pulsars with postcursor components, this emission follows the core component, and all may thus have equatorial emission geometries No pulsars with precursors in this sense – including the Crab pulsar – are known.

The distribution of power between the primary and secondary modes is very similar at both 430 and 1400 MHz. Our analysis shows that in this pulsar considerable depolarization must be occurring on time scales that are short compared to the time resolution of our observations, which is here some 0 5–1 0 milliseconds. One of the most interesting features of the mode-separated partial profiles is a phase offset between the primary and secondary modes. The secondary-mode 'main pulse' arrives some $1.5 \pm 0.1°$ before the primary-mode one at 430 MHz and some $1.3 \pm 0.1°$ at 21 cm Given that the polar cap has an angular diameter of $3.36°$, we consider whether this is a geometric effect or an effect of differential propagation of the two modes in the inner magnetosphere of the pulsar

Key words. Pulsars—polarization—PSR B0823 + 26.

327

1. Introduction

Pulsar B0823 + 26 is one of the oldest known pulsars, being the first or second pulsar discovered at the Arecibo Observatory (Craft, Lovelace & Sutton 1968) With a period of 531 ms and a spindown of $1\,72 \times 10^{-15}$ sec/sec – yielding a B_{12}/P^2 value of 3.44 – its timing properties could not be more ordinary. However, Backer *et al* (1973) discovered that the pulsar has both an interpulse (IP) and a postcursor (PC) component The pulsar is also relatively close (DM $\sim 19.5\,pc/cm^3$), bright, and exhibits a turnover in its radio-frequency spectrum only below about 50 MHz (Sieber 1973, Izvekova *et al* 1981) For all of these reasons, it has been possible to study it over a remarkably wide interval of frequency On the high end it has been detected at Bonn by Bartel *et al.* (1978) at $14\,8$ GHz, and observations on the low end have been reported at 26 MHz (Phillips & Wolszczan 1992)

Over this enormous frequency range the form of the pulsar's profile changes remarkably little [see Hankins & Rickett (1986) for a series of profiles spanning 135 to 2380 MHz] The MP exhibits a nearly Gaussian-shaped profile at both the very highest and lowest frequencies, only distorted by what is probably interstellar scattering at 26 MHz Its width does change, however, from being practically constant above 1 GHz, to growing with an asymptotic dependence of about $f^{-0\,58}$ below about 300 MHz (Rankin 1983b, hereafter Paper II) The half-power width of the MP, interpolated to 1 GHz, was determined in Rankin (1990, hereafter Paper IV) to be $3.38°$, very close to the $2\,45°/P^{1/2}$ angular diameter of the pulsar's polar cap at the surface of the star

The MP-IP spacing is very close to 180° and could be independent of frequency, although a slight decrease with frequency is also compatible with the observations (Hankins & Fowler 1986). The MP-PC separation, however, *increases* monotonically with frequency between about 400 and 2400 MHz as $f^{0\,08}$ (Hankins & Fowler 1986), and Arecibo 130-MHz observations further confirm this behaviour (Hankins & Rankin 1994) The relative intensity of the IP is strongest at 400 MHz, with a peak intensity of just under 1 per cent that of the MP, and decreases steadily at both higher and lower frequencies The PC, in turn, is somewhat stronger than the IP, being about 3 per cent of the MP at 400 MHz At frequencies above about 400 MHz the relative intensities of the PC and IP fall off at about the same rate ($f^{\sim -1}$) Below 400 MHz, the relative intensity of the IP decreases very rapidly, whereas that of the PC increases, at least to about 100 MHz, though far less steeply than at higher frequencies (Hankins & Rankin 1994).

Full period, average polarimetry has been published for pulsar 0823 + 26 at 430 MHz (Rankin & Benson 1981), 1400 MHz (Rankin *et al* 1989, Blaskiewicz *et al* 1991), and $10\,55$ GHz (Xilouris *et al.* 1995), all but the last of which also includes some information about the PC and/or the IP Individual-pulse polarimetric studies have been carried out at 430 MHz (Rankin *et al.* 1974; Backer & Rankin 1980) and 1400 MHz (Stinebring *et al.* 1984) The aggregate linear polarization is also Gaussian in form, occupies the central portion of the profile, and is never large—going from perhaps 35% at 430 MHz, to 25% at 1400 MHz, and 5% at $10\,55$ GHz. The edges of the profile are thus almost completely depolarized, but slightly more so on the leading than the trailing edge so that the residual linear 'component' looks a little delayed relative to the total-power profile

A small amount of circular polarization is also observed in this pulsar's average profile, usually less than 5%. The published profiles often show a little left-hand (positive) circular on the leading edge, changing to a little more right-hand (negative) on the trailing. However, other unpublished observations suggest considerable variation around this general configuration.

With not only an MP, but an IP and PC as well, the linear polarization angle (PA) can be measured over a large part of the star's rotation cycle. Backer & Rankin (1980), however, found the linear PA behaviour of this pulsar to be unusually complex, apparently requiring two different angle systems. Using the information in Rankin & Benson (and correcting for '90° flips' at about − 8 and + 12°), Lyne & Manchester (1988) have obtained a value of 80° for α, the angle between the magnetic and rotation axes of the star, by fitting the single-vector model (Radhakrishnan & Cooke 1969, Komesaroff 1970) to the PA data Better resolved observations are to be found in Rankin *et al* (1989) and Blaskiewicz *et al* (1991), and the rapid traverse of the PA near the peak of the profile can be seen clearly The latter study (also correcting for a '90° flip' at about 170° in the 430-MHz observation) obtained values of $79° \pm 1°$ and $91° \pm 600°$ at 430 and 1418 MHz, respectively

Fluctuation-spectral analysis yields a 'weak, broad feature in the range of 0 05 to $0\,23c/P_1$ with a constant strength of 0 35 . The measured center frequency is $0\,14c/P_1$' (Backer 1973). In other studies (Taylor & Huguenin 1969; Lang 1969), the feature appeared stronger and at a frequency of 0 18 to $0.20c/P_1$ We note here [and Rankin (1986; hereafter Paper III) did not[1]] that there is considerable fluctuation power at frequencies below $0\,10c/P_1$, suggesting in the terms of Paper III both core and conal-associated fluctuations. Finally, there is no published evidence for null pulses, although the limit of $\leqslant 5\%$ (Ritchings 1976) is not a very strong one.

As regards classification, pulsar 0823 + 26 has had a chequered history In Paper III it was seen as a conal double (D) pulsar in an attempt to make sense of the MP and PC as a conal component pair The spacing between the two components was uncomfortably large, and there was some antisymmetric MP circular polarization, but the lack of MP conal 'outriders' at high frequency tilted toward the conal side The growing weight of evidence regarding core-component geometry in Paper IV shifted 0823 + 26 into the core-single (S_t) class. Its MP width was exactly what would be expected for a core component in a pulsar with a nearly orthogonal magnetic geometry, a geometry which seemed highly compatible with its observed interpulse. Its rather high B_{12}/P^2 also seemed to suggest that it is not a cone-dominated pulsar And viewing the MP as primarily a core component was more compatible with its polarization characteristics This classification left only two nagging questions a) In a pulsar which can be observed to such high frequencies, where are the high frequency conal 'outriders'? And b) If the MP is a core component, how are we now to interpret the PC?

These questions are the starting point for this paper In the next section we introduce the observations considered in our analysis, and §3 begins our discussion of the polarization structure of pulsar 0823 + 26's profile. In §4 we consider mode-separation techniques and their application to pulsar 0823 + 26, §5–§7 explore the pulsar's main-pulse, postcursor, and interpulse emission geometry, respectively, §8 then returns to the polarization-modal structure of the main-pulse emission, §9 assesses the significance of the displaced modal emission, and §10 provides a summary and the conclusions of the paper.

2. Observations

The single-pulse observations used in our analysis below come from three programs carried out at the Arecibo Observatory over a long period of time. The older 430-MHz

observations were carried out in January 1974 with a single-channel adding polarimeter of 500-kHz bandwidth and 1.0-ms integration time, giving a nominal time resolution of about 0 7° longitude. The polarimetry scheme is described in Rankin *et al* (1975); no attempt was made to correct the Stokes parameters for the known 0 25% cross-coupling in the feed, which can produce spurious circular polarization at a nominal level of about 10% of the linear

The older 1400-MHz observations were carried out in October 1981, again with a single-channel, adding polarimeter Here the bandwidth was 10 MHz and time constant 0 66 ms, giving an effective resolution of about 0.5° A serious effort was made for the first time to correct the measured Stokes parameters for instrumental distortion using the 'orthogonal' approximation described by Stinebring *et al.* (1984)

The newer observations at 430 and 1404 MHz were made in a single observing session in October 1992, the 430 MHz on the morning of the 20th and the 21 cm on the morning of the 15th Both used a special program to gate the 40-MHz correlator, and the basic data recorded at the telescope were the ACFs and CCFs of the right- and left-hand channel voltages. The higher frequency observations used a 20-MHz BW and the lower a 10-MHz BW, and the retention of 32 lags in both cases reduced dispersion delay across the bandpass to negligible levels The resolution was then essentially the correlator dump time, which was 506 μs or 0.34° The Arecibo 40-MHz correlator is described by Hagan (1987) and the observing software by Perillat (1988, 1992) The measured correlation functions were scaled, 3-level sampling corrected, and Fourier transformed to produce raw Stokes parameters, which were in turn corrected (channel by channel) for dispersion, Faraday rotation, instrumental delays, and all of the known feed imperfections as determined by full-sky tracks of pulsar 1929 + 10 and other sources. During the course of our analysis, we discovered that the instrumental polarization is highly frequency dependent, particularly at 430 MHz, therefore, the most recent observations represent some of the best calibrated ever made at the Arecibo Observatory The instrumental details will be described in a forthcoming paper (Rankin, Rathnasree & Xilouris 1996)

3. The polarization structure of pulsar 0823 + 26's profile

Figures 1a–c give a collection of profile and polarization-angle density plots for both 430 and 1404 MHz Notice the difference in the longitude scales, at 430 MHz the entire MP-PC portion of the rotation cycle of the pulsar is included, whereas at 1404 MHz only the MP region is plotted We should say that the lower panels are not really grey-scale plots; each point represents the polarization of an actual measured sample falling above a threshold of a few standard deviations in the off-pulse noise. The regions of greatest primary-mode power are thus 'over exposed' in the process of plotting enough individual pulses to explore the overall space represented by the diagram.

These plots are interesting and remarkably complex. Let us first consider the simpler 1404-MHz diagram (Fig. 1c), wherein it is clear that there are two distinct modes and that these have very different PA traverses One can also see this, both in Stinebring *et al.*'s Fig 5 and in Gil *et al*'s Fig 2 – we are dealing here with the same data – but considerably less clearly owing to the details of plotting or analysis. The darker primary mode has a slope of 14–15°/°, and the less prominent secondary mode a slope just about twice this What is most striking is that the two modes are anything but orthogonal, and

near the trailing edge of the profile (near + 3° longitude) appear to be separated by barely 45°. Lest anyone wish to attribute this to instrumental causes, we have another, shorter 1404-MHz sequence from our 1992 October observations which shows an identical behaviour. Other than this it is interesting to again note the minor peak in the linear power as well as the larger one, which trails the profile center. Also one can see, both how narrow the longitude interval over which the PA can be traced is and how poorly it often traces the PA of the primary-mode power.

We see a good deal more in the 430-MHz figures (Figs. 1a and b), and it is noteworthy how much more similar the PA density plots are than the average position-angle behaviour. The primary and secondary modes are again prominent in the center of the profile, and their measured slopes are nearly the same as at 21 cm.
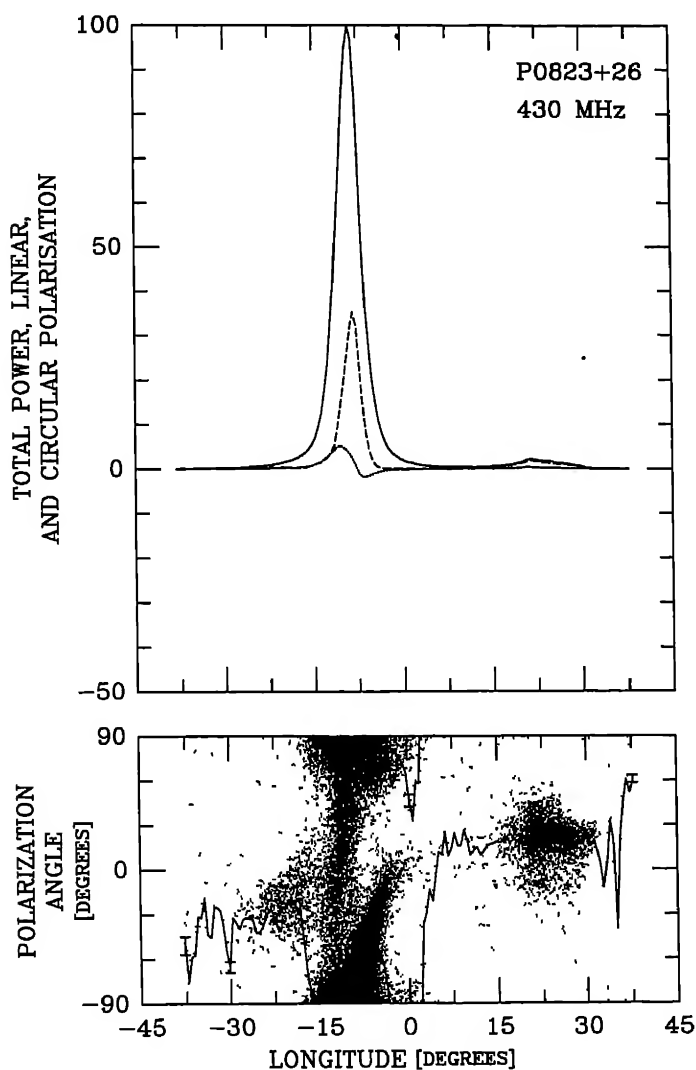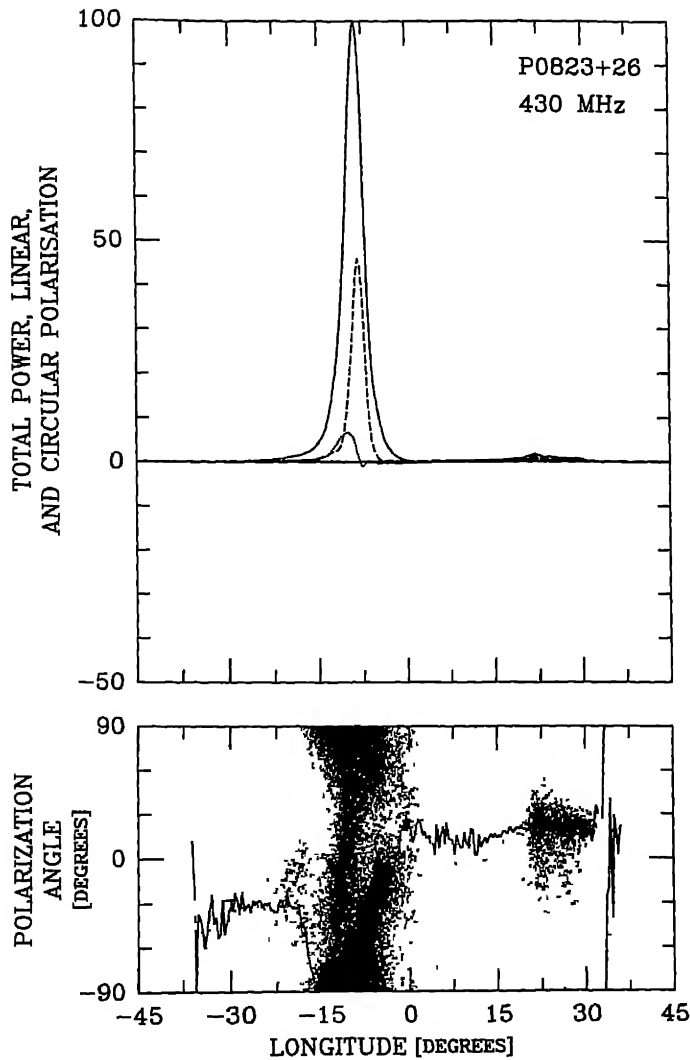

Figure 1 (a).

Figure 1(b).

Again there is rather little aggregate linearly polarized power outside the MP center, but owing to the greater intensity of the pulsar at 430 MHz, individual samples with sufficient power to define the PA can be found over nearly a quarter of the rotation cycle of the pulsar The principal primary-mode 'blotch' begins at about $-12°$ longitude and $\pm 90°$ PA and rotates positively through about $90°$, also making the largest contribution to the overall linearly polarized power, L Several other 'patches' of significant linear polarization can also be seen Note the area associated with the postcursor, another on the extreme leading edge of the profile (which can also be seen in L), and a third, secondary-mode 'blotch' which begins at about $-14°$ longitude and $-45°$ PA, again rotating positively through $90°$ At this point this last traverse appears to flatten off adjacent to the principle primary-mode 'blotch', and its power is conflated with the main primary-mode 'blotch' in L.
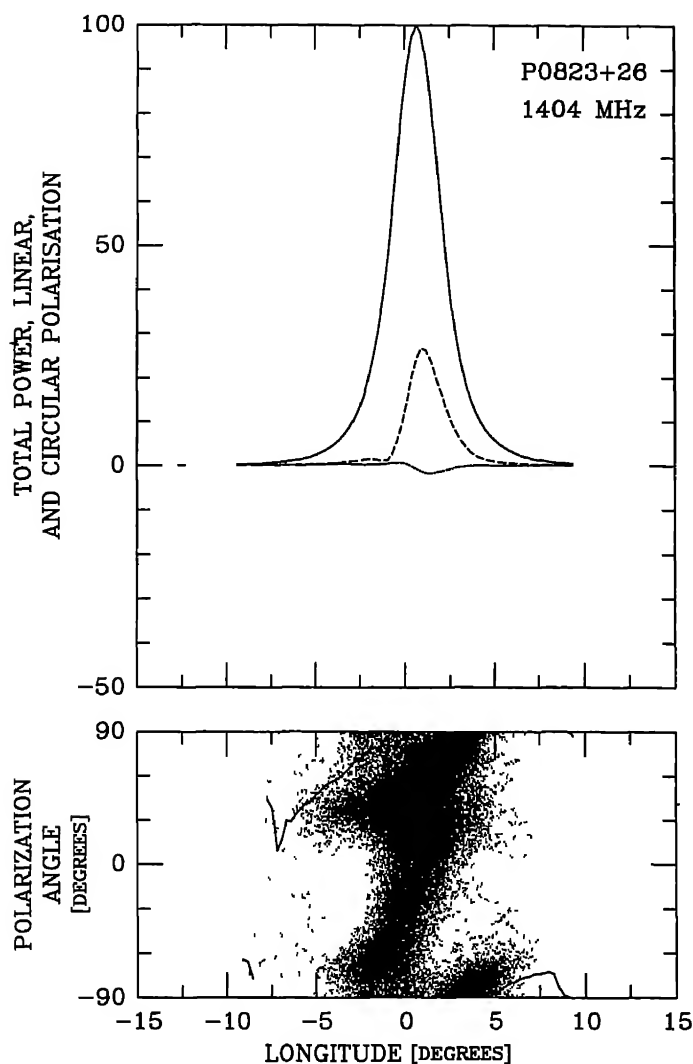
Figure 1(c).

Figure 1 (a–c). Average profiles and polarization-angle density plots for pulsar 0823 + 26 at 430 MHz (a, b), and 1404 MHz (c). The upper panel plots Stokes parameter I, the total power (solid curve), $L = (Q^2 + U^2)^{1/2}$, the total linear polarization (dashed curve), and V, the circular polarization (dotted curve) The lower panel gives the polarization position angle of each sample falling above some threshold (see text), and the average position angle is also plotted, where defined, as a solid curve The 430-MHz observations were recorded on 6th January 1974 and 20th October 1992 and represent 3194 and 1800 pulses, respectively. The 1404-MHz observation was made on 9th October 1982 and represents 6200 pulses

Again it is interesting to consider how different the overall linear PA traverse is in the two 430-MHz observations, given the striking similarity of their modal-power distributions. It does appear that the polarization of this pulsar shows significant time variability; the differences in fractional linear polarization, PA traverse, and the entirely different form of the circular are quite typical of other (not shown) observations in our
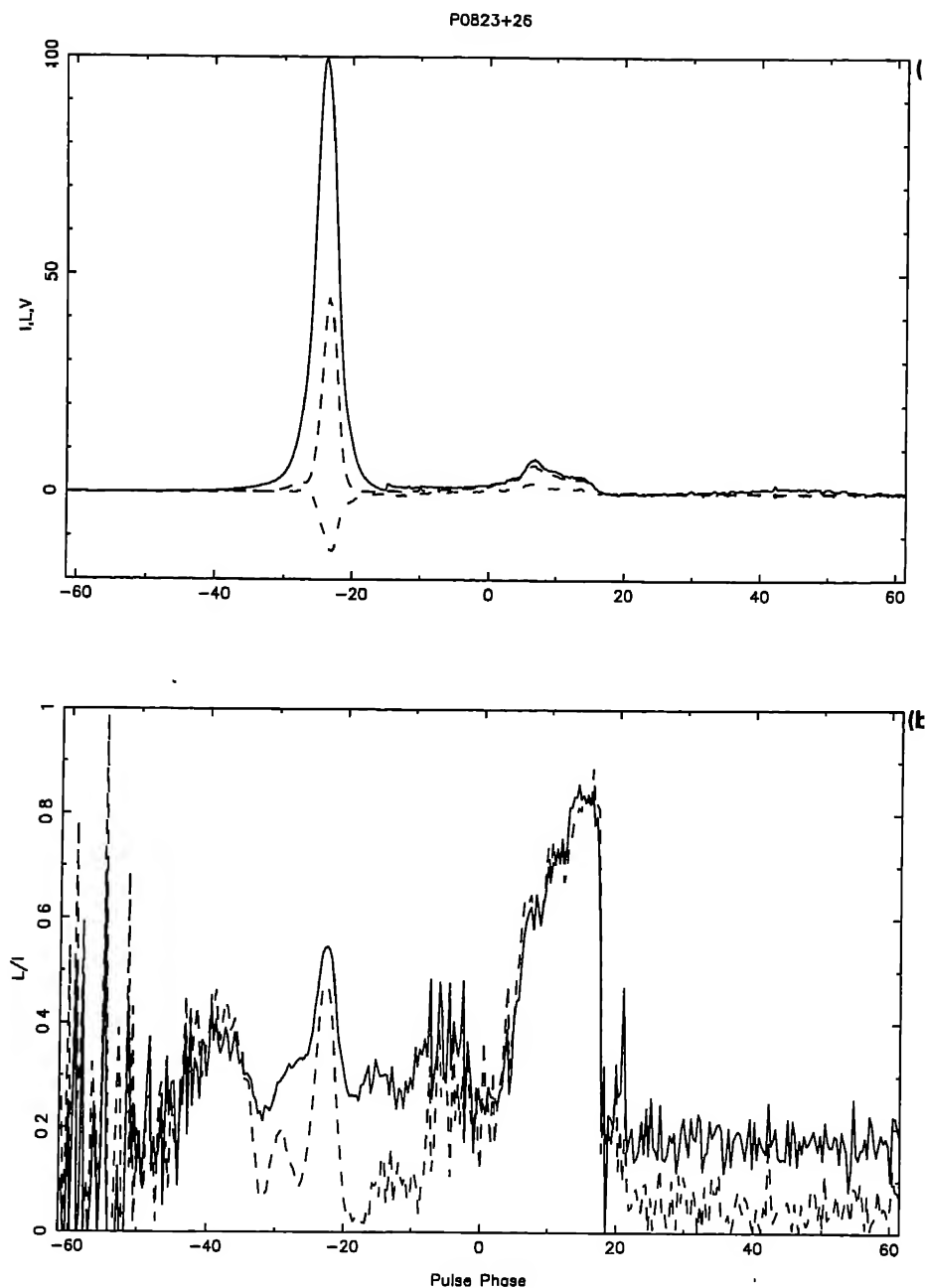
P0823+26

Figure 2. (a) Average profile of pulsar 0823 + 26 at 430 MHz as in Fig 1b At longitudes larger than − 15° all the quantities *I*, *L* and *V* have been multiplied by a factor of 5 to show the region o the postcursor more clearly. (b) The fractional linear polarization, ⟨*L/I*⟩ (solid curve) anc ⟨*L*⟩/⟨*I*⟩ (dashed curve). In both the curves the averages have been corrected for statistica. polarization In regions of low intensity, the degree of polarization could be quite undefined and oscillating between high and low values as in the left hand portion of the figure

P0823+26

Figure 3. Pulse intensity histogram (solid line) for pulsar 0823 + 26 at 430 MHz corresponding to the October 1992 observations in Fig 1b. The dashed line shows the intensity histogram obtained from the noise window, which is normalized to 142 pulses.

possession. It is quite conceivable that this pulsar exhibits some yet unrecognize mode-switching phenomenon (and of course this would be particularly difficult t identify in a pulsar with a single profile).

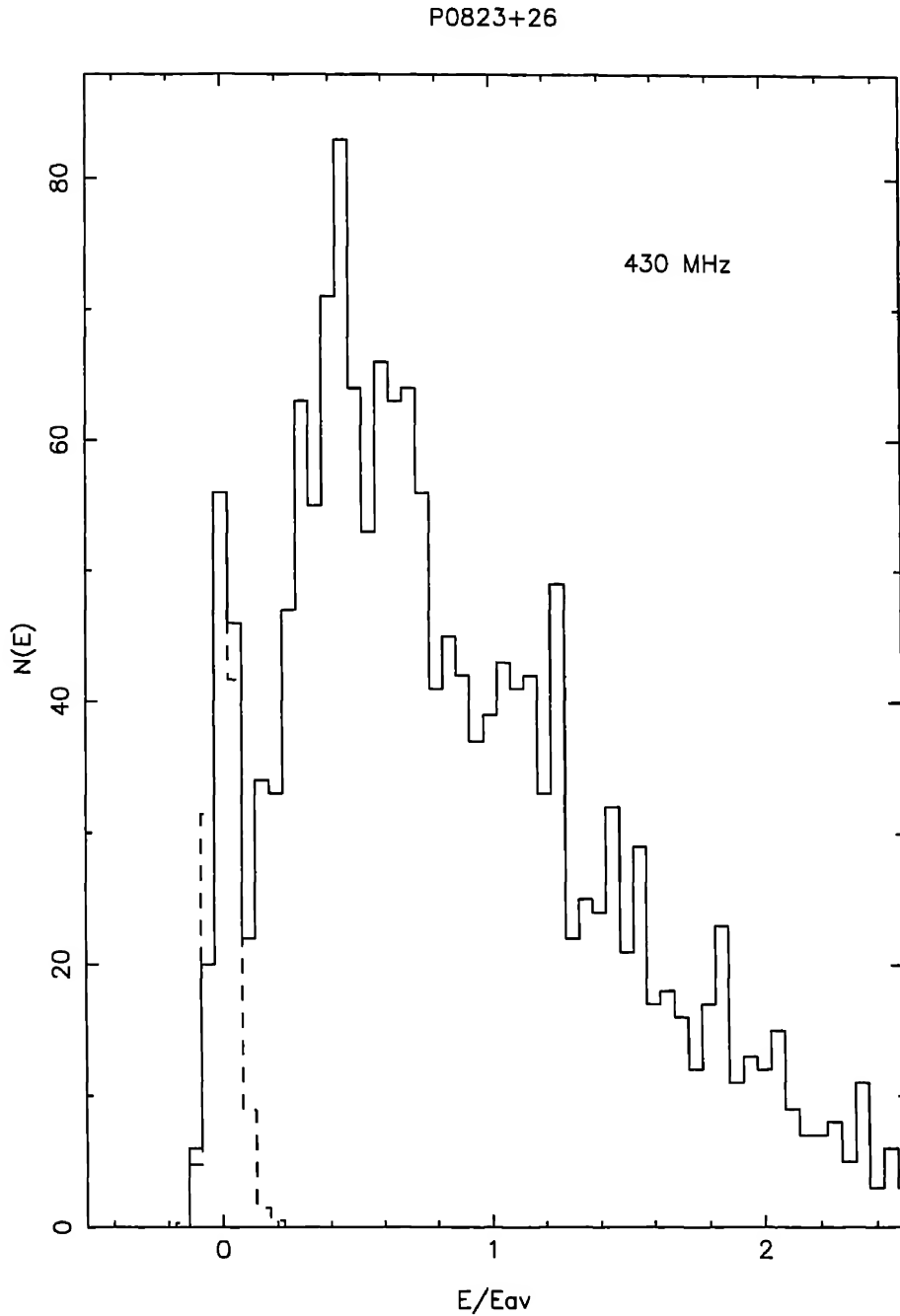Turning now to Fig 2, we again see the 430-MHz profile although displayed a slightly different manner than in Fig. 1b In the top panel, at all longitudes later tha $-15°$, I, L and V have been multiplied by a factor of 5, so that the postcursor ar interpulse windows can be seen more clearly. The information in the bottom panel ha been obtained after rejecting sample by sample all data points with $I <$ twice the σ the noise window Here, we plot the fractional linear polarization, first in the usu manner by averaging Stokes parameters Q and U (dashed curve) and, second, t aggregating the linearly polarized power irrespective of the PA (solid curve). Under th MP peak the latter is larger than the former as expected, but generally only by son 10% or so, arguing that most of the depolarization is occurring on time scales sho compared to the 500-μs resolution of the observation However, the amount depolarization taking place over time-scales larger than a period (which amounts to th difference between the two curves in the bottom panel) is considerably greater in th wings of the MP profile This suggests that different processes and time scales depolarization are operative in the MP wings, and overall, that the MP has a composi character. We will return to this issue below. Finally, note that exactly the opposite true for the PC; the two linear polarization measures are identical within the nois indicating that virtually no depolarization is occurring on time scales shorter than th sampling interval

Finally, Fig. 3 gives a 430-MHz, pulse-intensity histogram, scaled to the averag profile intensity to show the range of fluctuation (solid line) A similar histogra (dashed line) for the noise window has been normalized so that the zero-intensity bi coincide Interestingly, the pulse-intensity histogram is bi-modal, and the distin zero-energy peak has a width almost exactly equal to that of the noise distribution T fraction of null pulses from this analysis is $6 4 \pm 0 8\%$ as compared with the upper lin of 5% from Ritchings' (1976) study

4. Polarization-mode separation

Several efforts have been made to separate the polarization modes and to reconstru the two modal pulse profiles Cordes *et al.* (1978) first carried out this analysis for PS $2020+28$, and Rankin *et al.* (1988) and Rankin (1988) then applied it to pulsa $1737+13$ and 1604–00, respectively. About this time Gil *et al.* (1991) develop a different polarization-mode fitting technique and applied it first to $0823+$ observations at 1404 MHz and then to observations of a small group of other pulsars the same frequency (Gil *et al* 1992). The first technique relies on a model of t polarization angle as a function of longitude, usually the 'single-vector' model given Radhakrishnan & Cooke (1969) and extended by Komesaroff (1970), whereas t second uses an algorithm which partitions the aggregate polarization angles into tv groups statistically, longitude by longitude.

The two techniques are complementary in that, both have their strengths ai weaknesses The first technique is more sensitive and 'stable', but risks giving the fa' appearance that the modal PAs follow the model in regions of longitude where t modal power is negligible. Gil's technique, on the other hand, has the advantage

being model-independent, but requires significant power in both modes at each longitude and easily loses track of the identity of the modes when they are discontinuous Our study of 0823 + 26 uses only the first technique, because we were unable to obtain sensible results using Gil's technique on the 430-MHz observations.

The question then immediately arises regarding how this overall polarization PA behaviour should be interpreted At 430 MHz, beginning with the primary mode, we see a positive, about 120° rotation of the PA which seems to terminate at around the PA of the PC; by this interpretation, however, there is no appreciable primary-mode power at longitudes earlier than that of the primary-mode 'blob'—a circumstance which is also largely true, we note, at 21 cm What power there is at earlier longitudes is reasonably associated with the secondary mode, although the leading-edge patch seems somewhat disconnected from the main area where the secondary mode rotates
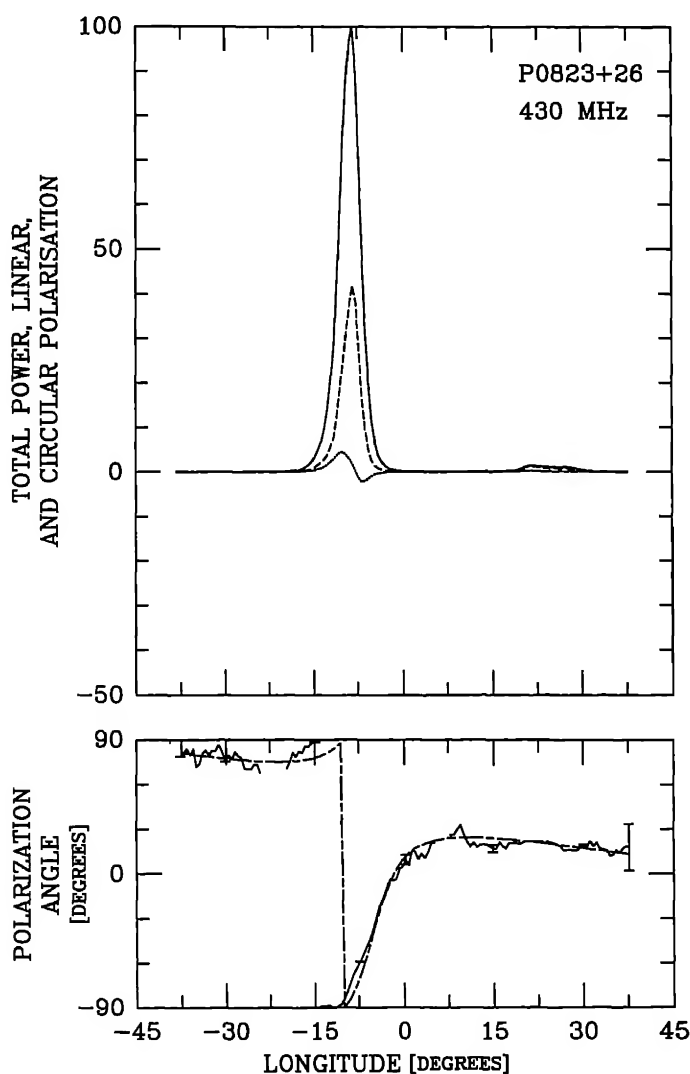
Figure 4(a).
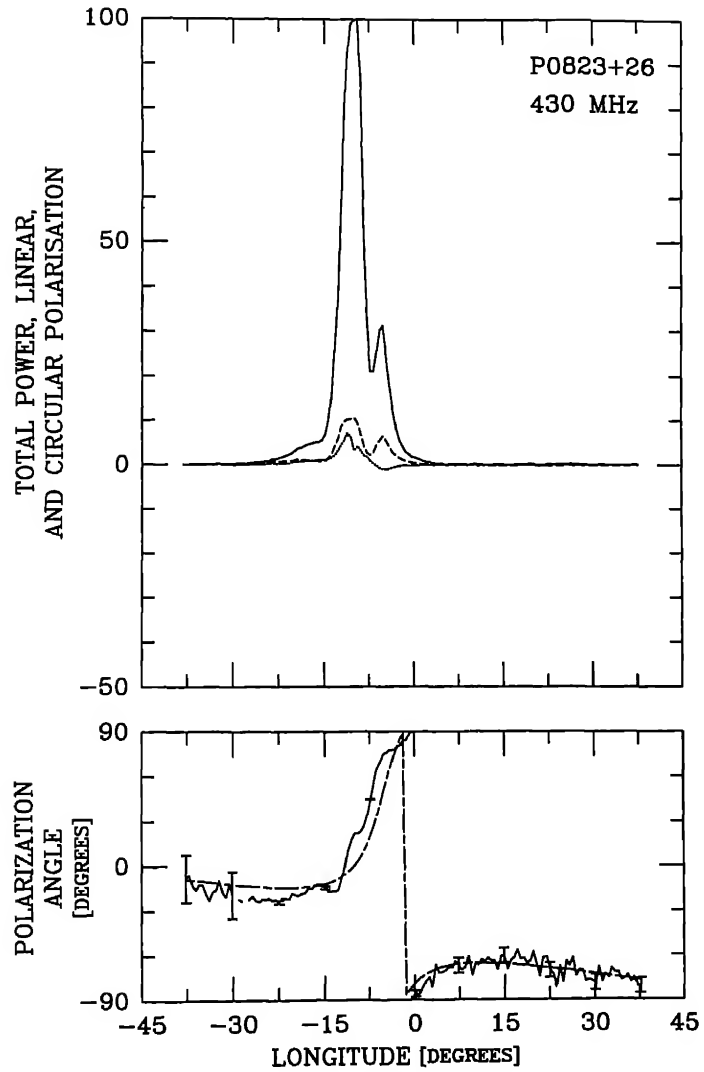
Figure 4(b).

most rapidly. It furthermore seems that the primary and secondary mode barely distinguishable in the 'patch' near − 5 to − 10° longitude and Conveniently − despite the uncorrected ionospheric Faraday rotation − MHz observations have nearly the same PA origin.

Using this interpretation of the polarization-mode behaviour, we can separate the composite profiles into their constituent polarization-mod profiles. In Rankın *et al* (1988) we found a convenient representation of vector model

$$\chi = \chi_0 + \tan^{-1}\frac{\sin(\phi - \phi_0)}{A - \left(A - \frac{1}{R}\right)\cos(\phi - \phi_0)},$$
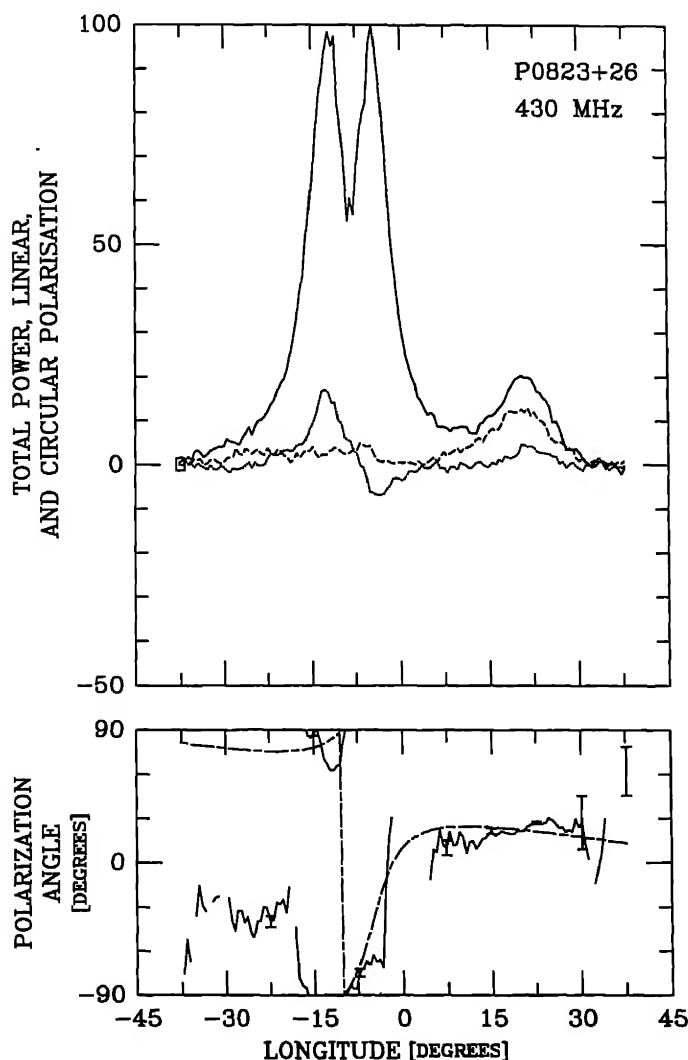
Figure 4(c).

Figure 4(a–c). Partial, 'mode-separated' profiles for pulsar 0823 + 26 at 430-MHz on 6th January 1974, (a) primary-mode, (b) secondary-mode, and (c) residual profiles. The lower panels in these figures give the PA traverses corresponding to the two modes, and the model PA is overplotted as a dashed curve

where χ is the polarization angle, ϕ the longitude, $R = \left|\dfrac{d\chi}{d\phi}\right|_{max} = \sin\alpha/\sin\beta$ the maximum PA rate, and A a constant which can be computed from the total PA traverse χ_c between reference longitudes $\pm\phi_c$ as

$$A = \frac{\sin\phi_c/\tan\frac{1}{2}\chi_c - \cos\phi_c/|R|}{1 - \cos\phi_c}$$

and which is formally equal to $\sin\zeta/\tan\alpha$, where α and ζ are the angles that the magnetic axis and the sight line make with the rotation axis, respectively

Now taking the center of the primary-mode PA traverse at about $-4°$ 1·
a PA of $-40°$, R as about $+15°/°$, and computing A from a total traverse
$\pm 30°$ longitude, we proceed to construct partial ('mode-separated') p·
sponding to the primary and secondary modes of $0823 + 26$ The stream ·
the individual pulses is compared with a threshold – the criteria being **a)**
total linear polarization exceeds twice the off-pulse baseline noise level, an
the computed PA falls within $\pm 45°$ of the model PA – and accumulated ir
partial profile 'bins' accordingly The first, 'primary-mode' partial profil·
those samples which both exceeded the noise threshold and had PAs lying
of the Poincaré sphere closest to the Stokes vector representing the m·
second those in the other hemisphere, and the third those which did not m
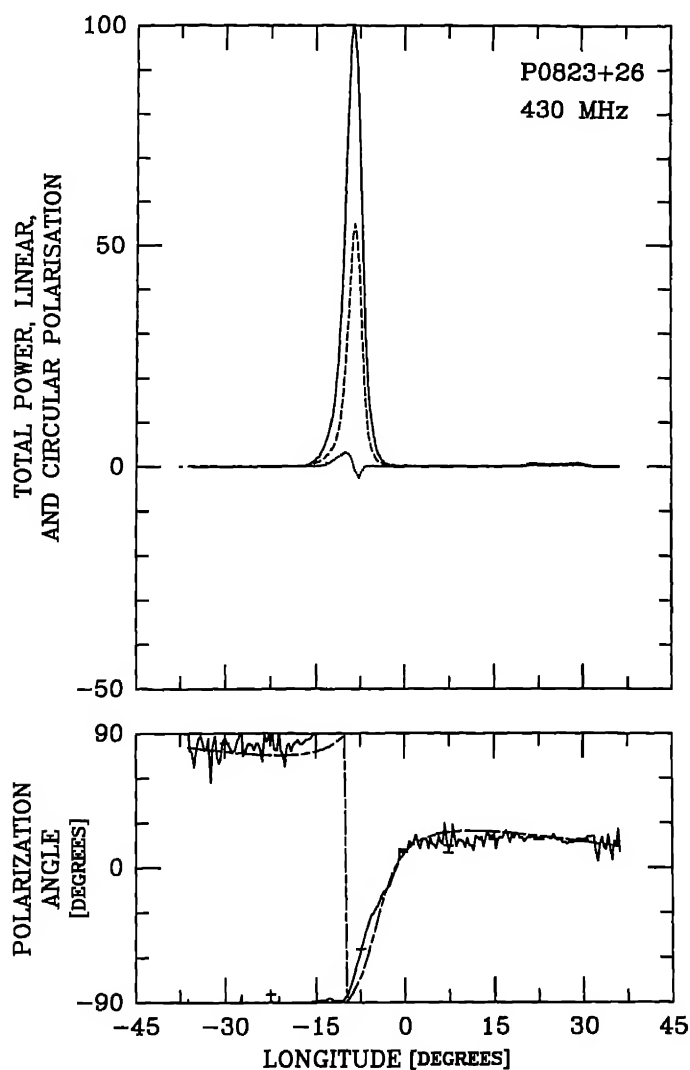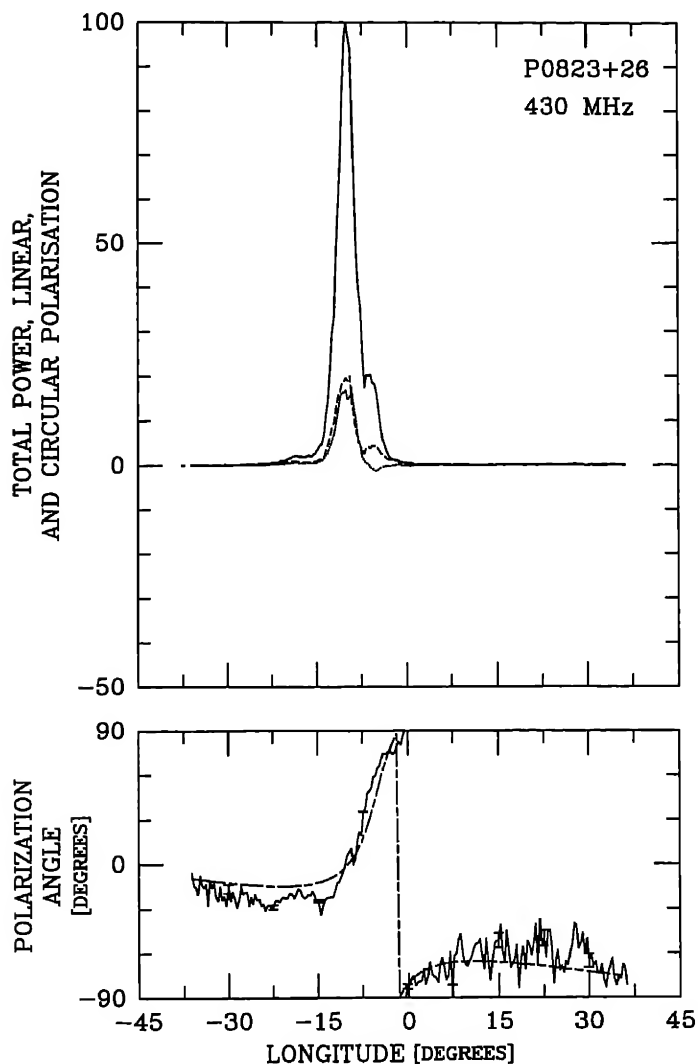
Figure 5(a).

Figure 5(b).

threshold. The 'mode-separated' profiles at 430 MHz computed from the earlier 1974 and the later 1992 observations are given in Figs. 4 and 5, respectively.

Turning first to the earlier observations in Fig 4, we see that the primary-mode partial profile (Fig 4a) greatly resembles the total profile in Fig. 1a. The linear polarization is only a little greater, the circular polarization almost identical, only we now have an MP which is slightly narrower with its linear polarization more symmetrically positioned in its center. With a noise threshold of about 2-σ[†] only about 9.9% of

---

[†]The precise off-pulse noise level is difficult to determine in the older observations as the noise-window data is no longer readily available, comparison with the 1992 observations – where the noise levels were accurately determined – however, shows that our estimate of σ is not far in error
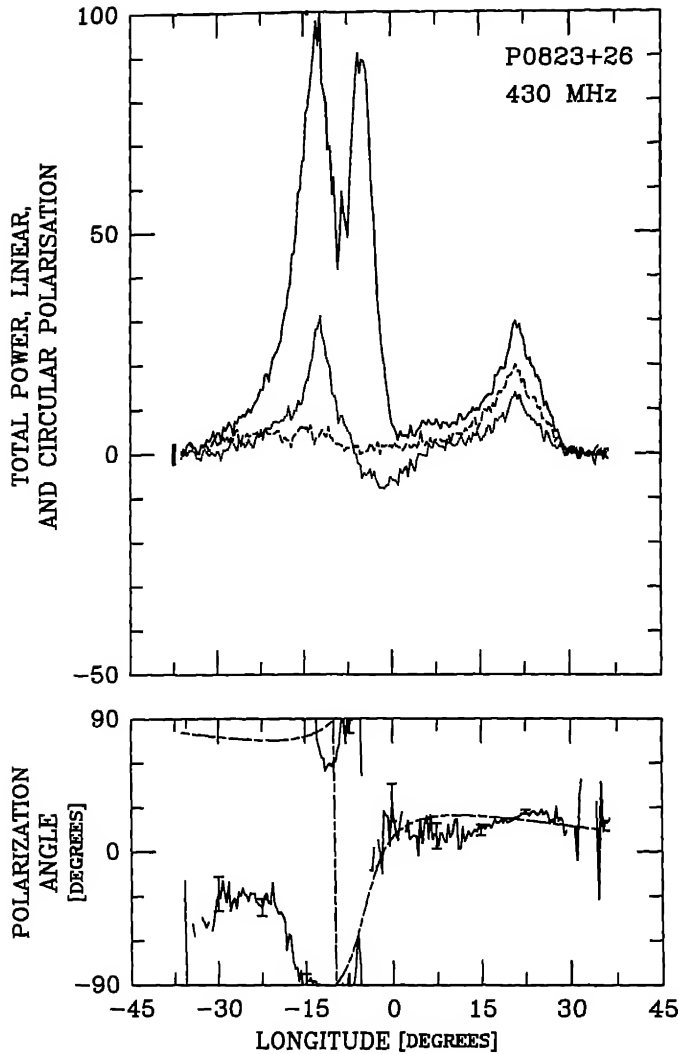
Figure 5(c).

Figure 5(a–c). Partial, 'mode-separated' profiles for pulsar 0823 + 26 at 430-MHz on October 1992 as in Fig 4

the samples accrue to the primary-mode partial profile, but these carry nearly 67.9'
the total power The only big change is in the PA traverse, which now more ne
conforms to what is expected on the basis of the single-vector model. Part of this i
artefact of the 'mode-separation' procedure; in regions of longitude where prim
mode L is small compared to the noise level – such as the 'baseline' region on
MP – the precise value of the model PA does affect the PA of the modal partial prc
However, in regions where any significant linear power is present, the partial pre
PAs are only very weakly dependent upon the PA model We also note that the P
most prominent in the primary mode, and its linear polarization appears n
complete because weakly polarized samples have not reached the noise threshold le

It is the secondary-mode profile in Fig. 4b which holds the surprises, though it consists of only 4.1% of the samples and 17 7% of the power. This profile shows a more complex structure, both in L and in total power. Were it a complete profile, we would immediately say it had a triple form The polarization is low, but not insignificant, throughout its entire extent, here we see much less severely depolarized 'wings' as compared with the primary-mode profile Part of this is again an artefact of the separation in that, weakly polarized samples in the wings will have a much reduced chance of meeting the threshold in L; however, as we shall see below, this is not the whole story. Again, the PA traverse is 'rationalized', but it is also well defined over most of its extent by 'patches' of modal power. Note that here we see a flattening of the steep traverse after about $-15°$ longitude as compared to the density plot in Fig. 1 because the PA model cannot track both the primary- and secondary-mode traverses in this region simultaneously

Returning now to the form of the secondary-mode profile, let us begin to ask what interpretation should be made of it The first thing to point out is that the primary- and secondary-mode profiles are not coincident in time The two partial profiles have virtually identical half widths (fwhm) at 4.1°, however, the secondary-mode one arrives earlier by about 1.5°. Then there is the question of the 'outriders'! The leading feature can be traced to the isolated 'patch' at about $-23°$ longitude and $-30°$ PA in Fig. 1b which we pointed out earlier. The trailing feature is more difficult to see as it is below and to the right of – but immediately adjacent to – the principle primary-mode 'patch' at -9 to $-14°$ longitude and $\leqslant 90°$ PA. Note the asymmetry of the primary-mode feature, and the additional emission to the bottom right of it Note also that the minimum between the 'MP' and the trailing feature in the secondary-mode partial profile falls just after $-7.5°$ longitude—and that there is a slight 'cusp' in the density distribution in Fig. 1b which apparently corresponds to it Here the PA model used in the mode separation is sensitive to the position of the modal boundary, so that it effectively discriminates between the above primary-mode 'patch' and the secondary-mode power immediately adjacent to it. This criticality stems from the close separation in angle of the two modes in this region

Readers may also question whether the secondary-mode features are in some manner generated by the mode-separation procedure After all, most of the samples (86.0%) and a significant amount of the power (14.4%) in the original pulse sequence are not represented in Figs 4(a and b) and accrue to the residual profile in Fig. 4c In order to explore this possibility, partial profiles were computed holding the model PA parameters constant, but progressively reducing the noise threshold from 2σ to 1σ, 0σ, and even -1σ. Eventually, with the latter, the noise threshold becomes moot and all samples accrue to either one or the other modal partial profiles. The meaningless division of ever more noise-dominated samples into one or the other 'modal profiles' produces statistical travesties (total linear polarization $L > I$), but the form, boundaries, and relative amplitudes of the secondary-mode 'MP' and its 'outriders' remain intact. Therefore, we cannot trace their origin to an artefact of the partial-profile construction process If there is an error, it must be in the interpretation of the primary- and secondary-mode related 'patches' in Fig. 1.

Turning now to the more recent 1992 observations, we see a very similar story overall. The pulsar appears to have been about 4 times weaker on the latter occasion, but 5 times the bandwidth and much better receivers were also being used in 1992. It is worth returning to Fig. 1 and again carefully comparing the two 430-MHz observations. The

MP in the 1992 observation is significantly narrower than that in the earlier one (3.7° versus 4 5°), owing perhaps to improved resolution. This seems to accentuate the asymmetry of L within the overall I envelope, and probably accounts in part for its larger relative amplitude as well. Very different, however, is the circular polarization; while the 1974 observation shows a small amount (< 5%) which varies antisymmetrically across the MP, the 1992 profile has nearly 15% RCP with only a hint of a sense reversal.

The primary-mode, secondary-mode, and residual partial profiles are given in Figs. 5(a–c), respectively Little needs be said about the former except to note its narrowness (now about 3.2° fwhm), its increased linear symmetry as compared with the total profile, its nearly identical circular polarization, and of course its more orderly PA
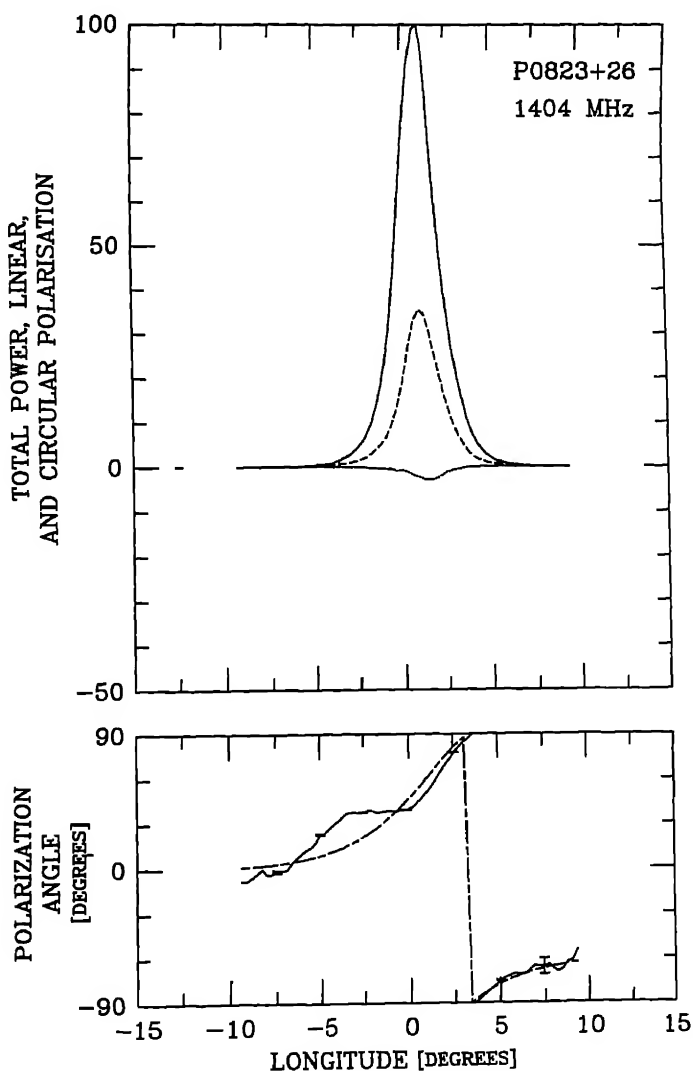
Figure 6(a).
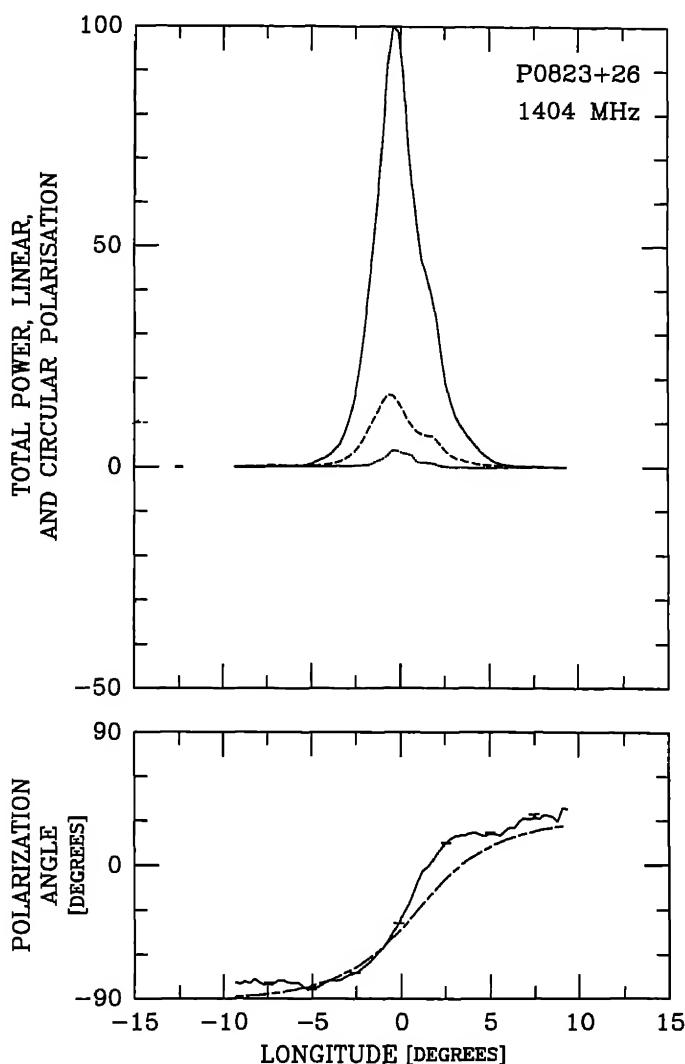
Figure 6(b).

traverse With a 2-σ threshold, it here represents 10 1% of the samples and 68.9% of the total power in the individual-pulse sequence.

The secondary-mode profile in Fig. 5(b) again has a tripartite form, both in I and in total linear, L—although the minimum between the middle and trailing features is less well resolved The fractional linear polarization seems to be a little larger than in the earlier observation. However, please note that the secondary-mode circular is very comparable, notwithstanding the very different primary-mode circular (again suggesting that a 'mode-changing' phenomenon is active in the pulsar which changes, over time, the relative proportions of the two polarization modes or their overall polarization states) The fwhm of the 'MP' is here about 3.3°, and it again leads the primary-mode one by almost exactly 1.5°. Here the secondary-mode
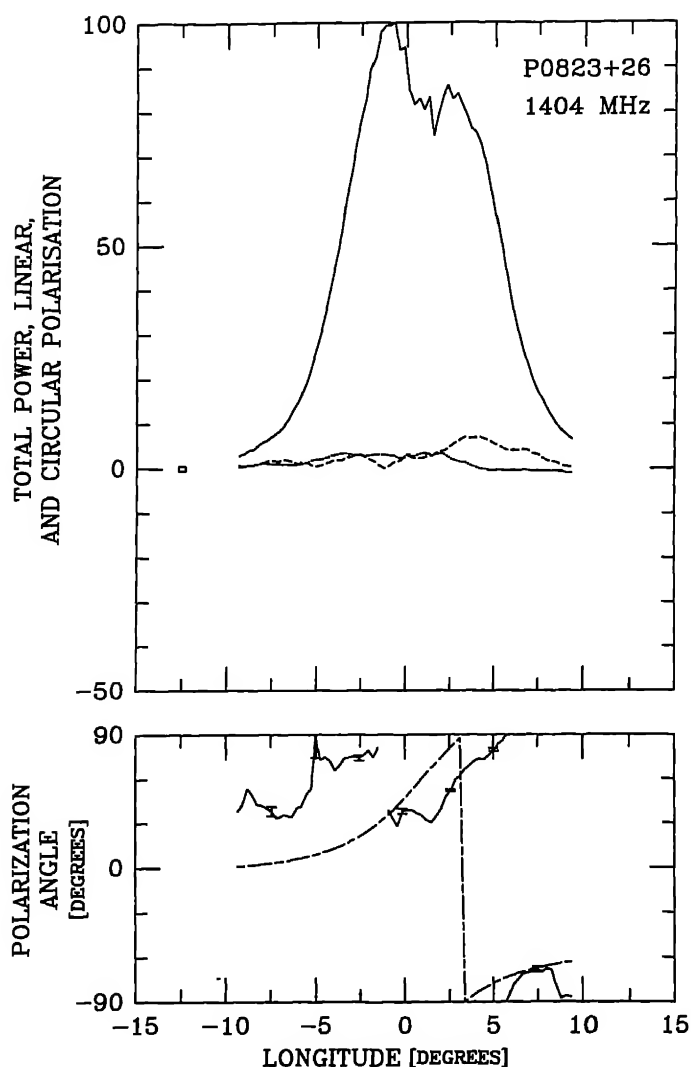
Figure 6(c).

Figure 6(a–c). Partial, 'mode-separated' profiles for pulsar 0823 + 26 at 1404-MHz on 9th October 1981 as in Fig 4

profile represents 4 0% of the samples and 19 0% of the power of the total individual-pulse sequence at an *L*-threshold value of 2σ. And, again, lowering the *L* threshold to irrelevance produces no qualitative change in the form of the secondary-mode profile

'Mode-separated' profiles corresponding to the 1404-MHz observation in Fig. 1(c) are given in Figs. 6(a–c). Only a limited longitude range around the MP was available in these observations. The PA-model parameters used were similar to those given above. At this frequency 60 1% (16 5%) and 24.1% (8 4%) of the power (samples) accrued to the primary (Fig 6a) and secondary (Fig 6b) modes, respectively, and 15.8% (75.1%) to the residual (Fig. 6c) profile

5. Main-pulse emission geometry

Rather few 'mode-separated' partial profiles, computed from well resolved and calibrated observations, are available in the literature; it is thus far too early to attempt any generalizations regarding them. In particular, the question of what constitutes a 'component' in total-average profiles has been a subject fraught with controversy (and is perhaps only now beginning to clarify); therefore we certainly have no wish to hastily attribute this status to every discernible minor feature in mode-separated partial profiles. Nevertheless, the appearance of the additional features in pulsar 0823 + 26's secondary-mode profile is so extraordinary that we are emboldened to attempt some speculative analysis.

Therefore, let us proceed by entertaining the hypothesis that the two new, minor features on the leading and trailing edges of the main one are indeed correctly interpreted as a conal-component pair, which was too weak to detect in the total profile at any frequency We noted above—and reiterate here – that 0823 + 26, though almost certainly correctly classified as a core-single (S_t) pulsar, produces no identifiable conal 'outriders' even at the highest frequencies of observation. Thus, were we to interpret the secondary-mode features as 'outriders', we would encounter no conflict with our existing knowledge of this star

A way to assess whether this interpretation makes sense is that of exploring its geometrical consequences. The basic magnetic geometry of this pulsar seems well established. Paper IV argued that core-component widths can be used to determine the latitude of the magnetic axis α, and pulsar 0823 + 26 was discussed not only as an example of a pulsar whose interpolated 1-GHz core width implies that $\alpha \simeq 90°$, but one whose overall PA traverse supports this, and whose interpulse (0823 + 26 is almost certainly a two-pole interpulsar) leaves virtually no doubt.

More questionable then is its emission geometry in relation to our sightline. Referring again to Fig. 1, recall that the maximum PA sweep rate R is about $+15°/°$ for the primary mode and about $+30°/°$ for the secondary one. Using the definition of R following equation (1), we see that this results in β values of $+3.8°$ and $+1.9°$, respectively, where the '$+$' sign has been added to indicate that these are outside (positive) traverses on the basis of their flattened wings (see Narayan & Vivekanand 1982).

The significance of the β value associated with the primary mode is not yet clear, but we are immediately at liberty to use the secondary-mode β value, along with α and the (outside, half-power) width of the conal component pair to calculate the conal emission radius which would be expected. This latter value, scaled from the older and newer secondary-mode profiles in Figs 4 and 5 are 16.7° and 16.3°, respectively. Now using equation (4) of Rankin (1993a; hereafter Paper VIa), this implies a conal radius ρ of just less than 8 5° (if we 'round' down to 16° in an effort to 'extrapolate' to 1 GHz, ρ is 8 2°; please see Rankin (1993b); hereafter Paper VIb, Table 4). In either case, 0823 + 26's secondary-mode ρ value is clearly just what one would expect for an outer cone, as can be seen by referring to equation (5) of Paper VIa

It would then seem that the most economical interpretation of the 'outriders' in the secondary-mode profile of pulsar 0823 + 26 is that they indeed represent an outside conal component pair, which is so weak that it can be detected only by removing the dominant primary-mode power from the profile. This line of interpretation is entirely consistent quantitatively with the known geometry of the pulsar and further an answer to the question – for 0823 + 26, certainly, but also in general – of why some core-single pulsars have no discernible conal outriders

6. Postcursor emission geometry

First, several different lines of argument now give similar conclusions regarc basic geometry of pulsar 0823 + 26 Its interpulse (Hankins & Fowler 1986; Pa analysis of its PA traverse (Lyne & Manchester 1988; Blaskiewicz *et al.* 1991), . width of its MP core component (Paper IV) all indicate that its magnetic axis is orthogonal to its rotational axis Moreover, two somewhat different analyse: & Manchester (see especially, their table 2) and that in both this paper and Pap find that our sight line passes within a mere 1 or 2° of the magnetic axis

Second, the identification above of the secondary-mode 'outriders' as an oute component pair marks these components as falling at the extreme boundary o emission in this pulsar, in terms both of angle from the magnetic axis and of di from the star We now have overwhelming evidence that conal emission is consistent in its angular beaming properties (Paper VIa & b; Gil *et al* 1993, Gil & 1993), the outer conal emission radius is $5\,75°\,P^{-1/2}$, or, as we saw in the pre section, about 8°

In this geometric context it is now much more interesting to consider the signifi of the postcursor component in pulsar 0823 + 26, and the first point to make is tl now have no possible option of viewing the PC component as some kind of widely separated portion of a conal double profile as was attempted in Paper II PC lies much too far from the magnetic axis – some 30° – for it to be of conal ori any usual sense; furthermore, there is *only* a PC, no precursor[!]

While we cannot say how it is that the PC is emitted, it would seem that 0823 geometry offers a particularly good opportunity to identify unusual types of emi As noted above, not only is this pulsar's magnetic moment nearly parallel to its eq but so is our sight line! Only in this geometry is there a bundle of field lines (also p; to the star's rotational equator) which remains in view as the star rotates an tangent points in the observer's direction for an unusually large fraction of the rotation period One such bundle trails the magnetic axis, and it is worth notin; any 'field-line sweepback' at high altitude will increase the curvature of this bi Another bundle leads the magnetic axis, and (with enough sweepback) it coulc have tangents in the observer's direction, but only at great altitude and for a sh interval

If the PC component is emitted along this trailing bundle of peripheral, equal field lines at a height at which the field remains essentially dipolar, then it is possil estimate the emission height of the PC, again using equation (2) in Paper VIa F< angular separation between the PC and the magnetic axis (taken to be the MP pe; about 32° (Hankins & Fowler 1986), we find an emission height of about 4×10^3 that is, about 400 stellar radii or some 4% of the light-cylinder radius – as comp to the nominal 210-km emission height of the outer cone. Any poloidal distortic the field would increase the curvature of the trailing bundle of equatorial field and decrease the emission height Interestingly, it would also decrease that o leading bundle, perhaps explaining why we more generally see postcursors r; than precursors. Both height and sweepback will tend to increase the curvatu the trailing bundle, which may favour emission by particles with quite diffe energies than those responsible for the MP Theories of pair-production disch above pulsar polar caps, seem to produce a broad distribution of particle ene: (Daugherty and Harding 1986) Finally, we note that the MP-PC separation *incre*

Figure 7. Longitude-to-longitude intensity correlation plot corresponding to the 430-MHz observations in Fig 1b Average profiles comprising the noise, the MP-PC, and IP windows have been plotted on both axes for convenience, and at longitudes larger than −15° the quantities *I*, *L* and *V* have been multiplied by a factor of 5 to show the postcursor and interpulse regions more clearly The correlation is indicated by a coloured rectangle at the intersection of the two longitudes, and the colour scale in the upper left hand corner of the figure gives the magnitude of the correlation coefficient. The figure is divided into two triangular regions, the upper left one (row number > column number), gives the correlation of the current pulse with itself at different longitudes (zero lag), whereas, the lower right one gives the correlation between the current pulse and the previous pulse (lag = −1).

weakly with frequency, suggesting that the higher frequency PC emission is emitted at greater heights than the low frequency emission, if so, this would be a 'radius-to-frequency mapping' of the opposite sense to that usually encountered

If this is the correct interpretation for the geometry of the PC component, then we note that both the PC and the latter conal outrider are emitted along the same bundle of trailing equatorial field lines It is then possible that the two components will exhibit some correlation in the intensities of their constituent individual pulses The longitude-to-longitude correlation of the total power, corresponding to the 430-MHz observations in Fig 1b, is given in Fig 7. The longitude, of course, labels both axes, and average profiles comprising the noise, the MP-PC, and IP windows have been plotted for convenience. A colour scale indicating the degree of correlation is given at the upper left of the figure The upper triangular region shows that the longitude-longitude correlations are calculated by correlating the emission in the same pulse at different longitudes (zero lag) In the lower triangular region, the emission at any given longitude corresponding to the row number is correlated with emission in the previous pulse at longitude corresponding to the column number (lag = + 1) The diagonal line is included in the lower part with lag = + 1

This figure clearly shows the correlation between the MP and PC emission Interestingly, the correlation is significant only between the central portion of the PC and the wings of the MP, between the center of the MP and the PC there is hardly any significant correlation. If anything, the emission in the center of the MP is anti-correlated with the PC emission of the previous pulse, as can be seen from the lower part of the figure However, the correlation between the wings of the MP and PC persists even for a one-period lag Similarly, the MP leading and trailing wings exhibit highly correlated emission, but this emission is not significantly correlated with that of the MP center Another curious feature is the anti-correlation between the MP peak and the 'bridge' region between the MP and PC. This correlation was also noted by Popov & Sieber (1990) in their 1700-MHz study, although their observations were restricted narrowly to the MP region There is also a significant correlation between the leading part of the previous MP and the current IP peak

All this notwithstanding, we note that there are five other pulsars with known PC components: The Crab pulsar is usually discussed as having a 'precursor' component, but in that this component appears to be a core component (Paper IV), one might better regard the star's MP as a postcursor to it Then there are 0940 + 16, 1530 + 27 (Rankin *et al* 1989), probably 1530 − 53 (McCulloch *et al*. 1978, Manchester *et al* 1980; McCulloch *et al*. 1982), 1929 + 10 (Perry & Lyne 1985, Rankin & Rathnasree 1996), and more recently 2217 + 47 (Suleymanova & Shitov 1994). We know of no pulsar with a true precursor – that is, one with a weak patch of emission which leads a core component Apart from the Crab pulsar and 1929 + 10 – which are almost certainly orthogonal rotators – we know very little about the geometry of these other stars; most have not even been adequately classified, in part because of their odd 'postcursor' emission Somewhat more is known about 2217 + 47, it was classified as an S_t pulsar in Paper VIb with an α of only 42° This value could easily increase, however, as the profiles available in the literature are mostly poor (the only ∼ 400-MHz profile available is from LSG in 1971') and thus probably not well resolved

We note that pulsars 0823 + 26 and 2217 + 47 have very similar periods and period derivatives, and the completely equatorial model used above to discuss the emission

geometry of the former also provides an attractive scenario for understanding Suleymanova & Shitov's observations of the latter. Perhaps the most surprising feature of the 2217 + 47 postcursor is that it slowly varied in amplitude and position over time, possibly correlated with changes in the torque on the star Indeed, if the PC emission is occurring high on this bundle of trailing, equatorial field lines, torque changes might change the curvature and thus the height of the radiation, which would in turn change its phase within the profile relative to the core component. But we do not yet know whether 2217 + 47 – or really any of the other 'postcursor' pulsars apart from the Crab – have orthogonal geometries We are guessing that they probably do, but additional observations and analysis are required to answer this question If so, some – 2217 + 47 to be sure – may prove highly useful as a means of exploring other regions of the pulsar magnetosphere. Pulsars with PC components may also be good candidates in which to search for new interpulses

7. Interpulse emission geometry

Little can be said with confidence about pulsar 0823 + 26's interpulse geometry No quality observation of this feature exists in the literature, and, given its weakness, none may be possible in the foreseeable future. Nonetheless, the 430-MHz profile (Rankin & Benson 1981) appears more single, and the 1400-MHz profile (Rankin *et al* 1989) has a flat top which might indicate incipient conal outriders (as per the usual triple or possibly conal-single evolution) Both IP profiles have a full width at half maximum of about 16 or 17°, and the PA sweep rate is about − 6°/°. These values do not make any immediate sense in terms of the geometrical arguments of Paper VIa & b If the above width corresponds to an outer cone, either the IP sweep rate needs to be steeper or the width smaller One possibility is that here we are cutting an outer cone on its extreme edge, so that the sightline comes nowhere near the high-intensity 'shoulder' of the conal beam.

8. Polarization-modal structure of PSR 0823 + 26's emission

We have seen above that the primary mode at 430 MHz represents about 68–69% and the secondary-mode about 18–19% of the total power in the sequence of pulses when the threshold is set at a level such that L must exceed about two σ in the off-pulse noise; that is, the primary mode is about 3.5 times stronger than the secondary one. Of course, these numbers will change somewhat if a) the mode-separation algorithm is not accurately segregating the modal power in the PA-longitude diagram, b) if the L threshold level is changed, or c) if the emitted modal power varies in time We have done our best to assure that the modal separation is correct, although given the proximity of the two modes near the primary-mode 'blotch' in Fig. 1, some ambiguity is unavoidable. As for the second condition, a 2-σ threshold gives a sample uncertainty in the PA of ± 30°, and any lower threshold will increase the number of unpolarized or noise-dominated samples which are spuriously assigned to one mode or the other We re-emphasize that only for those samples with adequate residual linear polarization can we make a choice about their mode For the others, all such information has been lost through depolarization on time scales short compared to the sampling interval, and we

can only speculate about the significance of this depolarized portion of the puls emission Observations suggest either that these are relatively stable or that we h found the pulsar in the same 'modal' state

We can then ask whether this is the 'true' power ratio of the two modes. So 12–14% of the power fell below the threshold in *L,* and the average of these 'residt samples shows virtually no linear polarization It might then be a) that most this power is associated with the secondary mode, which is only some 10% polariz in which case the modal ratio is about 70/30%, b) that the power is about equa divided between the two modes (and, indeed, the residual PA falls near the prime mode before the MP peak and near the secondary mode thereafter) in which ce the modal ratio is about 75/25%, or c) that most of the residual power is associat with the primary mode in view of its greater intensity, in which case the moc ratios are about 80/20% At 21 cm about 60% of the power was found in the prima mode to about 24% and 16% for the secondary mode and residual categories, s Fig 6 If the polarization-mode switching phenomenon is broad band – as, inded it appears to be – these latter numbers might be squared with any of the thr alternatives

It is also useful to consider the fractional linear polarization, and comparing the tot average profiles in Fig 1 with the modal partial profiles in Figs. 4–6 we see that tl mode separation did not dramatically increase the fractional linear polarization, eith at 430 or 1400 MHz. The earlier 430-MHz observation has a peak fractional linea polarization of about 35%, whereas the primary mode's is only about 42%. Similarl that of the later 430-MHz run goes from about 45% to 52% and the 1400-MHz or from about 28% to 36%. The later data are better resolved than the earlier at both 43 and 1404 MHz, and this may be responsible, in part, for their somewhat larger amoun of aggregate linear polarization.

In all cases the secondary-mode fractional linear is lower. We then apparently hav a situation in pulsar 0823 + 26 wherein very significant amounts of depolarization ar occurring on time scales shorter than the inherent time resolution of the observations here in all cases some part of 1° longitude. This also largely explains the fact that th secondary mode is more depolarized than the primary one, because secondary-mod samples will typically contain more primary-mode power than primary ones wil secondary-mode power, by simple reason of their relative intensities Only thos unusual samples in which the secondary mode dominates the primary will be recog nized as 'secondary-mode' samples—and accumulate in the 'secondary-mode' profile Generally the secondary mode will just exceed the primary, and these are the conditions which are most depolarizing. These factors are especially complicated in 0823 + 26, however, owing to the spectacular non-orthogonality of the two modes throughout the duration of the MP

9. Displaced modal emission in the main pulse

A very interesting feature of the modal partial profiles in Figs. 4–6 is the displacement in phase between the primary and secondary modes Reference to these figures shows that the secondary mode 'MP' always leads the primary-mode feature, at 430 MHz by $1 5 \pm 0.1°$ and at 1404 MHz by some $1 3 \pm 0.1°$. Displacement in rotational phase has been seen before in the components of mode-separated profiles – the first component of

1737 + 13, for instance, shows a dramatic offset (Rankin *et al.* 1988) – however, this effect has not, before to our knowledge, been identified in a core component[@].

The question is what interpretation to make of this phase delay, and at this point two possibilities seem open The first is that the offset is a geometrical phenomenon We saw above that the observed offset was somewhat greater at 430 as compared to 1400 MHz – but just so within the errors – and just over 1° of longitude is quite comparable to the 3 36° diameter of the pulsar's polar cap. Another possibility is that we are here seeing an effect of birefringent propagation in the pulsar's inner magnetosphere as suggested, for instance, by Barnard & Arons (1986) If this is the case we might expect the effect to become more pronounced at lower frequencies—and furthermore this 'double' nature of the core component might be connected with such well known, but entirely unexplained phenomena such as 'absorption' and the observed broadening of some core components at lower frequencies (see Paper II).

10. Summary and conclusions

The polarization structure of the radiation which comprises pulsar 0823 + 26's average profile at both 430 and 1400 MHz has been studied Two polarization modes are identified in the emission over a substantial range of longitudes around the MP and PC In some intervals they are roughly orthogonal; however, just under the MP the two modes are more conspicuously non-orthogonal – and thus difficult to distinguish – than in any other pulsar we know of We have attempted to construct partial profiles in which the power in the two polarization modes is largely separated and have identified two (mostly) continuous, non-orthogonal PA trajectories which seem to correspond to these modes. The primary mode in 0823 + 26 is three to perhaps five times stronger than the secondary mode overall and thus dominates the emission and the PA at most longitudes. It is then not surprising that the primary-mode MP closely resembles the total-profile MP

The secondary-mode profile consists of three MP features, which appear to be a central core component and a surrounding pair of conal outriders. The (outside half-power) width of the outriders together with the secondary-mode PA traverse appear compatible with the interpretation that these conal features represent an outer emission cone.

This technique could lead to the discovery of covert emission features in the profiles of other pulsars with single profiles but complicated PA histograms. In this context, it is interesting to speculate about the emission geometry of the PC feature, which follows the MP by some 30°. Having now identified a pair of much more closely spaced components, which appear to represent an outer cone of emission, it is clear that the PC cannot be a conal component in any usual sense

Overall, 0823 + 26 seems to have a nearly equatorial geometry—that is, both the magnetic axis and the sight line appear to lie close to the rotational equator of this pulsar We then note that in this situation there is a bundle of trailing field lines which has a tangent in our direction for a substantial portion of the rotation cycle of the

---

[@] Pulsar 1737 + 13's core component is also misaligned in the mode-separated profiles, but given the greater complexity of both partial profiles, it is not at all clear what interpretation to make of this circumstance

pulsar Perhaps it is emission along this bundle – at a height of some $4 \times 1($ about 4% of the light cylinder – that the PC emission occurs.

If the PC component and the trailing conal outrider are both emitted al trailing bundle of equatorial field lines, then it is possible that their emi correlated Indeed, we find that there is significant correlation between the PC longitude ranges of the trailing conal outriders, and furthermore that this cor becomes negligible between the PC and the core-emission region.

Finally, it seems that the pulsar does exhibit some $6 4 \pm 0 8\%$ null pulses, somewhat more than the 5% limit of Ritchings (1976).

Acknowledgements

References

Backer, D C., Boriakoff, V, Manchester, R N 1973, *Nat Phys Sci.*, **243**, 77.
Backer, D. C 1973, *Astrophys J*, **182**, 245
Backer, D C., Rankin, J M 1980, *Astrophys J Suppl*, **42**, 143
Barnard, J J, Arons, J 1986, *Astrophys J*, **302**, 138
Bartel, N, Sieber, W, Wielebinski, R 1978, *A & A*, **68**, 361
Blaskiewicz, M, Cordes, J M., Wasserman, I 1991, *Astrophys J*, **370**, 643
Cordes, J M, Rankin, J. M, Backer, D C 1978, *Astrophys. J*, **223**, 961
Craft, H D, Lovelace, R V E, Sutton, J M 1968, *I A U Circ No. 2100*
Daugherty, J K, Harding, A K 1986, *Astrophys. J*, **309**, 362
Gil, J A, Snakowski, J K, Stinebring, D R 1991, *Astrophys J*, **242**, 119
Gil, J A, Lyne, A G, Rankin, J. M, Snakowski, J K, Stinebring, D R 1992, *A&A*, **255**
Gil, J A, Kijak, J 1993, *A & A*, **273**, 563
Gil, J A, Kijak, J, Seiradakis, J. H 1993, *A&A*, **272**, 268
Hagan, J 1987, *NAIC Electronics Department Manual No 8319*
Hankins, T H, Fowler, L A 1986, *Astrophys. J.*, **304**, 256
Hankins, T H, Rickett, B J 1986, *Astrophys J.*, **311**, 684
Hankins, T H, Rankin, J M 1994, private communication
Izvekova, V. A., Kuz'min, A D, Malofeev, V M, Shitov, Yu P. 1981, *Astrophys. Space Sci,*
Komesaroff, M M 1970, *Nature*, **225**, 612.
Kramer, M, Wielebinski, R, Gil, J A, Seiradakis, J H, Jessner, A 1994, *A&A*, **107**, 527.
Lang, K R 1969, *Astrophys J Lett*, **158**, L175
Lyne, A G, Manchester, R N. 1988, *Mon Not. R astr Soc.*, **234**, 477.
Manchester, R N, Hamilton, P. A, McCulloch, P M 1980, *Mon Not R astr. Soc.*, **192**,
McCulloch, P M., Hamilton, P A, Manchester, R. N., Ables, J. G 1978, *Mon Not. R astr* **183**, 645
McCulloch, P M, Hamilton, P A., Manchester, R N. 1982, private communication

arayan, R., Vivekanand, M 1982, *A&A*, **113**, L3

:rillat, P 1988, *NAIC Computer Department Report # 23*

:rillat, P 1992, private communication

:rry, T E , Lyne, A G 1985, *Mon Not R astr Soc* , **212**, 489

illips, J A , Wolszczan, A 1992, *Astrophys J.*, **385**, 273

opov, M V , Sieber, W 1990, *Sov Astr* , **34**, 382

adhakrishnan, V , Cooke, D J 1969, *Astrophys J Lett* , **3**, 225

ankin, J M 1983b, *Astrophys J*, **274**, 359 (Paper II)

ankin, J M 1986, *Astrophys J.*, **301**, 901 (Paper III)

ankin, J M 1988, *Astrophys J.*, **325**, 314

ankin, J M 1990, *Astrophys J* , **352**, 247 (Paper IV)

ankin, J M 1993a, *Astrophys J* , **405**, 285 (Paper VIa)

ankin, J. M 1993b, *Astrophys J (Suppl)*, **85**, 145 (Paper VIb)

ankin, J M , Benson, J M 1981, *Astr J.*, **86**, 418

ankin, J. M , Campbell, D. B , Backer, D C 1974, *Astrophys J* , **188**, 609

ankin, J M , Campbell, D B , Spangler, S 1975, *NAIC Report # 46*

ankin, J M , Rathnasree, N. 1996, in preparation.

ankin, J. M , Stinebring, D R , Weisberg, J M 1989, *Astrophys J* , **346**, 869

ankin, J M , Wolszczan, A , Stinebring, D R 1988, *Astrophys J* , **324**, 1048

itchings, R T. 1976, *Mon Not R astr Soc* , **176**, 249

ieber, W 1973, *A&A*, **28**, 237

tinebring, D R , Cordes, J M , Rankin, J M , Weisberg, J M , Boriakoff, V 1984, *Astrophys. J (Suppl)*, **55**, 247

uleymanova, S A , Shitov, Yu P 1994, *Astrophys J Lett* , **422**, L17

aylor, J. H , Huguenin, G R 1969, Symposium on Pulsars and High Energy Activity in Supernova Remnants, Academia Nationale dei Lincei, Rome, 1969 December 18.

ilouris, K M., Seiradakis, J M , Gil J , Sieber, W , Wielebinski, R 1995 *A&A*, **293**, 153

Disk Luminosity and Angular Momentum for Accreting, Weak Field Neutron Stars in the 'Slow' Rotation Approximation

Bhaskar Datta[1], Arun V. Thampan & Paul J. Wiita[2] *Indian Institute of Astrophysics, Bangalore 560 034, India*
[1]*Visiting Professor Raman Research Institute, Bangalore 560 080 India.*
[2]*Permanent address Department of Physics & Astronomy, Georgia State University, Atlanta, GA 30303–3083, USA*

Abstract. For accretion on to neutron stars possessing weak surface magnetic fields and substantial rotation rates (corresponding to the secular instability limit), we calculate the disk and surface layer luminosities general relativistically using the Hartle & Thorne formalism, and illustrate these quantities for a set of representative neutron star equations of state We also discuss the related problem of the angular momentum evolution of such neutron stars and give a quantitative estimate for this accretion driven change in angular momentum Rotation always increases the disk luminosity and reduces the rate of angular momentum evolution These effects have relevance for observations of low-mass X-ray binaries

Key words. Stars: accretion—stars: accretion disks—stars· neutron—stars rotation.

1. Introduction

Disk accretion on to a neutron star possessing a weak surface magnetic field ($B \lesssim 10^8$ G) provides interesting X-ray emission scenarios, and is relevant for understanding X-ray bursters and low-mass X-ray binaries (e.g. van Paradijs 1991) Such weak-field neutron stars can rotate very rapidly and are also seen as millisecond pulsars (Radhakrishnan & Srinivasan 1982, Alpar *et al* 1982; Bhattacharya & van den Heuvel 1991) and may be relevant for quasi-periodic oscillators (QPOs) (Priedhorsky 1986; Paczyński 1987). The equation of state of neutron star matter as well as general relativity play essential roles in such a scenario. This is in contrast to the strongly magnetic ($B \gtrsim 10^{12}$ G) accreting neutron stars, where plasma processes dominate (e.g., Ghosh & Lamb 1991). For the weak-field case, the radius of the innermost stable circular orbit (r_{orb}) plays a central role, deciding quantities of observational interest such as the disk luminosity. The relevance of this parameter (r_{orb}) was emphasized by Kluźniak & Wagoner (1985, hereafter KW), who pointed out that for weak-field accreting neutron stars it is incorrect to always make the usual assumption that the accretion disk extends very close to the surface of the star, and is separated from it by a thin boundary layer. Using Schwarzschild geometry, Syunyaev & Shakura (1986, hereafter SS) concluded that the boundary layer brushing the neutron star surface will be substantially more X-ray luminous than the extended accretion disk If the star's radius (R) is less than r_{orb}, the

357

boundary layer is likely to be characterized by poorly collimated tangential motion of t infalling matter and a comparatively soft emission spectrum Whether or not R excee r_{orb} (and consequently the detailed features of the accretion scenario) depends on t geometry of the spacetime and also the equation of state of neutron star matter

An important aspect of disk accretion on to weak-field neutron star is the possibili that the neutron star will get spun up to very short rotation periods ($\lesssim$ millisecon over a time of the order of hundreds of millions of years. For such rapid rates rotation, the relativistic effect of dragging of inertial frames in the vicinity of the neutron star will be important This effect will alter the trajectories of infalling particles compared to the non-rotational case Therefore, for a quantitative description of tl accretion features, one must take into account the relativistic effects of rotation upc the spacetime geometry. Although the possible importance of such effects was stresse by KW and SS, the details were not worked out by them

In this paper we address this question and calculate the disk and surface lay luminosities incorporating the rotational effects in a general relativistic framework. W take the spun up neutron star to be rotating at a particular value, namely, the secul instability limit so as to illustrate the maximal reasonable effects of rotation. Th corresponds to the late stages of accretion. We use the Hartle & Thorne (1968, hereaft HT) formalism, for our purpose, this formalism describes a rotationally perturbe Schwarzschild space-time. The HT formalism is valid for strong gravitational fields bt only in the limit of uniform rotation with a rate that is 'slow' compared to the critic speed for centrifugal break-up Neutron star models rotating at the secular instabili limit (assuming the star to be homogeneous), relevant in the context of accretio induced spun up neutron stars, are within this limit (Datta & Ray 1983), so th approximation will usually be adequate Recently Cook *et al* (1994a & b) calculate last stable orbits of rotating neutron stars incorporating higher order rotational term that go beyond the HT approximation. However, these authors did not use their resull to estimate the disk luminosity and angular momentum evolution involved in th accretion scenario Although the Hartle & Thorne prescription assumes rotationall perturbed geometry, the use of this prescription provides a first estimate, which i amenable to a straightforward numerical treatment, of the luminosity values an angular momentum evolution for an accreting weak-field neutron star. This can b quite useful in observational applications such as low-mass X-ray binaries. Ou calculations are done for a range of stable neutron star configurations computed usin a representative sample of the proposed equations of state of neutron star matter W also consider the accretion driven evolution of the angular momentum of the neutro star in a more accurate fashion than was done by KW

2. Accretion on to a rotating neutron star

To describe the spacetime around a rotating neutron star we use the metric suggestec by Hartle & Thorne (1968) This metric describes a rotationally perturbed Schwar zschild geometry to order Ω^2, where Ω is the angular velocity of the star as seen b a distant observer. The general form of the metric is (signature: $+ - - -$)

$$ds^2 = g_{\alpha\beta}dx^\alpha dx^\beta, (\alpha, \beta = 0, 1, 2, 3)$$
$$= e^{2\Phi}dt^2 - e^{2\Psi}(d\phi - \omega dt)^2 - e^{2\mu}d\theta^2 - e^{2\lambda}dr^2 + \mathcal{O}(\Omega^3/\Omega_c^3). \tag{1}$$

Here ω is the angular velocity of the cumulative dragging of inertial frames and $\Omega_c = (GM/R^3)^{1/2}$, the critical angular velocity for equatorial mass shedding, where M and R are the mass and radius of the non-rotating neutron star. For simplicity, we use the geometric units: $c = 1 = G$. The metric components correspond to an interior with the identification:

$$e^{2\Phi} = e^{2\nu}\{1 + 2(h_0 + h_2 P_2)\}, \tag{2}$$

$$e^{2\psi} = r^2 \sin^2\theta \{1 + 2(v_2 - h_2)P_2\}, \tag{3}$$

$$e^{2\mu} = r^2 \{1 + 2(v_2 - h_2)P_2\}, \tag{4}$$

$$e^{2\lambda} = \frac{1 + 2(m_0 + m_2 P_2)/(r - 2m)}{1 - 2m/r}, \tag{5}$$

(where 2ν is the gravitational potential function for the non-rotating star and m is the gravitational mass contained within a volume of radius r) and to an exterior with the identification:

$$e^{2\Phi} = e^{-2\lambda} = 1 - 2\frac{M'}{r} + 2\frac{J^2}{r^4}, \tag{6}$$

$$e^{2\psi} = r^2 \sin^2\theta, \tag{7}$$

$$e^{2\mu} = r^2. \tag{8}$$

Here M' and J are respectively the mass and angular momentum of the rotating configuration of the star. The quantity P_2 is the Legendre polynomial of order 2, and h_0, h_2, m_0, m_2, v_2 are all functions of r that are proportional to Ω^2 (see HT). The metric has the desirable property that the internal and external forms match at the surface of the star. For our purpose here, we shall retain only the spherical deformation terms (characterized by subscript 0) and neglect the quadrupole deformation terms (characterized by subscript 2). The latter are necessary for computing stellar quadrupole deformation, but average out in calculating the rotation induced changes to M and R. The applicability of the metric (1) is valid for Ω small in comparison to Ω_c, and to go beyond that approximation requires a treatment similar to that of Cook *et al.* (1994a, b).

A relativistic effect of rotation, important for the astrophysical scenario that we consider here, is the dragging of inertial frames, which implies

$$\bar{\omega}(r) \neq \Omega, \tag{9}$$

where $\bar{\omega}(r)$ is the angular velocity of the stellar fluid relative to the local inertial frame, and is given by (HT)

$$\frac{d}{dr}\left(r^4 j \frac{d\bar{\omega}}{dr}\right) + 4r^3 \bar{\omega} \frac{dj}{dr} = 0, \tag{10}$$

where

$$j(r) = e^{-\nu}(1 - 2m/r)^{1/2}, \tag{11}$$

with the boundary conditions

$$\left(\frac{d\bar{\omega}}{dr}\right)_{r=0} = 0; \quad \bar{\omega}(r = \infty) = \Omega. \tag{12}$$

For $r > R$ (i e, outside the star),

$$\bar{\omega}(r) = \Omega - 2J/r^3, \tag{1}$$

where J is the angular momentum of the star.

$$J = \frac{R^4}{6}\left(\frac{d\bar{\omega}}{dr}\right)_{r=R}. \tag{1}$$

The equations of motion are derived from the Lagrangian corresponding to the metr (1):

$$\mathscr{L} = \tfrac{1}{2}\{e^{2\Phi}\dot{t}^2 - e^{2\lambda}\dot{r}^2 - e^{2\mu}\dot{\theta}^2 - e^{2\psi}(\dot{\phi} - \omega\dot{t})^2\}, \tag{1}$$

where a dot represents a derivative with respect to proper time We shall, for purpose illustration, take the polar angle (θ) to be fixed and equal to $\pi/2$, which corresponds t the equatorial plane

The metric (1) and the equations of motion provide three equations in the thre variables $\dot{\phi}$, $\dot{t}$, and $\dot{r}$. From these, we can get (see KW)

$$\dot{r}^2 = \tilde{E}^2 - 2\omega\tilde{E}\tilde{l} - h^2(1 + \tilde{l}^2/r^2), \tag{1}$$

where

$$\tilde{E} = h^2\dot{t} + \omega r^2\dot{\phi}, \tag{1'}$$

and

$$\tilde{l} = r^2(\dot{\phi} - \omega\dot{t}), \tag{1}$$

stand respectively for the energy and angular momentum per unit rest mass (denoted b m_B) and

$$h = (1 - 2M'/r)^{1/2}. \tag{1}$$

The conditions for the turning point of the motion, the extremum of the energy, an the minimum of the energy are respectively given by (see Misner, Thorne & Wheele 1974)

$$\tilde{E}^2 = V^2, \tag{2}$$

$$\frac{d\tilde{E}}{dr} = 0 = \frac{dV}{dr}, \tag{21}$$

and

$$\frac{d^2\tilde{E}}{dr^2} > 0, \tag{2}$$

where V is the effective potential, given by

$$V^2 = 2\omega\tilde{E}\tilde{l} + h^2(1 + \tilde{l}^2/r^2) \tag{2}$$

For marginally stable orbits we can use the condition

$$\frac{d^2\tilde{E}}{dr^2} = 0 = \frac{d^2V}{dr^2}. \tag{2}$$

Written explicitly, equations (20), (21), and (24) respectively become

$$\tilde{E}^2 - \frac{\tilde{j}a\tilde{E}}{x^3} - \left(1 - \frac{1}{x}\right)\left(1 + \frac{a^2}{x^2}\right) = 0, \tag{25}$$

$$a^2 + \frac{3\tilde{j}a\tilde{E}}{(2x-3)} - \frac{x^2}{(2x-3)} = 0, \tag{26}$$

$$x^2 - 3a^2x + 6(a^2 - \tilde{j}a\tilde{E}) = 0, \tag{27}$$

where $x = r/2M'$, the dimensionless radial co-ordinate; $\tilde{j} = J/M'^2$ and $a = \tilde{l}/2M'$ are the dimensionless angular momenta for the star and the infalling matter respectively. Solving equations (25)–(27) simultaneously gives the values for the energy (E_{orb}) and the specific angular momentum (a_{orb}) of the accreted particle in the innermost stable orbit having a radius $x = x_{orb}$

Using Schwarzschild geometry, it was shown by SS that an accretion disk whose luminosity is small compared to the Eddington limit can exist only for R greater than the radius of the last stable circular orbit, $3r_g$, where $r_g = 2M =$ the Schwarzschild radius. For $R < 3r_g$, the accreting matter falling on to the neutron star will follow the trajectory of a free particle in this geometry, with an energy equal to $m_B\sqrt{8/9}$. These authors also gave estimates of the energy released in the disk and in the boundary layer for R/r_g ranging from 1 5 to 10 without reference to any specific equation of state model. In the case where the neutron star has a high spin rate, the innermost stable orbit was calculated by KW using the HT metric to describe rotating spacetime These authors, however, did not estimate the luminosity, and they neglected the rotational corrections to M and R in computing the evolution of angular momentum

For a low-field, accreting neutron star possessing substantial rotation, the luminosity from the disk accretion can be calculated using equations (25)–(27). We use here the notation $x^* = R'/2M'$, where M' and R' correspond to the neutron star mass and radius that include corrections due to the rotation The following distinct cases are possible:

2 1 *Case (a)· Radius of the star is greater than r'_{orb}*

If an accretion disk were to form around a relatively large neutron star (i.e., $x^* > x_{orb}$), the ingress of a particle of rest mass m_B from infinity to the inner disk boundary will release an amount of energy given by

$$E'_D = m_B\{1 - \tilde{E}_k(x^*)\}, \tag{28}$$

where $\tilde{E}_k(x^*)$ stands for the specific energy of the particle in the stable orbit just above the surface, obtained by solving equations (25) and (26) numerically for $x = x^*$ The energy loss in the boundary layer will be

$$E'_S = m_B\{\tilde{E}_k(x^*) - \tilde{E}_0(x^*)\}, \tag{29}$$

where $\tilde{E}_0(x^*)$ is the energy of the particle at rest on the surface of the neutron star, which can be calculated from equation (25) for $x = x^*$ and the specific angular momentum at the star's surface.

2 2   Case (b)   Radius of the star is smaller than r'_{orb}

In this case, $x^* < x_{orb}$ and the accretion disk will extend inward to a radius correspond
ing to $x = x_{orb}$. Now the energy released in the disk as the particle comes in from infinit
to the innermost stable orbit will be

$$E'_D = m_B\{1 - \tilde{E}_{orb}\},\qquad\qquad(3C$$

and the energy released in the boundary layer will be

$$E'_S = m_B\{\tilde{E}_{orb} - \tilde{E}_0(x^*)\}.\qquad\qquad(31$$

A remark about the boundary layer luminosity formula that we use, is in order here
Although this formula gives a plausible estimate for the boundary layer luminosity
strictly speaking, it is an overestimate as it does not take into account the subtraction c
the energy that goes into spinning up of the neutron star The need for such a correctio
was pointed out by Kluźniak (1987) and quantitative estimates for this were suggeste
by Ghosh, Lamb & Pethick (1977), Papaloizou & Stanley (1986), and Kley (1991
A fairly simple and general way to estimate the same was given recently by Pophar
& Narayan (1995) who considered the accretion disk boundary layer problem i
cataclysmic variables. Significantly, these authors have stressed that most of th
decrease in the boundary layer luminosity will occur in the early stages of spin-up, whe
the star is rotating slowly, *rather* than the late stages when it is approaching limitin
break up rotation rates The scenario that we consider in this paper corresponds to th
latter stage. Therefore, for our purpose, the formula for the boundary layer luminosit
that we have used is expected to be adequate This point is elaborated in §4

3.   Equation of state and rotation-induced changes in structure

The structure of neutron stars depends sensitively on the equation of state at higl
densities, especially for density regions $\gtrsim 10^{14}\,\mathrm{g\,cm}^{-3}$ There is no general consensu
on the exact behaviour of the equation of state at these high densities. For our purpos
here we choose the following six equations of state (1) Pandharipande (N) (neutroi
matter) model, based on the lowest order constrained variational method using Rei
potentials (Pandharipande 1971a), (2) Pandharipande (Y) (1971b) hyperonic matter; (3
Bethe-Johnson model V (N) for neutron matter (Bethe & Johnson 1974) which use:
improved phenomenological potentials; (4) Walecka (1974) model for neutron matter
using scalar-vector interactions in a field theoretical framework; (5) Wiringa
UV14 + UVII model for neutron-rich matter in beta equilibrium – a variationa
calculation incorporating the three-body interactions (Wiringa, Fiks & Fabrocin
1988), and (6) neutron-rich matter in beta equilibrium, based on the chiral sigma mode
(Sahu, Basu & Datta 1993) Of these, models (1) and (2) are 'soft' equations of state anc
(4) and (6) are rather 'stiff' ones, while the models (3) and (5) are roughly intermediate in
'stiffness'

The composite equation of state to determine the neutron star structure was
constructed by joining the selected high density equation of state to that of Negele &
Vautherin (1973) for the density range $(10^{14} - 5 \times 10^{10})\,\mathrm{g\,cm}^{-3}$, Baym, Pethick
& Sutherland (1971) for densities down to $\sim 10^3\,\mathrm{g\,cm}^{-3}$ and Feynman, Metropolis &
Teller (1949) for densities less than $10^3\,\mathrm{g\,cm}^{-3}$.

For a fixed central density (and a chosen equation of state model), the fractional changes in the gravitational mass ($\Delta M/M$) and radius ($\Delta R/R$) of the neutron star due to the rotation induced spherical deformation are proportional to Ω^2 (Ω is the angular velocity of the star as seen by a distant observer), and can be (numerically) obtained from a knowledge of the radial distributions of the mass and pressure perturbation terms, $m_0(r)$ and $p_0(r)$ (HT; Datta & Ray 1983; Datta 1988). The non-rotating mass (M) and radius (R) are obtained by numerically integrating the relativistic equations for hydrostatic equilibrium (see e.g. Arnett & Bowers 1977). The changes ΔM and ΔR are given by

$$\Delta M = m_0(R) + J^2/R^3, \tag{32}$$

$$\Delta R = -\left.\frac{p_0(\rho+p)}{dp/dr}\right|_{r=R}, \tag{33}$$

where $p(r)$ and $\rho(r)$ are the pressure and the total mass-energy density at the radial distance r from the center of the star.

For purpose of estimating the angular momentum evolution of the accreting neutron star (discussed in the next section), we need to know the baryonic mass of the rotating neutron star. The rotation induced change in the baryonic mass (denoted by ΔM_B) is conveniently written as

$$\Delta M_B = \Delta E_B + \Delta M, \tag{34}$$

where ΔE_B is the rotation induced change in the binding energy of the star (HT):

$$\Delta E_B = -J^2/R^3 + \int_0^R 4\pi r^2 B(r)dr, \tag{35}$$

where

$$B(r) = (\rho+p)p_0\left\{\frac{d\rho}{dp}\left[\left(1-\frac{2m}{r}\right)^{-1/2}-1\right] - \frac{d\varepsilon}{dp}\left(1-\frac{2m}{r}\right)^{-1/2}\right\}$$

$$+ (\rho-\varepsilon)\left(1-\frac{2m}{r}\right)^{-3/2}\left[\frac{m_0}{r}+\frac{1}{3}j^2r^2\bar{\omega}^2\right]$$

$$- \frac{1}{4\pi r^2}\left[\frac{1}{12}j^2r^4\left(\frac{d\bar{\omega}}{dr}\right)^2 - \frac{1}{3}\frac{dj^2}{dr}r^3\bar{\omega}^2\right], \tag{36}$$

and $\varepsilon = \rho - m_B n$ is the density of internal energy, with $n(r)$ and m_B denoting respectively, the baryonic density and rest mass

Density profiles of neutron stars are remarkably flat out to $r = (0.8–0.85)R$ (Datta *et al.* 1995). Therefore, the concept of rotational secular instability in the context of Maclaurin spheroids (Chandrasekhar 1969) is a relevant approximation when considering the rotational stability of neutron stars. For a uniformly rotating homogeneous spheroid, this instability corresponds to an angular velocity $\Omega = \Omega_s$, given by

$$\frac{\Omega_s^2}{2\pi G\bar{\rho}} = 0.18, \tag{37}$$

where $\bar{\rho}$ is the average density of the star. The quantity Ω_s sets a rough limit up to which the neutron star can be spun up, before the onset of rotational instabilities.

Bhaskar Datta et al

Table 1. Changes in Neutron Star Properties due to Rotation.

EOS Model (1)	ρ_c (g cm⁻³) (2)	$M/M_\odot$ (3)	R (km) (4)	Ω_s (rad s⁻¹) (5)	$\Delta M/M$ (6)	$\Delta R/R$ (7)	r_{orb} (km) (8)	r'_{orb} (km) (9)
Pandharipande (N)	1 24E15	1 062	10 390	5 82E3	0 085	0 033	9 408	7 936
	1.50E15	1.241	10 150	6.52E3	0 080	0 029	10 990	9 244
	1 75E15	1 367	9 936	7 07E3	0.076	0.025	12 110	10 140
	1.83E15	1.400	9 867	7 23E3	0 074	0 024	12 400	10 360
	3.88E15	1 658	8 585	9 69E3	0 054	0 011	14 690	11 860
Pandharipande (Y)	2 18E15	1 045	8 767	7 45E3	0.073	0 029	9 257	7 817
	3 26E15	1 289	8.096	9 33E3	0 064	0 019	11 420	9 477
	3 88E15	1 354	7.796	1.01E4	0 059	0 016	11 990	9 855
	4 79E15	1 400	7 437	1 10E4	0 054	0 012	12 400	10 070
	5 74E15	1.414	7.153	1 18E4	0 050	0 010	12 530	10 080
Bethe–Johnson V (N)	9 50E14	1 003	11 100	5 12E3	0 089	0 035	8.885	7 470
	1 24E15	1 292	10 830	6 04E3	0 084	0 029	11 450	9 627
	1 25E15	1 303	10.820	6 08E3	0 084	0 029	11 540	9 712
	1.37E15	1.400	10 690	6 41E3	0 081	0 027	12 400	10 410
	2.18E15	1 683	10 020	7 75E3	0 067	0 018	14 910	12 280
	3 26E15	1 757	9 304	8 84E3	0 057	0 012	15 560	12 620

Table 1. (continued).

EOS Model (1)	ρ_c (g cm^{-3}) (2)	$M/M_\odot$ (3)	R (km) (4)	Ω_s (rad s^{-1}) (5)	$\Delta M/M$ (6)	$\Delta R/R$ (7)	r_{orb} (km) (8)	r'_{orb} (km) (9)
Walecka	6.50E14	1.035	12 200	4 52E3	0 098	0 037	9 168	7 682
	7.48E14	1.279	12.240	5.00E3	0.095	0 033	11.330	9.522
	7 75E14	1.342	12.240	5.12E3	0 094	0 032	11 890	9 994
	8 02E14	1 400	12 240	5 23E3	0 094	0 031	12 400	10 430
	2 18E15	2 243	11.060	7 71E3	0 059	0 009	19 870	15 850
Wiringa UV14 + UVII	8 50E14	1.053	11 110	5 25E3	0 095	0 035	9.328	7 837
	9 72E14	1 282	11 120	5 78E3	0 092	0 031	11 360	9 550
	1 00E15	1 330	11.120	5.88E3	0 091	0 031	11 780	9 899
	1.04E15	1 400	11.120	6 04E3	0 090	0 028	12.400	10 410
	2.70E15	2 188	9.875	9.02E3	0 053	0 004	19 380	15 120
Chiral Sigma Model	3 50E14	1.017	14.320	3 52E3	0 109	0 041	9.009	7.463
	3.85E14	1 261	14 620	3 80E3	0 110	0 038	11.170	9 345
	4 00E14	1 360	14 740	3 90E3	0 110	0 037	12.050	10.110
	4.06E14	1 400	14 780	3 94E3	0.109	0 037	12.400	10.400
	1.26E15	2 592	14 220	5 68E3	0 069	0 015	22 960	18 670

Table 2. Disk and Boundary Layer Luminosities.

EOS Model (1)	$M/M_\odot$ (2)	$M'/M_\odot$ (3)	E_D (m_0c^2) (4)	E'_D (m_0c^2) (5)	$\Delta E/E$ (6)	E_S (m_0c^2) (7)	E'_S (m_0c^2) (8)	$\Delta E/E$ (9)
Pandharipande (N)	1.062	1.152	0.056	0 066	0.1687	0.108	0.105	−0 0259
	1.298	1.400	0.057	0.073	0 2841	0 156	0.148	−0 0523
	1.400	1.504	0.057	0.074	0 2969	0.181	0.172	−0.0473
	1.642	1.738	0.057	0.075	0.3126	0.269	0.259	−0.0378
	1.658	1.748	0.057	0.075	0 3174	0.287	0.276	−0 0391
Pandharipande (Y)	1.045	1 121	0.057	0 071	0.2379	0.138	0.130	−0 0534
	1.289	1.371	0.057	0 074	0 2926	0.215	0.206	−0.0431
	1.319	1.400	0 057	0 074	0.2957	0.228	0 218	−0 0423
	1.400	1 476	0.057	0.075	0 3099	0.276	0.266	−0 0395
	1.414	1 485	0.057	0.075	0 3176	0 298	0.285	−0 0409
Bethe–Johnson V (N)	1 003	1.092	0 053	0.060	0.1347	0.090	0.089	−0 0112
	1.292	1.400	0.057	0.072	0.2542	0.138	0.132	−0 0461
	1 400	1 513	0.057	0.074	0.2919	0.160	0 152	−0.0511
	1.576	1.691	0.057	0.075	0 3030	0.200	0.191	−0 0427
	1.757	1 857	0.057	0.075	0.3155	0.278	0.267	−0 0381

Table 2. (continued).

EOS Model (1)	$M/M_\odot$ (2)	$M'/M_\odot$ (3)	E_D ($m_0 c^2$) (4)	E'_D ($m_0 c^2$) (5)	$\Delta E/E$ (6)	E_S ($m_0 c^2$) (7)	E'_S ($m_0 c^2$) (8)	$\Delta E/E$ (9)
Walecka	1.035	1 136	0.051	0.058	0 1298	0 083	0 083	0 0001
	1.279	1 400	0.057	0.067	0 1905	0 112	0.109	−0 0218
	1 400	1 531	0.057	0.071	0 2399	0 129	0 124	−0 0352
	1.680	1.825	0.057	0.075	0.3123	0.173	0.165	−0 0441
	2.243	2 375	0.057	0.077	0.3405	0.309	0.299	−0.0342
Wiringa UV14 + UVII	1.053	1 153	0 055	0 063	0 1541	0.097	0 096	−0.0114
	1 282	1.400	0 057	0.071	0 2430	0 131	0 126	−0 0384
	1 400	1 526	0 057	0 074	0.2896	0 150	0 144	−0 0439
	1 680	1 817	0 057	0 075	0 3148	0 201	0 194	−0 0359
	2 188	2.305	0.057	0.078	0 3653	0 355	0.342	−0 0369
Chiral Sigma Model	1 017	1.128	0.045	0 051	0 1140	0.066	0.067	0.0189
	1 261	1.400	0 052	0 059	0 1455	0 085	0.085	0.0075
	1.400	1 553	0 055	0 064	0.1686	0.097	0.097	−0.0010
	1 644	1 817	0.057	0.070	0 2260	0 120	0 118	−0 0224
	2.592	2 771	0.057	0.076	0 3274	0 263	0.255	−0 0324

The prescription mentioned earlier to calculate the mass and radius of a rotating relativistic star is valid only for rotation rates that are 'slow' in comparison to Ω_c Hartle & Thorne (1968) constructed 'slowly' rotating neutron star models all the way up to $\Omega = \Omega_c$ for the Harrison-Wheeler and Tsuruta-Cameron equations of state. Here we shall only consider rotating neutron stars with $\Omega = \Omega_s$ because of the secular instability consideration, and will employ the newer equation of state models mentioned earlier, these models will then illustrate the maximal reasonable effects of rotation. Since $\Omega_s = (0\cdot27)^{1/2}\,\Omega_c$, the models constructed by us are adequately treated in the limit of 'slow' rotation. To treat the maximal *possible* effects of rotation, one has to go beyond this limit, and use a technique similar to that employed by Cook *et al.* (1994a, b for very rapidly (but still uniformly) rotating neutron stars, they determined that spin-up to the millisecond pulsar regime is possible for a wide range of equations of state

4. Results and conclusions

In Table 1 we give the neutron star properties calculated for the various equations o state as a function of the central density (ρ_c). Columns (3) and (4) list the non-rotating mass and radius Column (5) gives the corresponding value of Ω_s and columns (6) and (7) give the differences between the rotating and non-rotating neutron star mass and radius. Column (8) gives the non-rotating values of r_{orb} while column (9) shows how r_{orb} decreases due to rotation. Typical increases in mass are (5–11)%, in radius $\leqslant 4\%$ while r_{orb} decreases between 15% and 25%

In the second and third columns of Table 2 we give values of the non-rotating mass M and the rotationally enhanced mass M' for a maximal reasonable rotation rate ($\Omega = \Omega_s$) Columns (4) and (7) show the disk and boundary layer luminosities for non-rotating configurations (E_D and E_S respectively) The values of E'_D and E'_S, including rotational effects treated consistently within the HT framework, are given in columns (5) and (8). All values of luminosity listed in the table are in units of the baryonic rest mass. The boundary layer luminosity values listed in Table 2 do not include corrections for the energy that goes into spinning up the neutron star. We have made estimate of this correction following the prescription of Popham & Narayan (1995) for the case of $1\cdot4\,M_\odot$ neutron star corresponding to the EOS model by Wiringa *et al* (1988) This is shown in Fig. 1 which is a plot of the rotational energy correction E_{rot} in units of the particle rest mass vs. the stellar rotation rate Ω. It is clear from this figure that the rotational energy correction to the boundary layer luminosity tends to become unimportant as the angular velocity approaches very high values. For $\Omega = \Omega_s$, $E_{rot} \sim 0\cdot048$; this is an order of magnitude less than the boundary layer luminosity given in Table 2. Therefore the neglect of rotational energy correction to calculate E'_s for the neutron star rotating at the limiting Ω as considered by us does not result in a gross overestimate

We find that as M' increases, the luminosity in the boundary layer increases monotonically. The disk luminosity increases in the rotational case as compared to the static case; the increase, illustrated in column (6), is most significant ($\gtrsim 30\%$) for high M' values. The fractional changes $\Delta E_s/E_s$ values (column (9)), however, exhibit a non-monotonic behaviour with increasing M', though they typically decrease by a few per cent Further, as is well known, we see that the radius of the innermost stable orbit is less than the static case (where $r_{orb} = 6M$) for all equations of state considered.
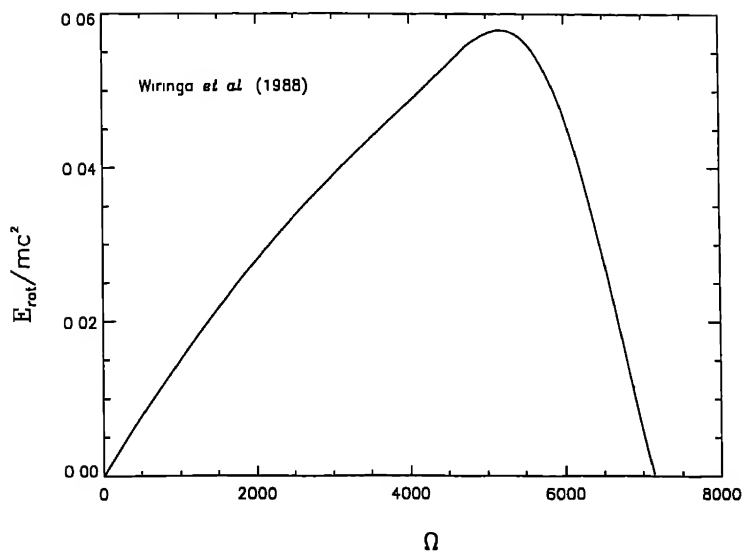
Figure 1. Rotational energy correction E_{rot}/mc^2 to the boundary layer luminosity as a function of the stellar rotation rate Ω.

We now make a few remarks about the angular momentum evolution of the accreting neutron star In performing the angular momentum evolution calculations, we have made the following additional assumptions:

■ The central density of the neutron star does not change with mass accretion. This is a reasonable assumption to make because for a static, stable neutron star, while the central density increases with increasing mass, the rotation tends to 'decrease' the central density Thus if the total accreted mass is not large, the effect of rotation will nearly compensate for the effect of accretion on the central density;

■ The mass accretion rate is equal to dM_B/dt as in KW, but with the difference that rotational effects have been taken into account, that is, $M_{acc} = dM'_B/dt$,

■ The maximum angular momentum for a particular neutron star configuration is determined by the secular instability limit:

$$\Omega = \Omega_s = (0.27)^{1/2}\Omega_c.$$

KW derived the evolution equation

$$\frac{dJ}{dM'} = \tilde{l}(r(M'))\frac{dM'_B}{dM'} = 2M'a\frac{dM'_B}{dM}, \tag{38}$$

and solved it under the simplifying assumptions

$$M' \simeq M, \quad \frac{dM'_B}{dM'} \simeq \frac{dM_B}{dM}$$

For dM_B/dM, KW used a fit to the values of M and R taken from Arnett & Bowers (1977) Here, we solve equation (38) numerically, incorporating the effect of rotation as

Bhaskar Datta et al

Table 3. Gravitational and Baryonic Masses as Functions of Angular Momentum.

EOS Model (1)	ρ_c (g cm^{-3}) (2)	$M/M_\odot$ (3)	$M'/M_\odot$ (4)	$M_B'/M_\odot$ (5)	J (g cm^2 s^{-1}) (6)
Pandharipande (N)	1 83E15	1 400	1 400	1 567	0 000E00
			1 413	1.578	2.526E48
			1 426	1 589	3 648E48
			1 438	1 599	4.420E48
			1 467	1.623	5 823E48
Pandharipande (Y)	4 79E15	1 400	1 400	1 615	0 000E00
			1.416	1 627	3 269E48
			1.432	1.639	4 660E48
			1.448	1 652	5 772E48
			1 466	1.665	6 746E48
Bethe–Johnson V (N)	1.37E15	1 400	1 400	1.556	0 000E00
			1 420	1 572	3.139E48
			1 440	1 589	4 424E48
			1 460	1 606	5 422E48
			1.500	1 639	6 992E48
Walecka	8.02E14	1 400	1 400	1 671	0 000E00
			1 430	1.699	3.760E48
			1.486	1.750	6 318E48
			1.500	1.764	6.844E48
			1.516	1.779	7 370E48
Wiringa UV14 + UVII	1 04E15	1.400	1.400	1.562	0.000E00
			1 420	1 578	3.050E48
			1.443	1 598	4.538E48
			1.467	1.618	5 655E48
			1 512	1 656	7.291E48
Chiral Sigma Model	4 06E14	1 400	1 400	1.521	0 000E00
			1.434	1.549	3.975E48
			1 472	1.581	5 760E48
			1.505	1.609	6.976E48
			1 539	1 638	8.031E48

outlined above. We assume that for a central density that gives a gravitational mass of $1 \cdot 4 M_\odot$ in the non-rotating case, $J = \Omega = 0$, and we then vary Ω from zero to Ω_s The results are presented in Table 3; these should be compared with Table 1 of KW.

From Table 3, we see that for each equation of state, a plot of M_B' vs M' gives an almost constant slope We solve equation (38) using the boundary condition $J = 0$ for
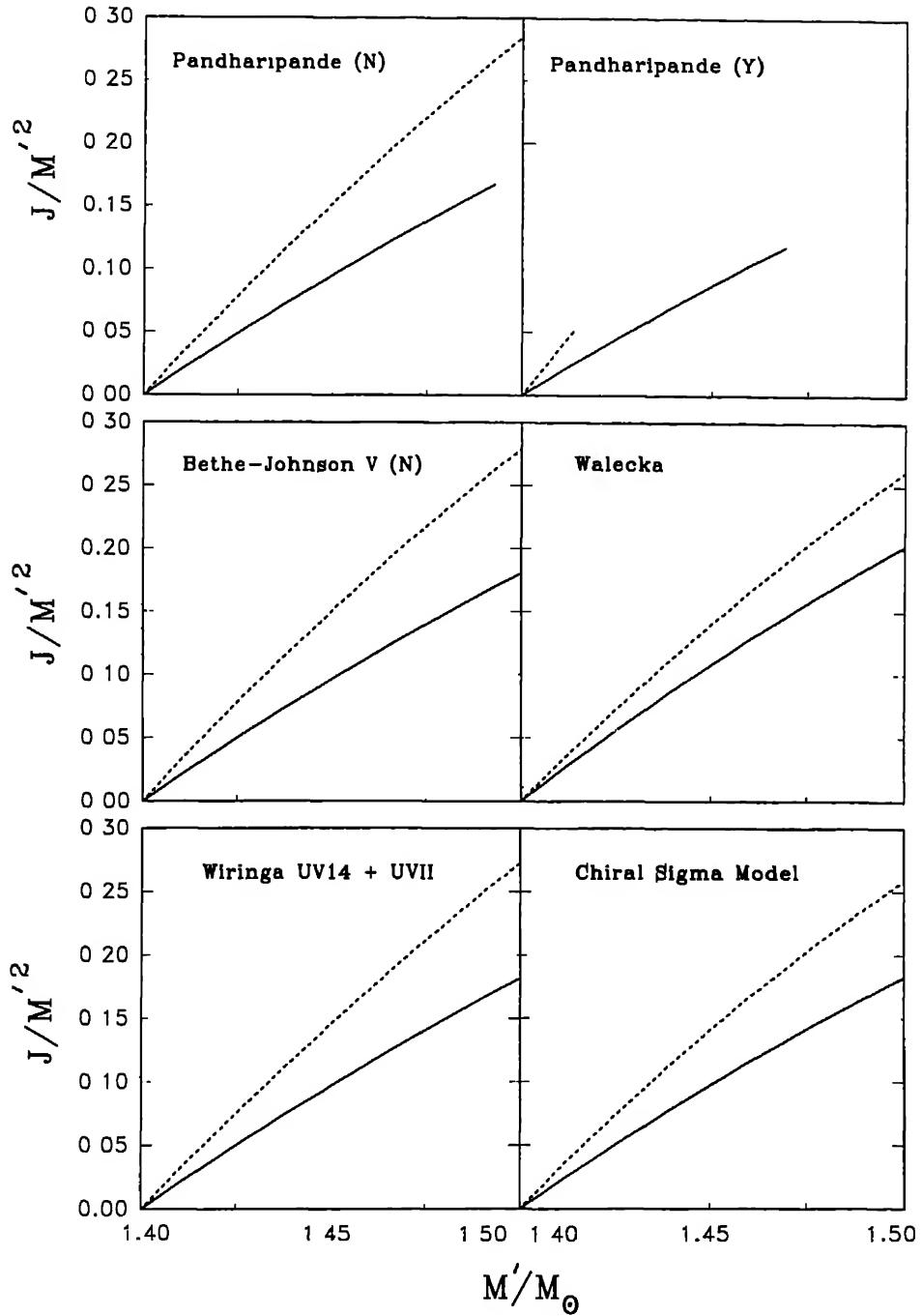
Figure 2. Evolution of the dimensionless angular momentum, $\tilde{j} = J/M^2$, of a neutron star with the accretion of mass, for six representative equations of state. The dashed curves correspond to the approach of KW, and the solid curves to our more self-consistent approach

$M' = 1.4\,M_\odot$ configuration We integrate it either until $M' = M'_{max}$, where M'_{max} is mass corresponding to J_{max} or until $J = J_{max}$ (the last entry for J in Table 3) whicht comes first

The results of our computations for the angular momentum are illustrated in Fit The x-axis corresponds to $M'/M_\odot$ and the y-axis to J/M'^2 The dashed cur correspond to the angular momentum evolution computed in the fashion of KW, w the solid curves represent the results of the more self-consistent (numerical) estime made by us as described above. The graphs indicate a slower rate of evolution of accreting neutron star's angular momentum in the rotational case as compared to case where rotational effects are not treated

There are two factors contributing to the slower evolution of the angular moment that we obtain The less significant one is a comparatively smaller value of dM'_B/d. The more significant factor is that the angular momentum $\tilde{l}$ of the accreted particli systematically less in the rotational case. Our calculations include the fact that infall material co-rotating with the neutron star has a smaller cross-section for accretion th does counter-rotating infalling matter, so that the effective angular momentum reduced (e g, Misner, Thorne, & Wheeler 1974) Within the realm of overlap of c approximations, the results we find agree reasonably well with those of Cook *et* (1994a, b) for accretion induced changes of angular momentum

5. Discussion

In presenting the results in the previous section, we have made the implicit assumptic that the magnetic field of the neutron star is too small to affect accretion Clear a quantitative estimate of this limit is in order The Alfvén radius (r_A), is defined by tl relationship (see Lamb, Pethick & Pines 1973)

$$\frac{B^2(r_A)}{8\pi} = \rho(r_A)v^2(r_A),\tag{3}$$

where ρ and v are respectively the density and radial velocity in the accretion dis determines the location at which magnetic pressure channels the flow from a disk int an accretion column structure above the magnetic poles. Lamb, Pethick & Pines (197 show that

$$r_A \lesssim 2.6 \times 10^8 \left[\frac{\mu_{30}^{4/7}(M/M_\odot)^{1/7}}{L_{37}^{2/7} R_6^{2/7}} \right] \text{cm},\tag{4(}$$

where $\mu_{30} = B_0 R^3/10^{30}\,\text{G cm}^3$, L_{37} is the total luminosity in units of 10^{37} erg s$^-$ $R_6 = R/10^6\,\text{cm}$ and B_0 is the magnetic field on the surface of the neutron star in gaus: The condition that $r_A < R$ implies that (taking $M = 1.4\,M_\odot$ and $R_6 = 1$)

$$B_0 < 5.5 \times 10^7 L_{37}^{1/2},\tag{41}$$

and is necessary for the scenario we have discussed to be fully self-consistent, but field somewhat higher than this value will not greatly modify our conclusions

In our notation, $L = (E'_D + E'_S)\dot{M}c^2$, with $\dot{M}$ the accretion rate According to ou calculations, typical values for $(E'_D + E'_S)$ are of the order of 0 2 The luminosity $L_{37} =$

would then correspond to an accretion rate $\sim 5 \cdot 6 \times 10^{16}$ g s^{-1} Such accretion rates are close to the ones estimated in X-ray binaries (Ghosh & Lamb 1991), so that our computations are relevant for systems with significant accretion on to old neutron stars whose surface magnetic fields have undergone substantial decay (to about $10^8 G$).

Under these circumstances of weak neutron star magnetic fields, we have shown that an incorporation of rotational effects always increases the disk luminosity, usually decreases the boundary layer luminosity, and always reduces the rate at which the neutron star's angular momentum rises with accreted mass These effects are large enough to merit their consideration in analyses of observations of low-mass X-ray binaries.

Acknowledgement

References

Alpar M A., Cheng, A F, Ruderman, M A, Shaham, J 1982, *Nature*, **300** 728
Arnett, W D, Bowers, R L 1977, *Astrophys. J. Suppl*, **33**, 415.
Baym, G, Pethick, C J., Sutherland, P. G 1971, *Astrophys. J*, **170**, 299
Bethe, H A, Johnson, M B 1974, *Nucl Phys* **A230**, 1
Bhattacharya, D, van den Heuvel, E P J. 1991, *Phys Rep.*, **203** 1
Chandrasekhar, S 1969, *Ellipsoidal Figures of Equilibrium* (New Haven Yale University Press)
Cook, G B, Shapiro, S L, Teukolsky, S A. 1994a, *Astrophys. J*, **423**, L117
Cook, G B, Shapiro, S L, Teukolsky, S A 1994b, *Astrophys J*, **424**, 823
Datta, B, Ray, A 1983, *Mon. Not R. astr. Soc.*, **204**, 75.
Datta, B 1988, *Fund. Cosmic Phys*, **12**, 151
Datta, B, Thampan, A V, Bhattacharya, D. 1995, *J Astrophys Astr.*, **16**, 375
Feynman, R. P., Metropolis, N, Teller, E, 1949, *Phys. Rev.*, **75**, 1561
Ghosh, P, Lamb, F. K, Pethick, C J 1977, *Astrophys J*, **217**, 578.
Ghosh, P., Lamb, F. K 1991 in *Neutron Stars Theory and Observations*, eds J Ventura & D. Pines, (Dordrecht Kluwer Acad. Publ) p 363
Hartle, J. B, Thorne, K. S 1968, *Astrophys. J.*, **153**, 807 (HT).
Kley, W 1991, *Astr Astrophys*, **247**, 95
Kluźniak, W, Wagoner, R V 1985, *Astrophys. J*, **297**, 548 (KW)
Kluźniak, W 1987, *Ph D Thesis*, Stanford Univ.
Lamb, F K, Pethick, C. J, Pines, D 1973, *Astrophys J.*, **184**, 271
Misner, C W, Thorne, K. S, Wheeler, J A 1974, *Gravitation* (San Francisco Freeman).
Negele, J W, Vautherin, D 1973, *Nucl Phys*, **A207**, 298
Paczyński, B 1987, *Nature*, **327** 303
Pandharipande, V. R. 1971a, *Nucl Phys*, **A174**, 641
Pandharipande, V R. 1971b, *Nucl Phys*, **A178**, 123
Papaloizou, J. C. B., Stanley, G Q. G 1986, *Mon Not R. astr Soc*, **220**, 593.
Popham, R., Narayan, R 1995, *Astrophys J*, **442**, 337

Priedhorsky, W. 1986, *Astrophys J*, **306**, L97.
Radhaknshnan, V, Srinivasan, G 1982, *Current Sci*, **51**, 1096
Sahu, P K, Basu, R, Datta, B 1993, *Astrophys J.*, **416**, 267
Syunyaev, R A, Shakura, N I 1986, *Sov Astr Lett*, **12**, 117 (SS)
van Paradijs, J 1991 in *Neutron Stars Theory and Observations*, Eds. J Ventura & D Pi
    (Dordrecht Kluwer Acad Publ), p 245
Walecka, J D 1974, *Ann Phys.*, **83**, 491
Wirmga, R B, Fiks, V, Fabrocini, A 1988, *Phys Rev. C*, **38**, 1010

A Numerical Survey of Neutron Star Crustal Density Profiles

B. Datta[1,3], A. V. Thampan[1] & D. Bhattacharya[2]
[1] *Indian Institute of Astrophysics, Bangalore 560 034, India*
[2] *Raman Research Institute, Bangalore 560 080 India.*
[3] *Visiting Professor Raman Research Institute, Bangalore 560 080 India*

Abstract. An accurate numerical survey of the density profiles corresponding to the crusts of neutron stars for representative equation of state models is presented This will find application in calculations of thermal and magnetic evolution of neutron stars

Key words: Stars neutron—crusts. neutron star

1. Introduction

The crust of a neutron star refers to a region, near the surface, that is composed of mainly neutron-rich bare nuclei which interact electrostatically and are arranged in a lattice The outer crust has small admixtures of free electrons and the inner crust has, in addition to electrons, 'drip' neutrons populating continuum states and permeating the nuclear lattice space. With increasing depth from the surface, and hence with increasing density, the neutron-to-proton ratio of the nuclei increases till a point is reached where the nuclei 'dissolve' and the composition is largely a homogeneous sea of neutrons This point is characterized as the crust bottom Although the crusts comprise a relatively small fraction of the total radius of the neutron star (usually about 10%), their importance derives from the fact that these possess interesting transport properties, and are believed to play a central role in a variety of directly and indirectly observable properties of neutron stars. The former include glitches, X-ray emission, and the latter concern the evolution of neutron star magnetic fields (and hence the evolution of pulsars) and possible changes in the neutron star structure and composition due to long-term accretion from a binary companion star In order to understand all these and related phenomena quantitatively, it is imperative to have accurate knowledge of the radial distribution of the density in the crust

Calculations suggest that neutron stars possess a more or less flat density profile from the centre to the crust bottom (Arnett & Bowers 1977; Datta 1988), and that the crust contains negligible mass in comparison to the mass in the rest of the star The crust bottom (which is the boundary layer between the inner crust and the interior region) according to realistic calculations, is roughly equal to the equilibrium nuclear matter density, $\simeq 2.4 \times 10^{14} \, \mathrm{g \, cm^{-3}}$. This is about an order of magnitude less than the central densities obtained in neutron stars Across the crust, however, the density drop is extremely sharp – about fourteen orders of magnitude. Clearly, an accurate knowledge of the crustal density profile needs an accurate numerical treatment while integrating the equilibrium structure equations in this region of extremely rapid density

375

variation The equation of state (EOS) of neutron star matter is the key input par‹
in all these calculations, the crustal properties depending sensitively on which p‹
lar EOS model is adopted to describe the neutron star interior In general, the stif
EOS, the more the extent of the crust. In this paper, we present a numerical sur
crustal density profiles for several neutron star configurations, and for a represen
choice of the EOS models

2. Equations of state

The structure of neutron star depends sensitively on the EOS at high den‹
Although the main composition of degenerate matter at densities $\gtrsim 2.4 \times 10^{14}$ g c
that characterize neutron star interiors, is expected to be dominated by neut
significant admixtures of other elementary particles (such as pions, muons
hyperons) are not ruled out. A persistent problem in determining the EOS (na‹
pressure as a function of density) of such high density matter is what to choose fo
interaction among the various particles, for which reliable experimental informati
not available All calculations involve either extrapolations from known nuclear m.
properties or field theoretical approaches Another unresolved problem is what m
body technique is adequate for the purpose of evaluating the higher order correla
terms for the pressure In this paper we do not address these problems, but choos‹
our purpose, eight EOS models based on representative neutron star matter interac
models A brief description of these is given below

A. Pandharipande (neutron matter): Pandharipande (1971a) studied behaviou‹
dense neutron matter using a many-body theory based upon the variational appro
suggested by Jastrow (1955). The two-body wave function was taken as satisfy
a simplified form of the Bethe-Goldstone equation, in which, terms representing
Pauli exclusion principle were omitted but simulated by imposing a 'healing' constr‹
on the wave function Instead of a state-dependent correlation function, an average ‹
used with spin dependence. To describe the nuclear interaction, the Reid nucle‹
nucleon potential was used (Reid 1968). This potential model is now considered to
inadequate as it does not fully describe known nuclear matter properties

B. Pandharipande (hyperonic matter): At high densities that prevail in neutron s‹
interiors, it is possible that elementary particles heavier than neutrons, such as hypero‹
may also be present. The suggestion that hyperons may be additional baryonic constit
ents of neutron star interiors was first made by Ambartsumyan & Saakyan (1960) bas‹
on energetic arguments. Although our knowledge of hyperonic interactions is meag
(primarily because of lack of experimental data), there have been several theoretic
attempts aimed at deriving the EOS of baryonic liquid made up of neutrons, proton
hyperons (Λ, Σ^0) One of the early such attempts is due to Pandharipande (1971b), wh
assumed the hyperonic potentials to be similar to the nucleon-nucleon potentials, b‹
altered suitably to represent the different isospin states The many-body method adopte
to derive the EOS was similar as in the case A. Several EOS models of hyperonic matt‹
have since been proposed by different authors. However, this still remains an ope
problem because our knowledge of hyperon-nucleon and hyperon-hyperon interac‹
tions and their coupling constants have large uncertainties

C. Bethe–Johnson: Bethe & Johnson (1974) devised phenomenological potentials for nucleon-nucleon interaction that have more realistic short-range behaviour than the Reid potentials These authors then used the lowest order constrained variational method as given by Pandharipande (1971a) to calculate the EOS of neutron star matter. The work of Bethe & Johnson (1974) consists of two different parts: (1) determination of the EOS for a pure neutron gas and (2) derivation of a hyperonic equation of state For purpose of illustration here, we have chosen their EOS model V (neutron matter).

D. Walecka: The exchange of vector and scalar mesons among nucleons is known to provide the short-range repulsion and intermediate-range attraction in the nucleon-nucleon potential. The effective interaction will be characterized by the meson parameters, such as their masses and coupling constants. If these parameters are specified, the meson wave functions can be easily solved as a function of density (assuming the wave functions to be space-time independent). From this, one can evaluate the stress tensor, which then provides the EOS. Walecka (1974) chose the meson parameters so as to reproduce the binding energy of nuclear matter (assumed to be -15.75 MeV/nucleon) at a saturation density of 0 193 nucleons fm^{-3}. More recent analysis of experimental data suggests the nuclear matter binding energy to be -16.3 MeV/nucleon and a saturation density of 0 153 nucleons fm^{-3} (Moller *et al* 1988) The EOS model of Walecka corresponds to pure neutron matter Both the scalar and vector mesons are assumed to have zero isospin by Walecka, so the model does not give the right asymmetry energy for nuclear matter.

E. Friedman-Pandharipande (neutrons): This model (Friedman & Pandharipande 1981), is also based on the lowest order constrained variational method. However, instead of the Reid potentials, the authors have made use of an improved phenomenological nucleon-nucleon potential containing a two-body part as well as three-body correlations This interaction fits the nucleon-nucleon scattering cross-section data, deuteron properties, and also the nuclear matter properties rather well.

F. Wiringa, Fiks & Fabrocini (1988): These authors gave a model of EOS for dense nuclear and neutron matter which includes three-nucleon interactions. This is a non-relativistic approach based on the variational method. The three-body potential considered by the authors includes long-range repulsive parts that are adjusted to give light nuclei binding energies and nuclear matter saturation properties. This work represents an improvement over the calculation of Friedman & Pandharipande (1981) regarding the long-range attraction term in the Hamiltonian. The authors have given three models We consider here their model for beta-stable case UV14 + UVII (neutrons, protons, electrons and muons).

G. Prakash, Ainsworth & Lattimer (1988) proposed EOS models for neutron stars, based on an extrapolation of the energy per particle of symmetric nuclear matter. The approach is empirical, and involves several parameters. The total energies are obtained by inclusion of the nucleon kinetic energy and the effect of finite forces between nucleons Four models have been suggested by the authors, we use model 1 for our purpose.

H. Sahu, Basu & Datta (1993) gave a field theoretical EOS for neutron-rich matter in beta equilibrium based on the chiral sigma model. The model includes an isoscalar vector

field generated dynamically and reproduces the empirical values of the nuclear
saturation density and binding energy and also the isospin symmetry coefficie
asymmetric nuclear matter. The energy per nucleon of nuclear matter according to
Basu & Datta (1993) is in very good agreement, up to about four times the equilib
nuclear matter density, with estimates inferred from heavy-ion collision experimenta

Models A, B and G are relatively soft EOS, models E, C and F are roughly interm
in their stiffness whereas models D and H are very stiff EOS. The composite EOS f
entire span of neutron star densities was constructed by joining the selected high d
EOS to that of Negele & Vautherin (1973) for the density range $(10^{14} - 5 \times 10^{10})$g ε
Baym, Pethick & Sutherland (1971) for densities down to $\sim 10^3$ g cm^{-3} and Feyr
Metropolis & Teller (1949) for densities less than 10^3 g cm^{-3}.

3. Calculations

The Tolman-Oppenheimer-Volkoff (Oppenheimer & Volkoff 1939) equations that
be integrated numerically to obtain stable, non-rotating neutron star structure a

$$\frac{dm}{dr} = 4\pi r^2 \rho$$

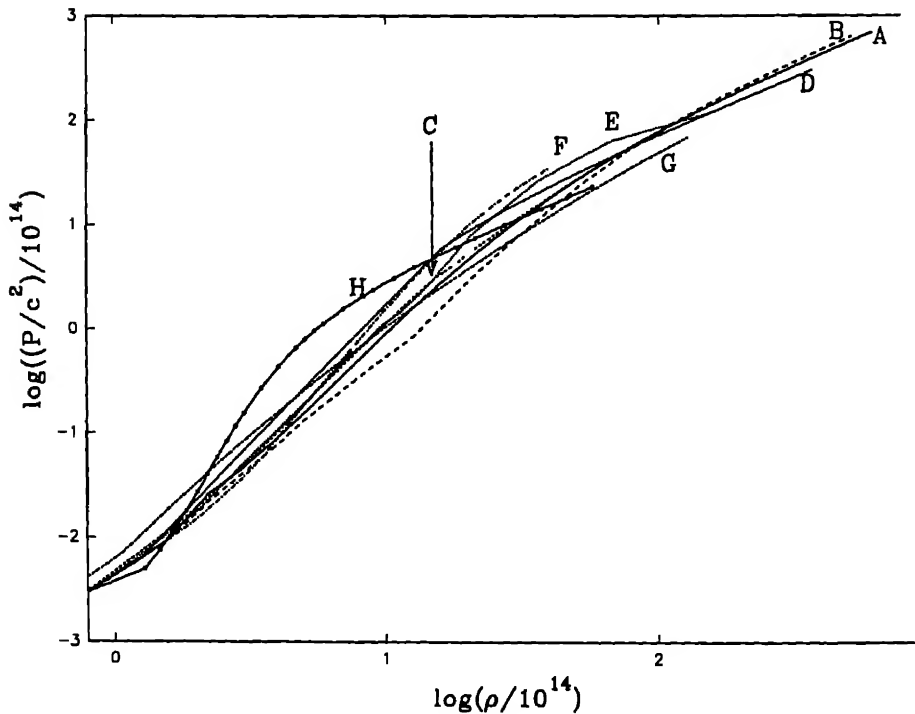$$\frac{dP}{dr} = -\frac{G(m + 4\pi r^3 P/c^2)(\rho + P/c^2)}{r(r - 2\,Gm/c^2)},$$

Figure 1. Pressure as a function of density for the EOS models (A–H)

Table 1. Neutron star structure parameters for the EOS Models (A–H)

EOS	$M/M_\odot$	R (km)	ρ_c (g cm^{-3})	Δ (km)	M_{cr}/M
Pandharipande	1.330	10 006	$1\,669E+15$	0 963	$3\,024E-02$
(neutrons)	1 400	09 867	$1\,830E+15$	0 858	$2\,537E-02$
	1.658	08 492	$4\,100E+15$	0.404	$8\,031E-03$
Pandharipande	1 330	07 921	$3\,606E+15$	0 484	$9\,189E-03$
(hyperons)	1 400	07 437	$4\,795E+15$	0 361	$5\,863E-03$
	1.414	07 082	$6\,017E+15$	0 300	$4\,426E-03$
Bethe-Johnson	1.330	10 782	$1\,283E+15$	1 149	$3\,945E-02$
Model V (neutrons)	1.400	10 691	$1.373E+15$	1 044	$3\,411E-02$
	1.758	09 200	$3.466E+15$	0 454	$9\,565E-03$
Walecka	1 330	12.252	$7.158E+14$	1 442	$5\,482E-02$
	1 400	12 280	$7\,415E+14$	1 387	$5\,415E-02$
	2 285	11 216	$2\,174E+15$	0 452	$1.040E-02$
Friedman-Pandharipande	1.330	10 824	$1\,332E+15$	1 134	$3\,859E-02$
(neutrons)	1 400	10.701	$1\,413E+15$	1 023	$3.297E-02$
	1 986	09 028	$3.450E+15$	0.307	$5\,531E-03$
Wiringa *et al*	1 330	11 122	$1.000E+15$	1.120	$3.543E-02$
(UV14 + UVII)	1 400	11 115	$1\,043E+15$	1.039	$3.167E-02$
	2 189	09.800	$2.830E+15$	0.294	$4.946E-03$
Prakash, Ainsworth	1 330	11 384	$1.507E+15$	1.702	$7\,376E-02$
& Lattimer Model 1	1.400	10 987	$1.808E+15$	1.456	$5\,781E-02$
	1 510	09 483	$3\,590E+15$	0.901	$2.744E-02$
Sahu, Basu	1 330	14 685	$3\,952E+14$	3.128	$2\,518E-01$
& Datta	1.400	14 761	$4.063E+14$	2.970	$2\,342E-01$
	2 593	14 096	$1\,345E+15$	0.975	$4\,588E-02$

NOTE· In Tables 1–9, the numbers following the letter E represent powers of ten.

where P and ρ stand for pressure and density and m is the gravitational mass contained within a sphere of radius r. The integration of equations (1) and (2) is done for a given EOS which specifies $P(\rho)$, and with initial condition $\rho = \rho_c$, a chosen value for the central density. The numerical integration started from the centre of the star is terminated at the radius of the star, defined as the point where the density $\lesssim 7\,86\,\mathrm{g\,cm^{-3}}$, expected to correspond to the neutron star surface The total gravitational mass is then given by $M = m(R)$.

We integrate equations (1) and (2) simultaneously using Runge-Kutta fourth order method, having an adaptive step size control The step size is adjusted for the required accuracy from a calculation of the local truncation error (Antia 1991) We find that this provides an extremely accurate method to integrate equations (1) and (2) for neutron

B. Datta et al

Table 2. Crustal density profiles Pandharipande (neutrons)

$M = 1330 M_{\odot}$		$M = 1400 M_{\odot}$		$M = 1.658 M$	
$R = 10\,006$ (km)		$R = 9.867$ (km)		$R = 8\,492$ (k	
$(1 - r/R)$	ρ (g cm^{-3})	$(1 - r/R)$	ρ (g cm^{-3})	$(1 - r/R)$	ρ (g c
$0.00000E+00$	$7.866E+00$	$0\,00000E+00$	$7.863E+00$	$0.00000E+00$	$7\,866\lambda$
$1\,13773E-09$	$1.319E+01$	$1\,28891E-09$	$1.360E+01$	$9.91795E-10$	$1\,447\lambda$
$2.39423E-08$	$4\,972E+01$	$2\,23090E-08$	$5\,120E+01$	$1.27579E-08$	$5\,428\lambda$
$1.41172E-07$	$1\,874E+02$	$1.31095E-07$	$1\,927E+02$	$7\,44405E-08$	$2.037E$
$6\,75515E-07$	$7\,066E+02$	$6.21865E-07$	$7\,252E+02$	$3.46816E-07$	$7.642E$
$2\,35836E-06$	$2\,664E+03$	$2.17080E-06$	$2\,730E+03$	$1.19743E-06$	$2.867E$
$6\,95373E-06$	$1.004E+04$	$6.34094E-06$	$1.027E+04$	$3\,47397E-06$	$1\,076E$
$1.94642E-05$	$3.786E+04$	$1.77038E-05$	$3.866E+04$	$9.73952E-06$	$4\,037E$
$5\,14517E-05$	$1\,427E+05$	$4\,67151E-05$	$1\,455E+05$	$2.53765E-05$	$1\,515E$
$1.26075E-04$	$5.382E+05$	$1.14160E-04$	$5.477E+05$	$6.23815E-05$	$5\,683E$
$2\,88548E-04$	$2\,029E+06$	$2\,60880E-04$	$2\,061E+06$	$1.40445E-04$	$2\,132E$
$6\,06912E-04$	$7.649E+06$	$5.47153E-04$	$7\,758E+06$	$2.93273E-04$	$8\,001E$
$1\,14403E-03$	$2.884E+07$	$1.03012E-03$	$2\,920E+07$	$5.56213E-04$	$3\,002E$
$2.05310E-03$	$1.087E+08$	$1.84738E-03$	$1\,099E+08$	$9\,86545E-04$	$1.126E$
$3\,46132E-03$	$4.099E+08$	$3.11233E-03$	$4.136E+08$	$1\,65994E-03$	$4.226E$
$5\,44170E-03$	$1\,545E+09$	$4\,89128E-03$	$1.557E+09$	$2.61038E-03$	$1.586E$
$8.57267E-03$	$5\,826E+09$	$7\,70080E-03$	$5\,859E+09$	$4.10792E-03$	$5\,950E\cdot$
$1\,28894E-02$	$2\,196E+10$	$1.15691E-02$	$2.205E+10$	$6.20721E-03$	$2.233E\cdot$
$1.89605E-02$	$8.280E+10$	$1.70260E-02$	$8.299E+10$	$9\,14044E-03$	$8.377E\cdot$
$2\,54733E-02$	$3\,122E+11$	$2.28786E-02$	$3.124E+11$	$1.22832E-02$	$3.143E\cdot$
$3\,04385E-02$	$1\,177E+12$	$2.73482E-02$	$1.176E+12$	$1\,47004E-02$	$1.179E\dashv$
$3\,39494E-02$	$4\,437E+12$	$3\,05103E-02$	$4.425E+12$	$1.64164E-02$	$4\,425E\dashv$
$4\,02999E-02$	$1\,673E+13$	$3\,62239E-02$	$1.665E+13$	$1.94675E-02$	$1\,660E\dashv$
$5\,34854E-02$	$6\,306E+13$	$4\,81026E-02$	$6\,268E+13$	$2.59768E-02$	$6\,230E\dashv$
$9\,62614E-02$	$2\,400E+14$	$8.69610E-02$	$2.400E+14$	$4.75309E-02$	$2\,400E\dashv$

Note. In the crustal density profiles presented here and in the subsequent tables, the th
mass column corresponds to that of the maximum stable mass.

star configurations varying widely in their density profiles. The method, of course, giv
bulk properties such as masses, radii and moments of inertia that agree with the valu
already reported in the literature.

Table 3. Crustal density profiles Pandharipande (hyperons)

$M = 1\,330\,M_O$		$M = 1\,400\,M_O$		$M = 1\,658\,M_O$	
$R = 7\,921$ (km)		$R = 7\,437$ (km)		$R = 7\,082$ (km)	
$(1 - r/R)$	ρ (g cm^{-3})	$(1 - r/R)$	ρ (g cm^{-3})	$(1 - r/R)$	ρ (g cm^{-3})
$0\,00000E + 00$	$7\,869E + 00$	$0\,00000E + 00$	$7\,873E + 00$	$0\,00000E + 00$	$7.872E + 00$
$1\,07340E - 09$	$1\,386E + 01$	$5\,54109E - 10$	$1.310E + 01$	$7.30479E - 10$	$1.386E + 01$
$1\,67489E - 08$	$5\,212E + 01$	$1\,22270E - 08$	$4\,937E + 01$	$1\,14305E - 08$	$5.206E + 01$
$9.81838E - 08$	$1\,959E + 02$	$7\,20507E - 08$	$1\,861E + 02$	$6\,69361E - 08$	$1.956E + 02$
$4\,63059E - 07$	$7\,366E + 02$	$3\,44856E - 07$	$7\,013E + 02$	$3\,15345E - 07$	$7.349E + 02$
$1\,61124E - 06$	$2\,769E + 03$	$1.21581E - 06$	$2.643E + 03$	$1\,09890E - 06$	$2\,761E + 03$
$4\,69519E - 06$	$1.041E + 04$	$3\,55792E - 06$	$9.961E + 03$	$3.19785E - 06$	$1.037E + 04$
$1\,31881E - 05$	$3\,914E + 04$	$1\,00363E - 05$	$3.754E + 04$	$8\,98933E - 06$	$3\,898E + 04$
$3\,44931E - 05$	$1\,471E + 05$	$2\,63282E - 05$	$1.415E + 05$	$2\,34770E - 05$	$1.464E + 05$
$8\,49483E - 05$	$5\,531E + 05$	$6\,51209E - 05$	$5.333E + 05$	$5\,78740E - 05$	$5.502E + 05$
$1\,92058E - 04$	$2\,079E + 06$	$1\,47600E - 04$	$2.010E + 06$	$1\,30595E - 04$	$2\,067E + 06$
$4.02430E - 04$	$7\,817E + 06$	$3.11479E - 04$	$7.575E + 06$	$2.74208E - 04$	$7\,767E + 06$
$7\,63318E - 04$	$2.939E + 07$	$5\,91571E - 04$	$2.855E + 07$	$5.20308E - 04$	$2.918E + 07$
$1\,35630E - 03$	$1.105E + 08$	$1.05199E - 03$	$1.076E + 08$	$9.30193E - 04$	$1\,096E + 08$
$2\,28591E - 03$	$4.153E + 08$	$1.77814E - 03$	$4.056E + 08$	$1.55724E - 03$	$4.120E + 08$
$3\,59396E - 03$	$1.561E + 09$	$2.80054E - 03$	$1.529E + 09$	$2.45039E - 03$	$1\,548E + 09$
$5\,66066E - 03$	$5\,870E + 09$	$4.42319E - 03$	$5\,761E + 09$	$3.86507E - 03$	$5.815E + 09$
$8\,55549E - 03$	$2.207E + 10$	$6.70178E - 03$	$2.171E + 10$	$5.85049E - 03$	$2\,185E + 10$
$1.25852E - 02$	$8\,296E + 10$	$9.87052E - 03$	$8.183E + 10$	$8.61429E - 03$	$8\,209E + 10$
$1\,70822E - 02$	$3.119E + 11$	$1.34460E - 02$	$3\,084E + 11$	$1.17295E - 02$	$3.084E + 11$
$2.03323E - 02$	$1.173E + 12$	$1\,60261E - 02$	$1\,162E + 12$	$1.39806E - 02$	$1\,159E + 12$
$2\,26843E - 02$	$4\,408E + 12$	$1\,78947E - 02$	$4\,381E + 12$	$1.56106E - 02$	$4.354E + 12$
$2\,68735E - 02$	$1\,657E + 13$	$2\,12047E - 02$	$1.651E + 13$	$1\,84789E - 02$	$1.636E + 13$
$3\,57424E - 02$	$6.230E + 13$	$2\,82703E - 02$	$6.223E + 13$	$2\,46211E - 02$	$6.146E + 13$
$6\,11192E - 02$	$2\,400E + 14$	$4.84971E - 02$	$2\,400E + 14$	$4.24178E - 02$	$2.400E + 14$

4. Results and discussions

The EOS models (A–H) are illustrated in Fig. 1 (which is a plot of pressure versus density) This plot refers to the high density region corresponding to the neutron star interior. We have already mentioned in section 2 the EOS that is used for the crustal region. It is important to note that because of substantial variation in the various EOS

models (A–H), the crustal thicknesses and density profiles are expected to exh
variation even though the crustal EOS is assumed to be the same for all cases.

In Table 1, we have summarized the results for the mass (M), radius (R), cen
density (ρ_c), the crustal thickness (Δ) and the mass contained in the crust as a fractio:
the total gravitational mass (M_{cr}/M) We have done this for three configurations of

Table 4. Crustal density profiles: Bethe-Johnson Model V (neutrons).

| M = 1.330 $M_\odot$ | | M = 1 400 $M_\odot$ | | M = 1.658 $M_\odot$ | |
| R = 10.782 (km) | | R = 10.691 (km) | | R = 9 200 (km) | |
$(1 - r/R)$	ρ (g cm^{-3})	$(1 - r/R)$	ρ (g cm^{-3})	$(1 - r/R)$	ρ (g cm^{-3})
0 00000E + 00	7.865E + 00	0 00000E + 00	7 865E + 00	0 00000E + 00	7 870E +
9 62517E − 10	1 274E + 01	5 12115E − 10	1 193E + 01	1.18152E − 09	1 483E +
2.58471E − 08	4 811E + 01	2.15850E − 08	4.517E + 01	1 38593E − 08	5.561E +
1.52912E − 07	1 817E + 02	1.28431E − 07	1 711E + 02	8 06756E − 08	2.084E +
7.38784E − 07	6 859E + 02	6.31512E − 07	6 479E + 02	3.73427E − 07	7.814E + ·
2 60124E − 06	2.590E + 03	2.25472E − 06	2 454E + 03	1.28236E − 06	2 929E + (
7.68367E − 06	9 780E + 03	6.70487E − 06	9.292E + 03	3.71389E − 06	1 098E + (
2 15801E − 05	3 693E + 04	1 88968E − 05	3 519E + 04	1.03945E − 05	4 116E + (
5 71082E − 05	1 394E + 05	5 02536E − 05	1 333E + 05	2.70460E − 05	1.543E + (
1.40477E − 04	5.265E + 05	1.24064E − 04	5 047E + 05	6.63716E − 05	5.784E + (
3 21795E − 04	1 988E + 06	2.85596E − 04	1.911E + 06	1 49243E − 04	2 168E + 0
6.78933E − 04	7.507E + 06	6 06957E − 04	7.238E + 06	3 10676E − 04	8.129E + 0
1.28251E − 03	2 835E + 07	1 14719E − 03	2 741E + 07	5 88968E − 04	3 047E + 0
2 30214E − 03	1.070E + 08	2.06531E − 03	1.038E + 08	1 04251E − 03	1.142E + 0
3.88311E − 03	4.041E + 08	3.49272E − 03	3.931E + 08	1 75488E − 03	4.282E + 0·
6 10597E − 03	1.526E + 09	5.50294E − 03	1 489E + 09	2.75858E − 03	1.605E + 0!
9.57620E − 03	5.762E + 09	8.64390E − 03	5 638E + 09	4.33485E − 03	6 017E + 0!
1 44965E − 02	2 176E + 10	1.31203E − 02	2 135E + 10	6 54368E − 03	2.256E + 1(
2.12980E − 02	8 215E + 10	1 92967E − 02	8 086E + 10	9 63627E − 03	8 456E + 1(
2.81867E − 02	3.102E + 11	2.56295E − 02	3 062E + 11	1.27252E − 02	3.170E + 11
3.38868E − 02	1.171E + 12	3.08582E − 02	1.160E + 12	1 53170E − 02	1 188E + 12
3 78217E − 02	4.423E + 12	3.44667E − 02	4.392E + 12	1.71185E − 02	4.454E + 12
4.49199E − 02	1.670E + 13	4 09600E − 02	1 663E + 13	2.03358E − 02	1.670E + 13
5 92713E − 02	6.306E + 13	5.41059E − 02	6.299E + 13	2 71825E − 02	6.259E + 13
1 06539E − 01	2.400E + 14	9.76166E − 02	2.400E + 14	4.93717E − 02	2.400E + 14

Table 5. Crustal density profiles Walecka

| $M = 1330\,M_\odot$ | | $M = 1400\,M_\odot$ | | $M = 1658\,M_\odot$ | |
| $R = 12.252$ (km) | | $R = 12\,280$ (km) | | $R = 11.216$ (km) | |
$(1 - r/R)$	ρ (g cm^{-3})	$(1 - r/R)$	ρ (g cm^{-3})	$(1 - r/R)$	ρ (g cm^{-3})
$0.00000E+00$	$7\,861E+00$	$0\,00000E+00$	$7\,863E+00$	$0\,00000E+00$	$7.873E+00$
$1\,23191E-09$	$1\,285E+01$	$8.38888E-10$	$1\,236E+01$	$8.18035E-12$	$8\,104E+00$
$3.16611E-08$	$4.842E+01$	$2.80625E-08$	$4\,672E+01$	$5.39587E-09$	$3.119E+01$
$1.86840E-07$	$1\,825E+02$	$1.66453E-07$	$1\,766E+02$	$3\,34822E-08$	$1.200E+02$
$9.00051E-07$	$6.877E+02$	$8\,10853E-07$	$6\,679E+02$	$1\,81747E-07$	$4\,621E+02$
$3\,16390E-06$	$2\,592E+03$	$2\,87465E-06$	$2\,525E+03$	$7\,10899E-07$	$1\,778E+03$
$9.32544E-06$	$9\,767E+03$	$8\,51191E-06$	$9.546E+03$	$2\,18496E-06$	$6\,845E+03$
$2\,61696E-05$	$3.681E+04$	$2.39565E-05$	$3\,609E+04$	$6\,34256E-06$	$2.635E+04$
$6\,91322E-05$	$1.387E+05$	$6.35046E-05$	$1.364E+05$	$1\,71650E-05$	$1\,014E+05$
$1\,70007E-04$	$5.228E+05$	$1\,56575E-04$	$5\,158E+05$	$4\,38472E-05$	$3.903E+05$
$3.88916E-04$	$1\,970E+06$	$3.59261E-04$	$1\,950E+06$	$1\,03477E-04$	$1.502E+06$
$8.20653E-04$	$7\,426E+06$	$7.60393E-04$	$7\,373E+06$	$2\,27039E-04$	$5.782E+06$
$1.54960E-03$	$2.799E+07$	$1.43749E-03$	$2\,788E+07$	$4.36443E-04$	$2.225E+07$
$2\,77895E-03$	$1\,055E+08$	$2\,58236E-03$	$1.054E+08$	$7\,97867E-04$	$8.565E+07$
$4.68399E-03$	$3.975E+08$	$4.35895E-03$	$3\,984E+08$	$1\,36479E-03$	$3.297E+08$
$7.30487E-03$	$1.498E+09$	$6.83400E-03$	$1\,506E+09$	$2\,19964E-03$	$1.269E+09$
$1.15413E-02$	$5.646E+09$	$1\,07640E-02$	$5\,695E+09$	$3.46460E-03$	$4.884E+09$
$1.74576E-02$	$2.128E+10$	$1\,62969E-02$	$2.153E+10$	$5\,32332E-03$	$1.880E+10$
$2.55827E-02$	$8\,019E+10$	$2\,39257E-02$	$8\,140E+10$	$7\,89448E-03$	$7.235E+10$
$3.44452E-02$	$3\,022E+11$	$3\,21742E-02$	$3\,078E+11$	$1\,09013E-02$	$2.785E+11$
$4.11286E-02$	$1\,139E+12$	$3\,84200E-02$	$1\,164E+12$	$1.31475E-02$	$1.072E+12$
$4.58221E-02$	$4\,292E+12$	$4.28220E-02$	$4.399E+12$	$1\,47359E-02$	$4.125E+12$
$5.41156E-02$	$1\,618E+13$	$5.07298E-02$	$1.663E+13$	$1\,74490E-02$	$1.588E+13$
$7\,09277E-02$	$6\,097E+13$	$6.67522E-02$	$6\,287E+13$	$2\,33665E-02$	$6.111E+13$
$1.17734E-01$	$2.400E+14$	$1.12973E-01$	$2\,400E+14$	$4.03436E-02$	$2.400E+14$

gravitational mass, namely, $1.33\,M_\odot$, $1\,4\,M_\odot$ and the maximum stable mass. A look at Table 1 shows that, for the EOS models considered here, the maximum neutron star mass (M) and their corresponding radii (R) lie in the range $(1\,414$–$2\,593)\,M_\odot$, and $(7.082$–$14.096)$ km respectively, with the lower value of each of the quantities corresponding to the Pandharipande hyperonic matter EOS (a very soft one) and the higher

B Datta et al.

to the EOS due to Sahu, Basu & Datta (a very stiff EOS). The values of the
thickness (Δ) for maximum mass configurations lie in the range (0 294–0 975
Clearly, the crust thickness, and therefore the crustal density profile, depend sensit
on the EOS model chosen to describe neutron star matter Of the three 1
configurations listed in Table 1, the 1 4 $M_\odot$ neutron star models are of partic
interest because analysis of available binary pulsar data suggests the pulsar mass

Table 6. Crustal density profiles. Friedman-Pandharipande (neutrons)

| $M = 1.330\,M_\odot$ | | $M = 1.400\,M_\odot$ | | $M = 1.658\,M_\odot$ | |
| $R = 10\,824$ (km) | | $R = 10\,701$ (km) | | $R = 9.028$ (km) | |
$(1 - r/R)$	ρ (g cm^{-3})	$(1 - r/R)$	ρ (g cm^{-3})	$(1 - r/R)$	ρ (g cm$^-$
$0.00000E + 00$	$7\,860E + 00$	$0\,00000E + 00$	$7.863E + 00$	$0\,00000E + 00$	$7\,861E +$
$8\,52656E - 10$	$1\,255E + 01$	$1\,37922E - 09$	$1\,350E + 01$	$1\,29813E - 09$	$1\,673E +$
$2.55103E - 08$	$4.744E + 01$	$2.53386E - 08$	$5.086E + 01$	$1.12913E - 08$	$6\,237E +$
$1.51130E - 07$	$1.793E + 02$	$1\,49079E - 07$	$1\,915E + 02$	$6\,47614E - 08$	$2\,325E +$
$7.33104E - 07$	$6\,773E + 02$	$7.08975E - 07$	$7.213E + 02$	$2.89898E - 07$	$8\,667E +$
$2.58950E - 06$	$2\,559E + 03$	$2.46504E - 06$	$2\,716E + 03$	$9.72901E - 07$	$3\,231E + ($
$7.65971E - 06$	$9\,671E + 03$	$7\,24485E - 06$	$1.023E + 04$	$2\,78838E - 06$	$1\,204E + ($
$2\,15325E - 05$	$3\,654E + 04$	$2.02704E - 05$	$3.852E + 04$	$7\,74926E - 06$	$4.490E + ($
$5\,70408E - 05$	$1\,381E + 05$	$5\,34425E - 05$	$1.451E + 05$	$1\,99766E - 05$	$1.674E + 0$
$1.40445E - 04$	$5.217E + 05$	$1\,30935E - 04$	$5\,463E + 05$	$4.87008E - 05$	$6.239E + 0$
$3\,22040E - 04$	$1.971E + 06$	$2\,98868E - 04$	$2\,057E + 06$	$1\,09401E - 04$	$2.326E + 0$
$6\,80500E - 04$	$7\,449E + 06$	$6\,26729E - 04$	$7.748E + 06$	$2.23341E - 04$	$8.670E + 0($
$1\,28579E - 03$	$2\,815E + 07$	$1\,18248E - 03$	$2.918E + 07$	$4.22660E - 04$	$3.232E + 0$
$2\,30933E - 03$	$1.064E + 08$	$2.11855E - 03$	$1\,099E + 08$	$7.50797E - 04$	$1\,205E + 0\varepsilon$
$3\,89716E - 03$	$4.019E + 08$	$3.56727E - 03$	$4\,138E + 08$	$1\,24788E - 03$	$4\,491E + 08$
$6\,13009E - 03$	$1\,519E + 09$	$5.60437E - 03$	$1.558E + 09$	$1\,95988E - 03$	$1.674E + 09$
$9.61827E - 03$	$5\,738E + 09$	$8\,77043E - 03$	$5.869E + 09$	$3\,06589E - 03$	$6\,241E + 09$
$1\,45658E - 02$	$2.168E + 10$	$1.32620E - 02$	$2.210E + 10$	$4.61747E - 03$	$2.326E + 10$
$2.14052E - 02$	$8\,193E + 10$	$1.94955E - 02$	$8.324E + 10$	$6\,80311E - 03$	$8\,673E + 10$
$2\,87813E - 02$	$3\,096E + 11$	$2\,61564E - 02$	$3.135E + 11$	$9\,09191E - 03$	$3.233E + 11$
$3.43830E - 02$	$1\,170E + 12$	$3.12389E - 02$	$1.180E + 12$	$1.08689E - 02$	$1.205E + 12$
$3.83380E - 02$	$4\,420E + 12$	$3.48329E - 02$	$4.446E + 12$	$1\,21344E - 02$	$4\,492E + 12$
$4.54710E - 02$	$1.670E + 13$	$4\,13380E - 02$	$1\,674E + 13$	$1.43877E - 02$	$1\,675E + 13$
$5\,99013E - 02$	$6\,311E + 13$	$5\,44597E - 02$	$6\,305E + 13$	$1.92192E - 02$	$6\,243E + 13$
$1.04735E - 01$	$2.400E + 14$	$9\,55692E - 02$	$2\,400E + 14$	$3.40162E - 02$	$2\,400E + 14$

Table 7. Crustal density profiles Wiringa *et al* (UV14 + UVII).

$M = 1.330\ M_\odot$		$M = 1\ 400\ M_\odot$		$M = 1.658\ M_\odot$	
$R = 11.122$ (km)		$R = 11.115$ (km)		$R = 9\ 800$ (km)	
$(1 - r/R)$	ρ (g cm^{-3})	$(1 - r/R)$	ρ (g cm^{-3})	$(1 - r/R)$	ρ (g cm^{-3})
$0.00000E + 00$	$7\ 865E + 00$	$0\ 00000E + 00$	$7.863E + 00$	$0\ 00000E + 00$	$7\ 862E + 00$
$4\ 79318E - 10$	$9\ 545E + 00$	$3.12246E - 11$	$8.123E + 00$	$1\ 33983E - 09$	$1\ 684E + 01$
$1\ 84269E - 08$	$3\ 649E + 01$	$1.35178E - 08$	$3.127E + 01$	$1\ 10568E - 08$	$6.274E + 01$
$1\ 14890E - 07$	$1\ 395E + 02$	$8.71834E - 08$	$1.204E + 02$	$6\ 25945E - 08$	$2\ 338E + 02$
$5\ 88007E - 07$	$5.332E + 02$	$4.62922E - 07$	$4.636E + 02$	$2.78294E - 07$	$8\ 710E + 02$
$2\ 21576E - 06$	$2.038E + 03$	$1.81126E - 06$	$1\ 785E + 03$	$9\ 35252E - 07$	$3\ 246E + 03$
$5\ 74056E - 06$	$7.792E + 03$	$5\ 62199E - 06$	$6\ 872E + 03$	$2.67672E - 06$	$1\ 209E + 04$
$1\ 92271E - 05$	$2.979E + 04$	$1.61628E - 05$	$2\ 646E + 04$	$7.43546E - 06$	$4.506E + 04$
$5\ 19015E - 05$	$1.139E + 05$	$4.41569E - 05$	$1\ 019E + 05$	$1.91534E - 05$	$1\ 679E + 05$
$1\ 29966E - 04$	$4\ 353E + 05$	$1.11643E - 04$	$3\ 922E + 05$	$4\ 66804E - 05$	$6.256E + 05$
$3\ 03771E - 04$	$1\ 664E + 06$	$2.64122E - 04$	$1\ 510E + 06$	$1\ 04872E - 04$	$2.331E + 06$
$7\ 60309E - 04$	$6.361E + 06$	$5.82289E - 04$	$5\ 813E + 06$	$2.13857E - 04$	$8.686E + 06$
$1\ 25384E - 03$	$2\ 432E + 07$	$1.11103E - 03$	$2\ 238E + 07$	$4\ 04672E - 04$	$3.236E + 07$
$2\ 27729E - 03$	$9\ 295E + 07$	$2.03311E - 03$	$8.617E + 07$	$7\ 18723E - 04$	$1\ 206E + 08$
$3\ 88460E - 03$	$3\ 553E + 08$	$3.49593E - 03$	$3.318E + 08$	$1\ 20173E - 03$	$4\ 493E + 08$
$6\ 17831E - 03$	$1\ 358E + 09$	$5.61392E - 03$	$1.277E + 09$	$1\ 87529E - 03$	$1.674E + 09$
$9\ 70251E - 03$	$5.193E + 09$	$8.77612E - 03$	$4.918E + 09$	$2.93350E - 03$	$6\ 238E + 09$
$1\ 48127E - 02$	$1\ 985E + 10$	$1.34625E - 02$	$1.893E + 10$	$4.41814E - 03$	$2\ 324E + 10$
$2\ 18186E - 02$	$7.588E + 10$	$1.99008E - 02$	$7.290E + 10$	$6.50913E - 03$	$8\ 661E + 10$
$2\ 97300E - 02$	$2.901E + 11$	$2\ 73359E - 02$	$2\ 807E + 11$	$8\ 70128E - 03$	$3.227E + 11$
$3\ 56409E - 02$	$1.109E + 12$	$3.28536E - 02$	$1.081E + 12$	$1\ 04031E - 02$	$1.203E + 12$
$3\ 97973E - 02$	$4\ 239E + 12$	$3\ 67344E - 02$	$4\ 160E + 12$	$1\ 16147E - 02$	$4\ 481E + 12$
$4\ 71200E - 02$	$1\ 620E + 13$	$4.35051E - 02$	$1.602E + 13$	$1.37662E - 02$	$1\ 670E + 13$
$5\ 18097E - 02$	$6\ 195E + 13$	$5\ 71556E - 02$	$6\ 167E + 13$	$1.83039E - 02$	$6.221E + 13$
$6\ 00741E - 01$	$2\ 400E + 14$	$9.34953E - 02$	$2.400E + 14$	$2\ 99743E - 02$	$2.400E + 14$

:se binaries to be close to this value For the $1\ 4\ M_\odot$ models, the Δ is in the range 361–$2\ 970)$ km, a much wider range than for the maximum mass cases. In Tables 2–9, give the crustal density variation with the depth in normalized units with respect to radius $(1 - r/R)$, (where r is the radial distance from the centre of the star) from the face of the neutron star for the three mass configurations. These tables will be of ect application in calculations of magnetic field evolution of pulsars. The same thing,

namely, the crustal density variations, is graphically illustrated in Figs 2 and 1 4 $M_\odot$ configurations for the various EOS models The dashed lines in these fig represent the core-inner crust boundary (which corresponds to $r = R - \Delta$) and dot-cum-dashed lines represent the surface of the neutron star $(r = R)$ The variati sharpest for the softest EOS considered here (Pandharipande hyperonic matter) gets to be comparatively less sharp as the EOS gets to be more stiff. The dependence

Table 8. Crustal density profiles: Prakash, Ainsworth & Lattimer Model 1

$M = 1\ 330\ M_\odot$ $R = 11.384$ (km)		$M = 1.400\ M_\odot$ $R = 10\ 987$ (km)		$M = 1.658\ M_\odot$ $R = 9\ 483$ (km)	
$(1 - r/R)$	ρ (g cm^{-3})	$(1 - r/R)$	ρ (g cm^{-3})	$(1 - r/R)$	ρ (g cm^{-}
$0.00000E + 00$	$7\ 864E + 00$	$0\ 00000E + 00$	$7.861E + 00$	$0\ 00000E + 00$	$7.868E$
$1.23204E - 09$	$1\ 299E + 01$	$5.64384E - 10$	$1.202E + 01$	$7\ 20466E - 10$	$1\ 297E$
$2.87558E - 08$	$4\ 893E + 01$	$2\ 26968E - 08$	$4.539E + 01$	$1\ 70600E - 08$	$4\ 893E\ \cdot$
$1\ 69510E - 07$	$1\ 843E + 02$	$1.34550E - 07$	$1\ 714E + 02$	$1.00739E - 07$	$1\ 846E\ \cdot$
$8\ 13995E - 07$	$6\ 945E + 02$	$6\ 59261E - 07$	$6.476E + 02$	$4.84015E - 07$	$6\ 966E\ \cdot$
$2\ 85212E - 06$	$2\ 616E + 03$	$2.34711E - 06$	$2\ 446E + 03$	$1.70821E - 06$	$2\ 628E\ \cdot$
$8.40799E - 06$	$9.857E + 03$	$6.97231E - 06$	$9.238E + 03$	$5.00958E - 06$	$9\ 917E\ \cdot$
$2.35563E - 05$	$3.713E + 04$	$1.95999E - 05$	$3.489E + 04$	$1\ 41327E - 05$	$3.742E\ \cdot$
$6.22494E - 05$	$1.399E + 05$	$5.20863E - 05$	$1.318E + 05$	$3.71474E - 05$	$1.412E\ \dashv$
$1\ 52771E - 04$	$5\ 270E + 05$	$1\ 28304E - 04$	$4.978E + 05$	$9.18752E - 05$	$5\ 327E\ \dashv$
$3\ 49639E - 04$	$1\ 986E + 06$	$2.95396E - 04$	$1.880E + 06$	$2.08710E - 04$	$2.010E\ \dashv$
$7.37203E - 04$	$7.480E + 06$	$6\ 28698E - 04$	$7.102E + 06$	$4.40124E - 04$	$7\ 585E\ \dashv$
$1\ 39012E - 03$	$2\ 818E + 07$	$1\ 18548E - 03$	$2\ 683E + 07$	$8.35840E - 04$	$2\ 862E +$
$2\ 49418E - 03$	$1\ 062E + 08$	$2.13488E - 03$	$1.013E + 08$	$1.48947E - 03$	$1\ 080E +$
$4\ 20487E - 03$	$4\ 000E + 08$	$3.61133E - 03$	$3\ 827E + 08$	$2.51514E - 03$	$4\ 074E +$
$6\ 60710E - 03$	$1\ 507E + 09$	$5\ 69228E - 03$	$1\ 446E + 09$	$3\ 95905E - 03$	$1.537E +$
$1.04093E - 02$	$5\ 677E + 09$	$8\ 98241E - 03$	$5\ 460E + 09$	$6.24693E - 03$	$5\ 801E +$
$1.56800E - 02$	$2\ 139E + 10$	$1\ 35685E - 02$	$2\ 062E + 10$	$9\ 43094E - 03$	$2\ 189E +$
$2.29656E - 02$	$8.057E + 10$	$1\ 99082E - 02$	$7.790E + 10$	$1.38631E - 02$	$8.258E +$
$3\ 27849E - 02$	$3.036E + 11$	$2\ 85376E - 02$	$2.942E + 11$	$1.98362E - 02$	$3.116E +$
$3.71907E - 02$	$1.144E + 12$	$3.26160E - 02$	$1.111E + 12$	$2.24955E - 02$	$1\ 176E +$
$4\ 15513E - 02$	$4.308E + 12$	$3.63684E - 02$	$4.198E + 12$	$2\ 51423E - 02$	$4.436E +$
$4\ 96169E - 02$	$1\ 623E + 13$	$4\ 34154E - 02$	$1.586E + 13$	$3.01974E - 02$	$1\ 674E +$
$6\ 63662E - 02$	$6\ 115E + 13$	$5\ 79696E - 02$	$5\ 989E + 13$	$4.11830E - 02$	$6.316E +$
$1.49536E - 01$	$2.400E + 14$	$1.32527E - 01$	$2.400E + 14$	$9.50182E - 02$	$2.400E +$

Table 9. Crustal density profiles. Sahu, Basu & Datta

$M = 1\,330\ M_\odot$ $R = 14.685$ (km)		$M = 1\,400\ M_\odot$ $R = 14.761$ (km)		$M = 1\,658\ M_\odot$ $R = 14.096$ (km)	
$(1 - r/R)$	ρ (g cm^{-3})	$(1 - r/R)$	ρ (g cm^{-3})	$(1 - r/R)$	ρ (g cm^{-3})
$0\ 00000E+00$	$7\ 861E+00$	$0\ 00000E+00$	$7\ 861E+00$	$0\ 00000E+00$	$7.863E+00$
$1\ 68177E-10$	$8\ 839E+00$	$6\ 18207E-10$	$1\ 139E+01$	$1\ 28531E-09$	$1.483E+01$
$2.51686E-08$	$3\ 391E+01$	$3\ 29844E-08$	$4\ 323E+01$	$1\ 50712E-08$	$5.553E+01$
$1.54202E-07$	$1\ 301E+02$	$1.96946E-07$	$1\ 640E+02$	$8.76310E-08$	$2.080E+02$
$8\ 19531E-07$	$4.990E+02$	$9\ 80469E-07$	$6\ 220E+02$	$4\ 05511E-07$	$7\ 789E+02$
$3.13725E-06$	$1\ 914E+03$	$3\ 54032E-06$	$2.360E+03$	$1\ 39181E-06$	$2\ 917E+03$
$9.61781E-06$	$7\ 344E+03$	$1.05575E-05$	$8\ 951E+03$	$4\ 02961E-06$	$1\ 092E+04$
$2\ 75907E-05$	$2\ 817E+04$	$2.98693E-05$	$3\ 396E+04$	$1\ 12695E-05$	$4\ 091E+04$
$7\ 48055E-05$	$1\ 081E+05$	$7\ 95623E-05$	$1\ 288E+05$	$2\ 93190E-05$	$1.532E+05$
$1.88519E-04$	$4.146E+05$	$1\ 97315E-04$	$4.886E+05$	$7.19116E-05$	$5\ 737E+05$
$4\ 42469E-04$	$1\ 591E+06$	$4.54910E-04$	$1.854E+06$	$1.61745E-04$	$2.149E+06$
$9\ 61559E-04$	$6.102E+06$	$9.64816E-04$	$7.032E+06$	$3.36900E-04$	$8\ 046E+06$
$1\ 84383E-03$	$2\ 341E+07$	$1.83881E-03$	$2\ 667E+07$	$6.38253E-04$	$3\ 013E+07$
$3\ 35559E-03$	$8\ 979E+07$	$3.31124E-03$	$1\ 012E+08$	$1.13022E-03$	$1.128E+08$
$5\ 73697E-03$	$3.445E+08$	$5.60155E-03$	$3\ 839E+08$	$1.90195E-03$	$4.226E+08$
$9\ 15009E-03$	$1.321E+09$	$8.77845E-03$	$1.456E+09$	$2\ 98755E-03$	$1.583E+09$
$1\ 43445E-02$	$5.069E+09$	$1.38724E-02$	$5\ 524E+09$	$4\ 69758E-03$	$5.927E+09$
$2.18743E-02$	$1\ 945E+10$	$2.10140E-02$	$2\ 095E+10$	$7.09328E-03$	$2\ 220E+10$
$3\ 21388E-02$	$7\ 460E+10$	$3.07877E-02$	$7\ 949E+10$	$1.04322E-02$	$8.313E+10$
$4.41761E-02$	$2\ 862E+11$	$4.18584E-02$	$3.015E+11$	$1\ 41597E-02$	$3\ 113E+11$
$5\ 25674E-02$	$1\ 098E+12$	$4\ 96901E-02$	$1.144E+12$	$1.68582E-02$	$1.166E+12$
$5\ 85730E-02$	$4.212E+12$	$5.53066E-02$	$4.339E+12$	$1.88106E-02$	$4.366E+12$
$6.90648E-02$	$1\ 616E+13$	$6.52886E-02$	$1\ 646E+13$	$2\ 22586E-02$	$1.635E+13$
$7\ 05533E-02$	$6\ 198E+13$	$8.55960E-02$	$6.245E+13$	$2\ 95893E-02$	$6.123E+13$
$2.13000E-01$	$2.400E+14$	$2\ 01202E-01$	$2.400E+14$	$6.91727E-02$	$2.400E+14$

eutron star mass of the radius and of the crustal thickness respectively are illustrated ι Figs 4 and 5 From Fig. 4, it can be seen that for the EOS models Walecka (1974), ιd Sahu, Basu & Datta (1993), ι.e. curves D and H, the slope for the lower values of the able mass is noticeably positive. This is because of the substantial contribution of tractive force brought on by the scalar σ-meson interaction present ιn these equations `state. It may be mentioned here that the σ-ιnteraction plays an ιmportant role at
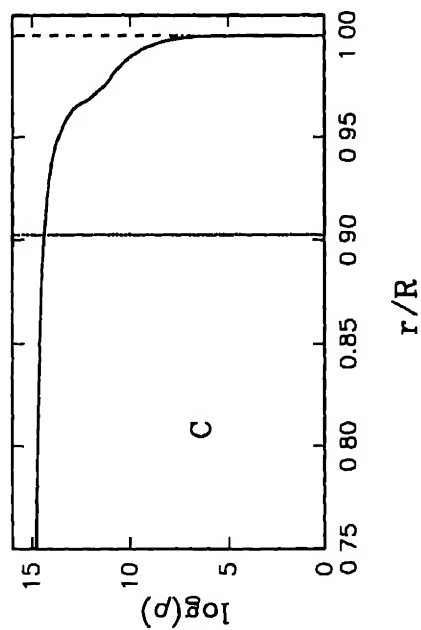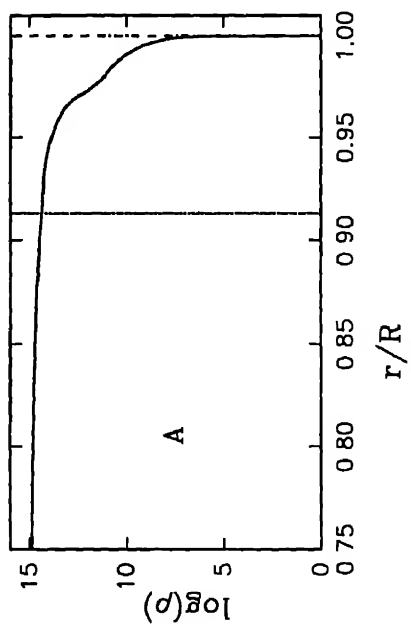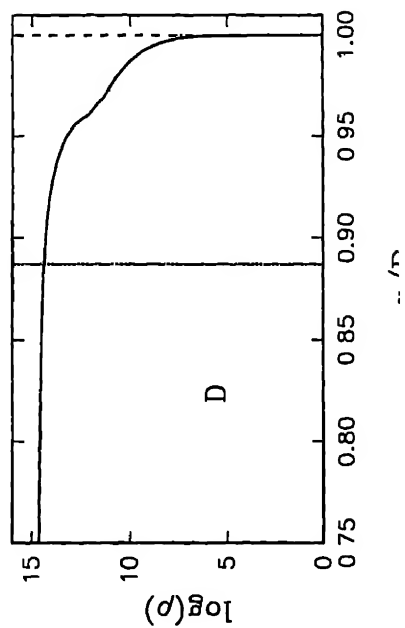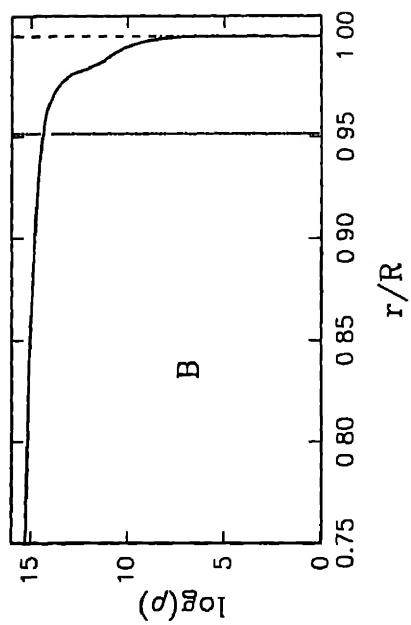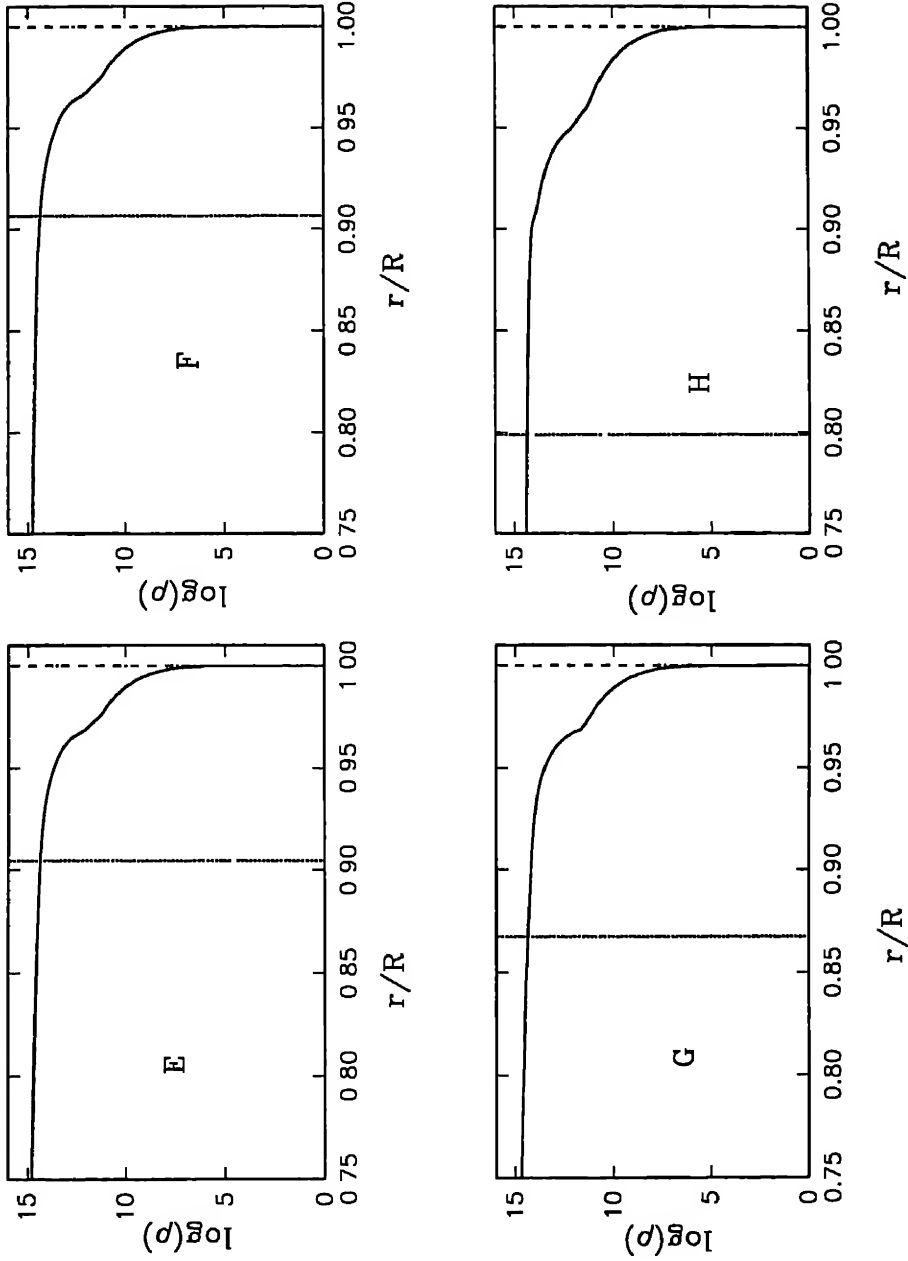
Figure 3. Neutron star density profiles for $1.4\,M_\odot$. EOS models (E–H)
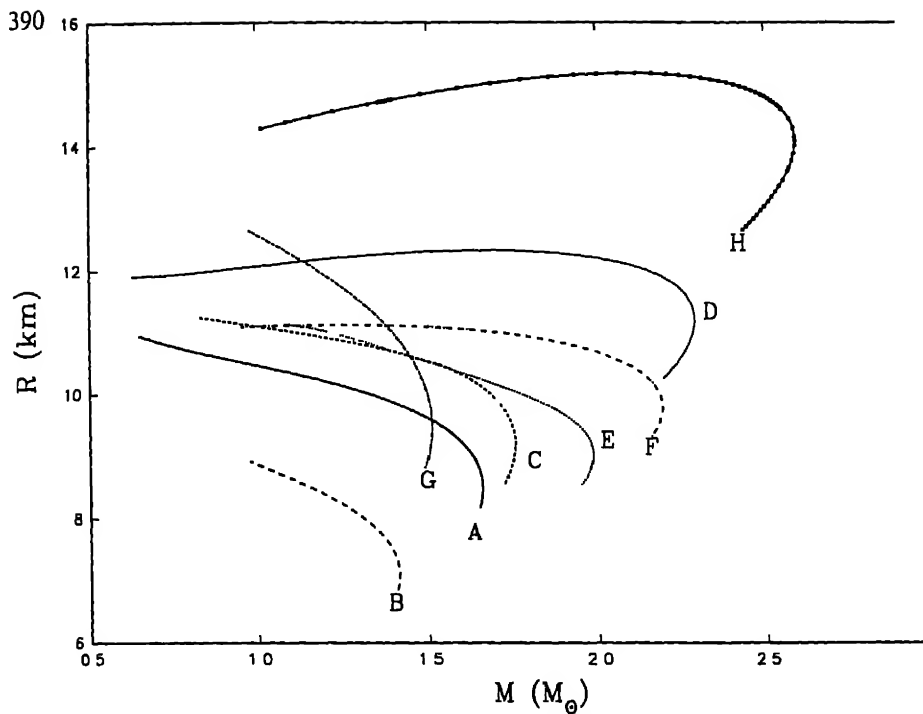
Figure 4. Neutron star mass-radius dependences for the EOS models (A–H)
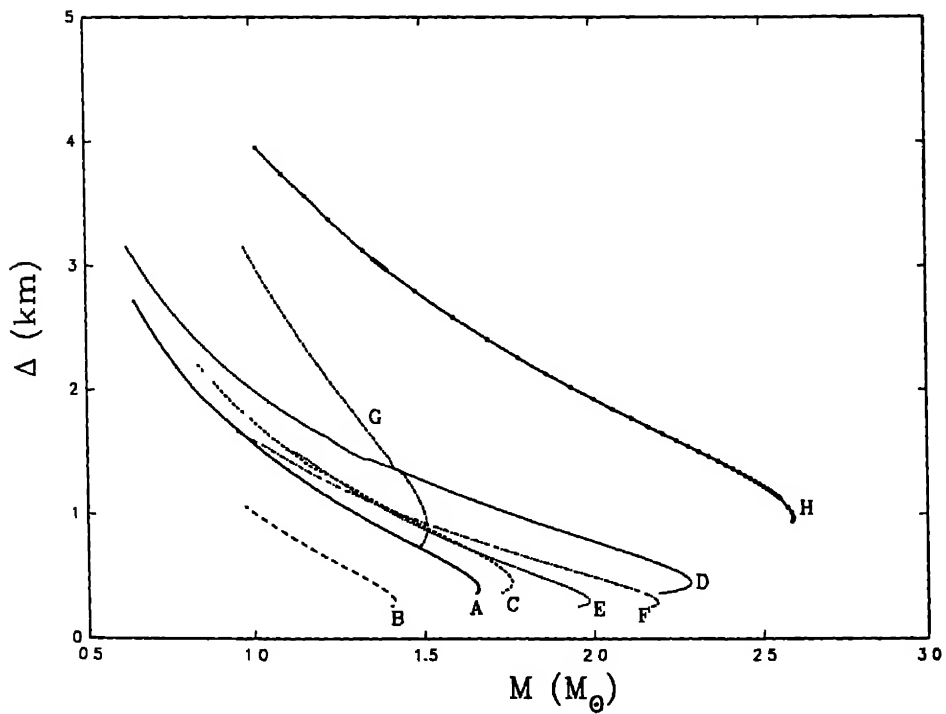
Figure 5. Neutron star crustal thickness (Δ) as a function of the gravitational mass (M) for the EOS models (A–H)

intermediate densities providing nuclear saturation, and must be included in any field theoretical EOS model At high densities the contribution of the vector meson (ω) interaction, which provides repulsive force dominates, and the slope becomes negative. The crustal thickness (Δ) is decided by how much mass is contained in the core and interior regions of the neutron star, so that, in general, the more the mass of the neutron star, the less the value of Δ for any EOS

As already emphasized, the crustal density profile of neutron stars is a key input in the proper understanding of a variety of important features associated with pulsars, such as the cooling rate Another important application, that is of much current interest in astrophysics, relates to the evolution of magnetic fields of pulsars However, several calculations reported in the literature on the problem of magnetic field evolution have considered cooling models for a specific EOS model while using the crustal model that corresponds to a different EOS model This is mainly because of non-availability of detailed, numerical crustal density profiles. The survey presented here is a preliminary step towards a uniform and consistent investigation of the problem of evolution of neutron star magnetic fields, which will be reported in a forthcoming paper (Bhattacharya & Datta 1995).

Acknowledgement

References

Ambartsumyan, V A , Saakyan, G S 1960, *Soviet Astr* , **4**, 187.
Antia, H M. 1991, *Numerical Methods for Scientists & Engineers* (New Delhi. Tata McGraw Hill Publ) 895.
Arnett, W D , Bowers, R L 1977, *Astrophys J Suppl* , **33**, 415
Baym, G , Pethick, C J , Sutherland, P G 1971, *Astrophys J.*, **170**, 299
Bethe, H. A , Johnson, M B 1974, *Nucl. Phys* , **A230**, 1
Bhattacharya, D , Datta, B. 1995, preprint
Datta, B 1988, *Fund. Cosmic Phys* , **12**, 151
Feynman, R P., Metropolis, N , Teller, E. 1949, *Phys. Rev* , **75**, 1561
Friedman, B., Pandharipande, V R 1981, *Nucl Phys.*, **A361**, 502
Jastrow, R 1955, *Phys Rev.*, **98**, 1479
Moller, P , Myers, W D., Swiatecki, M J., Treiner, J 1988, *Atomic Data Nucl Data Tables* **39**, 225.
Negele, J. W., Vautherin, D. 1973, *Nucl Phys.*, **A207**, 298
Oppenheimer, J. R., Volkoff, G M 1939, *Phys Rev* , **55**, 374.
Pandharipande, V R. 1971a, *Nucl Phys.*, **A174**, 641
Pandharipande, V R 1971b, *Nucl Phys* , **A178**, 123
Prakash, M., Ainsworth, T L., Lattimer, J M. 1988, *Phys Rev Lett* , **61**, 2518
Reid, R. V., Jr 1968, *Ann. Phys* , **50**, 411.
Sahu, P. K , Basu, R., Datta, B. 1993, *Astrophys. J.*, **416**, 267.
Walecka, J D 1974, *Ann Phys.*, **83**, 491.
Wiringa, R B , Fiks, V., Fabrocini, A, 1988, *Phys. Rev C*, **38**, 1010.

Flux Monitoring at 327 MHz during SL9-Jupiter Collision

Rakesh K. Malik*, Pradeep Gothoskar*, P. K. Manohran[@],
G. Swarup*, K. Subramanian* & V. Balasubramanian[@]
**National Centre for Radio Astrophysics, TIFR, Post Box 3, Pune 411 007*
[@] *Radio Astronomy Centre, TIFR, Ooty 643 001*

Abstract. Jupiter flux at 327 MHz was monitored using the Ooty radio telescope from July 12th to July 29th during the collision of comet Shoemaker-Levi 9 with Jupiter Flux was found to increase steadily from July 17th to July 26th by ~ 2.5 Jy, after which it declined to its pre-event value The comparison of 327 MHz observations with those at 840 MHz and 2240 MHz indicates that the enhancement was mainly due to the increased synchrotron emission and the contribution of thermal emission was very small at metric-decimetric frequencies The enhancement in radio emission was found to be more at 840 MHz than at 327 or 2240 MHz. The steepening of the spectrum between 327 and 840 MHz as well as between 2240 and 840 MHz was also noted

Key words SL9-Jupiter collision—radio flux monitoring—Jupiter radio emission

1. Introduction

Radio emission from Jupiter spans a wide frequency range from 0 01 MHz to 300 GHz This radio spectrum consists of three distinct components. Thermal radiation from the cloud layer dominates at millimeter and centimeter wavelengths At metric-decimetric wavelengths, the dominant component is the synchrotron emission by relativistic electrons trapped in the Jupiter's magnetic field. At the low frequency end, below 40 MHz, the emission consists of sporadic bursts due to plasma instabilities in the inner magnetosphere that generate the emission at frequencies slightly above the local electron cyclotron frequency

In the metric-decimetric band of interest to us, the emission is due to synchrotron process powered by electrons accelerated to 10–100s of MeV by radial diffusion from the outer magnetosphere into $\sim 2\,R_J$ These high energy electrons are then trapped in a shell of $\sim 2\,R_J$ above the cloud top level and centered on the magnetic equator which is tilted by about 10° with respect to the spin equator. The mirror points of most of these trapped electrons are within $\sim 1\,R_J$ above and below the magnetic equatorial plane. The observed synchrotron source therefore is the projection of a toroidal source surrounding the planet. The width and height of this projection are approximately $6\,R_J$ and $2\,R_J$ respectively The spectrum in the metric-decimetric band is nearly flat with the peak at around 1000 MHz. At higher frequencies, the thermal component dominates the synchrotron emission as shown in Fig. 1

393
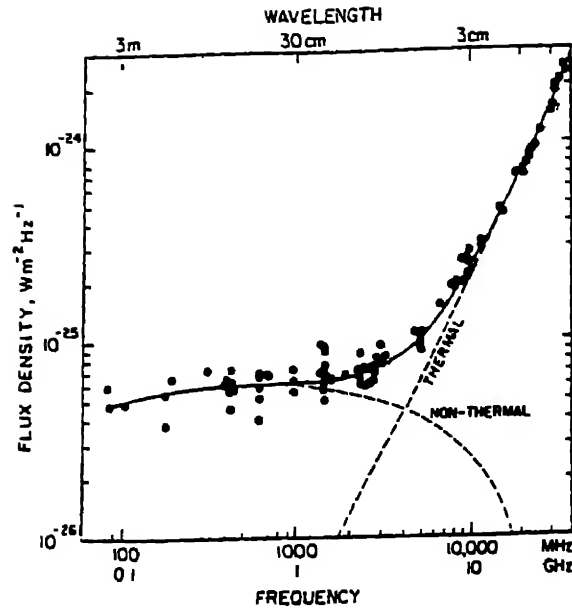
Figure 1. Radio spectrum of Jupiter observed over metric and decimetric frequency bands The observed spectrum (solid line) is composed of emission due to thermal and non-thermal components (dashed lines), (Carr, T D *et al* 1986, *Physics of Jovian Magnetosphere*, pp 235).

The passage of cometary fragments through the Jovian magnetosphere and the subsequent collisions were expected to affect Jupiter's metric-decimetric emission. Various scenarios for the change in the Jovian radio emission were thought of and are mentioned below.

■ It was expected that the energy released in the impact could ionize the cometary material resulting in an enhancement in the electron density These electrons could be accelerated to high energies in the shock waves that would have resulted from the impact. The resulting increase in the number of relativistic electrons would enhance the emission.

■ The emission could also be enhanced, if instead of producing new relativistic electrons in the impact, low energy electrons already existing in the synchrotron radiation belts were accelerated to sufficiently high energies thus resulting in a net enhancement in the density of high energy electrons.

■ Enhanced thermal emission due to the heating up of the Jovian atmosphere by the impacts was also a possibility. Enhancement due to thermal emission was however expected to be seen for short durations after the impact because of short cooling time scales

■ On the other hand, increase in the dust grains and larger-sized material in the magnetosphere with the entry of the comet was expected to slow down the high energy electrons As a result, the intensity was expected to decrease immediately after the cometary material entered the radiation belts Inward diffusion of electrons through a dusty magnetosphere was therefore expected to result in a drop in emission for many months after the comet had entered the magnetosphere (de Pater 1994).

We briefly describe our observational results in section 2 Results are discussed in section 3, and section 4 concludes the paper

2. Observational results

The observations were carried out using the Ooty Radio Telescope (ORT). The ORT consists of a 500 m long cylindrical parabolic antenna with an effective collecting area of about 8000 sq m situated in southern India at a latitude of $+12°$. The telescope operates at 327 MHz The telescope can be steered around its equatorial axis from -4.5 to $+4.5$ hours which allows one to monitor a single source for a stretch of 9 hours. In declination, the telescope can be pointed electronically from $+35$ to $-35°$ by phasing the array of dipoles (Swarup *et al.* 1971). The telescope can be operated
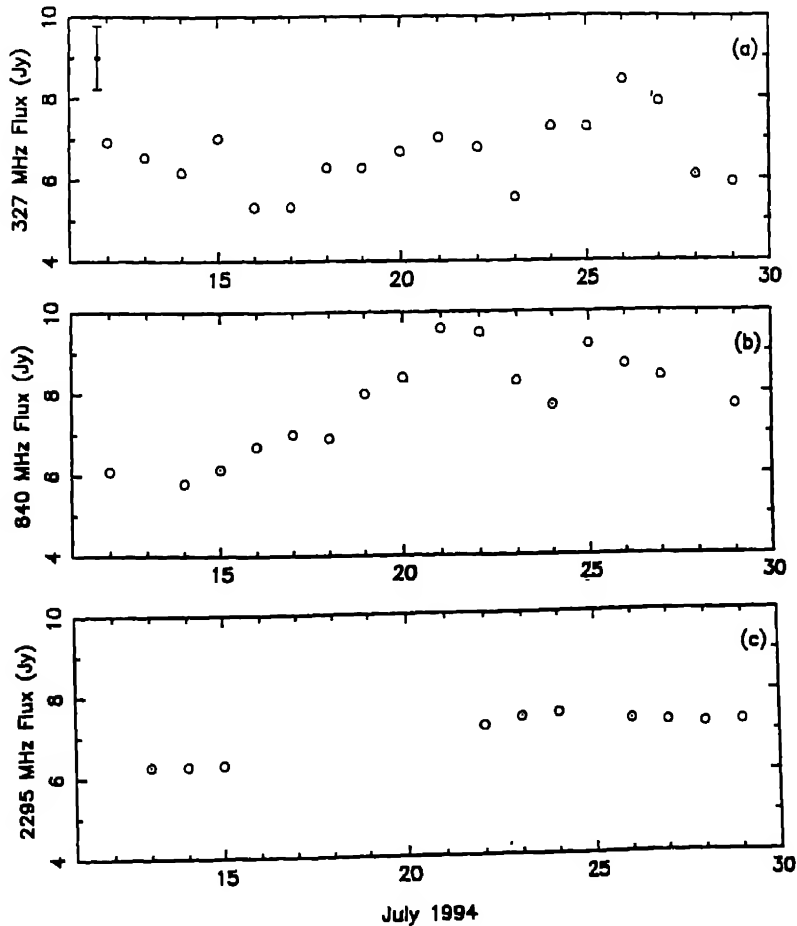
Figure 2. Radio flux measurements carried out between 12th July and 29th July 1994 Measurements at 327 MHz (a) were done using the Ooty radio telescope which we have compared with the reported observations at 840 MHz (b) and 2295 MHz (c) from Molonglo and J P L observatories, respectively All the flux values were normalized to a distance of 4 AU.

either in total power mode, where contribution from all the dipoles is added, or in phase-switched mode, where the signals from the north and south half of the telescope are correlated. In the phase-switched mode the ORT beam is 2 0° in the right ascension and 3' 5 sec(δ) in declination

The observations for the Jupiter-Comet collision were started on July 12th and continued till July 29th, 1994, well after the collision had taken place. Jupiter observations were interspersed with observations of calibrators. A total of five calibration sources were used during the course of these observations, and at least three of them were observed on a given day (except for July 16th and 17th when the number was 2 and 1 respectively). The data found contaminated with interference were rejected. Observations were corrected for the effect of ORT beamshape as Jupiter drifted in the beam For any Jupiter observation, confusion sources in the ORT beam down to 10 milli Jansky (1 Jansky = 10^{-26} Wm^{-2} Hz^{-1}) were subtracted After calibrating it against the calibration sources observed that day, a daily average of the Jupiter flux was obtained. The daily variation of the Jupiter flux thus obtained is shown in Fig 2(a).

As can be seen in Fig 2(a) there was a systematic increase of about 2·5 Jy (after normalizing it to a distance of 4 AU) observed between 17th and 26th July which was greater than the limit of flux measurement for ORT. This is indicated by the vertical error bar in Fig. 2(a) This increase in flux started after the impact of the first cometary fragment The maximum flux was observed on 26th July after which the flux steadily declined over the next 4 days of observations. The data from July 12th to July 16th, when the cometary fragments had entered the Jovian magnetosphere and were approaching Jupiter, show a gradual decrease in flux.

We have compared our results with the observations at 840 MHz (Huntstead & Campbell-Wilson 1994) and 2240 MHz (Klein *et al.* 1994) (Fig 2b–c). The enhanced emission was more at 840 MHz than at the other two frequencies There is evidence of progressive steepening of the radio spectrum between 327 and 840 MHz, and between 840 and 2240 MHz as a result of the impacts. As the radio emission declined after July 22nd (at 840 MHz) the spectra in these two frequency ranges also became less steep.

3. Discussion

The initial decrease in the emission level (July 12th to July 16th) could have resulted from the absorption of high energy synchrotron electrons by the dust added to the atmosphere by the comet For the later enhanced radio emission we now explore two possible explanations – both enhanced thermal as well as non-thermal emission.

3 1 *Thermal emission*

The data show a day-to-day increase in the flux with a peak on July 26th (i.e. 4 days after the last impact). The impacts therefore seemed to have had a cumulative effect on the radio emission rather than just a transitory enhancement at the time of the impact. The optical depth τ for free-free absorption is (e.g. Benz 1993).

$$\tau \sim 0\cdot11\, n_e^2 \nu^{-2} T^{-1\,5} \delta L, \tag{1}$$

where n_e is in number of electrons per cm^3, ν is in Hz, T in degree Kelvin and δL is measured in cm.

In order to explain the enhanced emission at 327 MHz in terms of optically thick thermal emission, an enhanced electron density of the order of $10^8 \, cm^{-3}$ would be required, assuming $T \sim 5000 \, K$ (since there is evidence that the temperature of the plumes resulting from the impact reached several thousand degrees, see Chapman 1994) and $\delta L \sim 1000 \, km$. (Note that we cannot account for the observations by assuming optically thin thermal emission since the increase in flux at 840 MHz is more than that at 327 MHz) However gas with density as high as indicated above, will cool very fast. For example, taking an analogy with HI or HII regions since the dominant component of the Jovian atmosphere is hydrogen, the cooling rate can be roughly estimated by (Spitzer 1978) $\Lambda/n_h^2 \sim 7 \times 10^{-26} \, erg \, cm^3 \, s^{-1}$ (assuming fraction of the H atoms ionized to be 10^{-2}).

The cooling time scale therefore would be $t_c \sim (3/2 n_h k T)/\Lambda$. Taking $n_h \sim 10^{10}$ (for fraction of ionized H atoms $\sim 10^{-2}$) and $T \sim 5000 \, K$, we find that the cooling time would be $\sim 1/2 \, hr$ Even if the cooling time derived above is off by an order of magnitude compared to what may hold for the Jovian atmosphere, we find that it is still difficult to understand the slow and sustained rise in the emission seen at the metric-decimetric band The thermal model however is more plausible for understanding the rapid variation in the emission reported at millimeter wavelengths

Another difficulty with the thermal emission is that the electron density of $\sim 10^8 \, cm^{-3}$ is required across the Jupiter disk in a shell of thickness $\sim 1000 \, km$. This is possible only if ALL the electrons from a typical cometary fragment spread out across the disk, which seems difficult to justify.

We can however use the shape of the frequency spectrum to constrain the thermal contribution to the observed enhanced emission. Assuming the thermal contribution to be optically thick at 2240 MHz, and further assuming that the increase of flux of $\sim 1 \, 56 \, Jy$ at 2240 MHz was purely due to thermal emission, in order to derive an upper limit on the thermal part of the enhanced emission, we find that the thermal contribution at 327 MHz would be $\leqslant 50 \, mJy$ while at 840 MHz it would be smaller than 300 mJy because the thermal emission scales as $1/\lambda^2$ for optically thick emission

3.2 *Synchrotron emission*

The peak of the Jovian synchrotron spectrum is determined by $\nu_{max}(MHz) \sim 4 \cdot 8(E)^2(B) \sin(\alpha)$, where energy and magnetic field is in MeV and Gauss respectively (Carr *et al* 1986). Taking $\nu_{max} \sim 1 \, GHz$, $\sin(\alpha) \sim 1$ and $B \sim 3$ Gauss we find that the energies to which electrons need to be accelerated are $\sim 8 \, MeV$ to explain the enhanced emission. The power emitted by one electron is (Carr *et al.* 1986):

$$p \approx 6 \cdot 10^{-22} \left(\frac{E}{MeV} \right)^2 \left(\frac{B}{Gauss} \right)^2 \sin^2 \alpha \sim 3 \cdot 10^{-19} \, W. \qquad (2)$$

Assuming that the enhanced emission comes from a volume of scale size $\sim 1000 \, km$, we find that an excess electron density of the order of $2 \, 5 \times 10^2 \, cm^{-3}$ accelerated to energies $\sim 10 \, MeV$ is sufficient to explain the enhanced emission.

Considering the moderate increase in the number density, compared to that for thermal emission, of relativistic electrons required to explain it, the synchrotron process seems to be the source of enhanced emission. The requirement of electrons accelerated to relativistic speeds could be met by a variety of processes.

- Shock waves generated by the impact could have accelerated the low energy electrons existing in the inner regions of the Jovian magnetosphere.
- There is an evidence of production of new electrons as inferred from the increase in auroras seen in ultraviolet images obtained by HST soon after the impact Therefore there is also a possibility that these newly generated electrons were accelerated and deposited in the inner regions of the magnetosphere.
- A third possibility would be the reconnection of magnetic field taking place behind the blob of ionized material as it arose after the impact and stretched the field lines.

All three of these scenarios would also explain the inward movement of the synchrotron belts.

4. Conclusion

We have observed the radio emission from Jupiter at the time of collision with comet Shoemaker-Levy at 327 MHz using the Ooty radio telescope. A careful analysis of the data indicates that there was a systematic but marginal increase of ~ 2.5 Jy in the Jovian radio emission at 327 MHz due to the cometary impacts. The flux continued to increase till July 26th after which it declined.

Comparison with observations carried out at 840 MHz and 2240 MHz indicates that the enhanced radio emission from Jupiter due to the cometary impacts was due to synchrotron emission. Acceleration of electrons in the inner regions of the magneto-sphere either due to shock waves emanating as an after effect of the impact or due to magnetic reconnection could be the cause of the increase in emission

Though the thermal emission cannot explain the sustained rise in the radio emission at meter-decimeter wavelengths, it is more plausible for 'bursts' seen at the time of impacts as e.g in millimetric wavelengths.

References

Benz, A O. 1993, *Plasma Astrophysics,* (Dordrecht, Boston, London Kluwer Academic Publishers) pp 263

Carr, T. D., Desch, M D , Alexander, J K. 1986, *Physics of Jovian Magnetosphere,* Cambridge Planetary Science Series, pp 235.

Chapman, C R. 1994, *Nature,* 370, 245

de Pater, I. 1994, *Geophys Res. Lett ,* 21, 1071.

Huntstead, R., Campbell-Wilson, D 1994, (private communication)

Klein, M J , Gulkis, S , Bolton, S J 1994, *Symposium on the Magnetospheres of the Outer Planets* (private communication)

Spitzer, Jr., L. 1978, *Physical Processes in the Interstellar Medium* (New York, Chichester, Brisbane, Toronto Wiley-Interscience Publication) p 143

Swarup, G , Sharma, N V G, Joshi, M. N , Kapahi, V K, Bagri, D. S , Damle, S. M., Ananthakrishnan, S , Balasubramanian, V , Sinha, R P 1971, *Nat Phys. Sci ,* 230, 185

Effect of Strong Magnetic Field on Cosmic Quark-Hadron Phase Transition and Baryon Inhomogeneity

Somenath Chakrabarty †*Department of Physics, University of Kalyani, West Bengal, India 741 235, and Inter-University Centre for Astronomy and Astrophysics, Post Bag 4, Ganeshkhind, Pune, India 411 007*

Abstract. The effect of intense magnetic field on the cosmic quark-hadron phase transition and also on the baryon number inhomogeneity has been investigated using phenomenological MIT bag model for the quark sector For the sake of simplicity an ideal gas equation of state has been considered for the hadronic phase

1. Introduction

In the past few years a lot of work has been done on the effect of strong magnetic field on various properties of dense astrophysical and cosmological matter These works are mainly related to the emissions from magnetized neutron matter (Kaminker *et al* 1991, 1992), electron-induced electromagnetic and weak processes (Shul'man 1991), and the Landau diamagnetism and Pauli paramagnetism of dense nuclear matter (Shul'man 1991, Fushiki *et al.* 1992) Very recently the effects of such intense magnetic field on the primordial nucleo-synthesis and also on the expansion rate of the universe micro-second after the Big Bang have been studied by Schramm *et al.* (Cheng *et al* 1993, 1994) and Grasso & Rubinstein (1994) In recent years some interesting work has also been done on quantum electrodynamics in the presence of strong external magnetic field (Persson & Zeitlin 1994, Zeitlin 1994; Danielsson & Grasso 1995) and also on the stability of matter in the presence of strong magnetic field (Vshivtsev & Serebryakova 1994, Elliott *et al.* 1995) In a series of publications we have also reported some new results on the effect of strong magnetic field on first order quark-hadron phase transition at the core of a neutron star In particular, we have studied the stability of strange quark matter, equation of state of such stable phase and also the nucleation of quark bubbles in metastable neutron matter in the presence of strong magnetic field We have seen that strange quark matter becomes more stable in the presence of strong magnetic field and the equation of state of magnetized strange quark matter differs significantly from that of a non-magnetized one The most interesting observation was that there cannot be any quark droplet nucleation in metastable neutron matter if the strength of the magnetic field is strong enough to make the quarks populate the Landau levels (Chakrabarty & Goyal 1994, Chakrabarty 1994, 1995a, b).

---

†Permanent address

In all these reported results, mentioned above, the possible effects of strong magnetic fields on cosmic QCD phase transition have not been considered Initially the universe is at a high temperature and in the quark-gluon plasma phase The net baryon number of the universe resides entirely in the primordial quark soup Due to cosmic expansion the temperature of the quark soup decreases and near the critical temperature, T_c, a transition to colour singlet hadronic phase takes place During phase separation the baryon number is transported to the hadronic phase mainly by the formation of nucleons which are the lightest baryons. The other possible hadrons are mostly light mesons, which do not carry the baryon number Now, the quarks in the quark gluon plasma are almost massless and carry 1/3 baryon number, whereas the mass of the lightest baryon, the nucleon, is ~ 940 MeV. A simple thermodynamic calculation shows that the baryon number solubility of primordial quark soup is much higher than that of hadronic matter at the critical temperature T_c. This gives rise to inhomogeneity in the baryon number distribution This particular aspect has also not been studied in the presence of strong magnetic field. The aim of this paper is to investigate the effect of strong magnetic field on both cosmic quark-hadron phase transition and baryon inhomogeneity

In §2 we give the basic thermodynamic formalism of quark matter in the presence of strong magnetic field In sections 3 and 4 we study the effect of strong magnetic field on the cosmic QCD phase transition and on the baryon inhomogeneity Section 5 contains the conclusion of this work

2. Formalism

As is well known, the energy of a charged particle changes significantly in the quantum limit if the magnetic field strength is equal to or greater than some critical value $B_m^{(c)} = m_i^2 c^3/(q_i \hbar)$ in Gauss; where m_i and q_i are respectively the mass and charge (absolute value) of the particle (e g , $q_i = 2e/3$ for u-quark, $e/3$ for d and s quarks, here $e = |e|$ is the absolute value of electronic charge), $\hbar$ and c are respectively the reduced Planck constant and velocity of light, both of which along with the Boltzmann constant k_B are taken to be unity in our choice of units For an electron of mass 0 5 MeV, the strength of this critical field as mentioned above is $B_m^{(c)(e)} = 4 \cdot 4 \times 10^{13} G$, whereas for a light quark of current mass 5 MeV, this particular value becomes $\sim 10^2 \times B_m^{(c)(e)}$, arise for s-quark of current mass 150 MeV, it is $\sim 10^{20} G$, which is too high to realize at the core of a neutron star. But the possibility of such high magnetic field cannot be discarded in the case of the early universe (Vachaspati 1991). The critical magnetic field as defined above is the typical strength at which the cyclotron lines begin to occur, and in this limit the cyclotron quantum is of the order of or greater than the corresponding rest energy This is also equivalent to the requirement that the de-Broglie wavelength is of the order of or greater than the Larmor radius of the particle in the magnetic field.

To study the cosmic QCD transition in the early universe in the presence of a strong magnetic field, we have considered the conventional MIT bag model. For the sake of simplicity we assume that quarks move freely within the system The current masses of both u and d-quarks are assumed to be extremely low (in our actual calculation we have taken the current mass for both of them to be 5 MeV, whereas for s-quark, the current mass is taken to be 150 MeV)

For a constant magnetic field along the z-axis ($\vec{B}_m = B_{m,(z)} = B_m = $ constant), the single particle energy eigen value is given by

$$\varepsilon_{k,n,s}^{(i)} = [k^2 + m_i^2 + q_i B_m (2n + s + 1)]^{1/2}, \tag{1}$$

where $n = 0, 1, 2, \ldots$, being the principal quantum numbers for allowed Landau levels, $s = \pm 1$ refers to spin up $(+)$ or down $(-)$ states and k is the component of particle momentum along the direction of external magnetic field. Setting $2\nu = 2n + s + 1$, where $\nu = 0, 1, 2, \ldots$, we can rewrite the single particle energy eigen value in the following form

$$\varepsilon_\nu^{(i)} = [k^2 + m_i^2 + q_i B_m 2\nu]^{1/2} \tag{2}$$

Now it is very easy to show that the $\nu = 0$ state is singly degenerate while all other states with $\nu \neq 0$ are doubly degenerate

The general expression for the thermodynamic potential of the system at temperature $T = \beta^{-1}$ is given by

$$\Omega = -T \ln Z = \sum_i \Omega_i V + BV, \tag{3}$$

where Z is the grant-partition function and the explicit form of the thermodynamic potential density for the ith species is given by

$$\Omega_i = -\frac{Tg_i}{(2\pi)^3} \int d^3 k \ln (1 + \exp (\beta(\mu_i - \varepsilon_i))), \tag{4}$$

where g_i is the degeneracy of the ith species ($= 6$ for a quark or an antiquark), B is the bag pressure and V is the volume occupied by the system. The sum in equation (3) is over u, d, s-quarks and their antiparticles. We assume that for antiparticles the chemical potential $\bar{\mu}_i = -\mu_i$, i.e. they are in chemical equilibrium with respect to annihilation processes.

Now let us consider the necessary changes to be made in equation (4) if a strong external magnetic field is present in the system. Here we shall investigate the magnetism arising from quantization of orbital motion of charged particles in the presence of a strong magnetic field. We know that if the magnetic field is along z-axis, the path of the charged particle will be a regular helix whose axis lies along the z-axis and whose projection on an x-y plane is a circle. If the magnetic field is uniform, both the linear velocity along the field direction and the angular velocity in the x-y plane will be constant, the latter arises from the constant Lorentz force experienced by the particle. Quantum mechanically the energy associated with the circular motion in the x-y plane is quantized in units of $2q_i B_m$. The energy associated with the linear motion along the z-axis is also quantized; but in view of the smallness of the energy intervals, they may be taken as continuous variables. We thus have equation (1) or (2) as single particle energy eigen value. Now, these magnetized energy levels are degenerate because they result from an almost continuous set of zero field levels. All those levels for which the values of the quantity $k_x^2 + k_y^2$ lie between $2q_i B_m \nu$ and $2q_i B_m (\nu + 1)$ now coalesce into a single level characterized by the quantum number ν. The number of these levels is given by

$$\frac{S}{(2\pi)^2} \int\int dk_x dk_y = \frac{S q_i B_m}{2\pi}, \tag{5}$$

here S is the area of the orbit in the x-y plane. This expression is independent of v. Then, in the integral of the form $\int d^3 k f(k)$, we can replace $\int\int dk_x dk_y$ by the expression given above, whereas the limit of k_z, which is a continuous variable, ranges from $-\infty$ to $+\infty$. Then we can rewrite equation (4) for the thermodynamic potential density in the presence of a strong magnetic field in the form

$$\Omega_i = -T\frac{q_i g_i B_m}{2\pi^2} \sum_{v=0}^{\infty} \int_0^{\infty} dk_z \ln(1 + \exp(\beta(\mu_i - \varepsilon_v^{(i)}))). \tag{6}$$

We have used equation (4) for s and $\bar{s}$ if $B_m < 10^{20} G$ and equation (6) for u, d-quarks and their anti-particles. Whereas for $B_m > 10^{20} G$, equation (6) has been used for all the constituents. In equation (4), $\varepsilon_i = (k^2 + m_i^2)^{1/2}$, whereas in equation (6), it is given by equation (2).

The expression for kinetic pressure of the system is given by

$$P = -\sum_i \Omega_i, \tag{7}$$

and the number density of the ith species is given by

$$n_i = -\left(\frac{\partial \Omega_i}{\partial \mu_i}\right)_T \tag{8}$$

3. Cosmic quark-hadron phase transition

Assuming for the sake of simplicity that only nucleons and pions are present in the hadronic phase and that they obey the free hadronic gas equation of state, the conditions to be satisfied by the co-existing phases are

$$\mu_p = \mu_d + 2\mu_u, \tag{9}$$

$$\mu_n = \mu_u + 2\mu_d, \tag{10}$$

$$\mu_\pi = 0, \tag{11}$$

$$P_h = P_q, \tag{12}$$

and

$$T_h = T_q = T_c. \tag{13}$$

The chemical equilibrium conditions are also valid for anti-quarks and anti-hadrons i.e. we can write down equations similar to equations (9) and (10) for $\bar{q}$, $\bar{n}$ and $\bar{p}$ (where $q = u$ or d). We also assume that the condition of β-equilibrium is satisfied in both the quark-gluon and hadronic phases. For the anti-particles, the chemical potential $\bar{\mu}_i = -\mu_i$. The expressions for kinetic pressures are then obtained from equation (7) by replacing Ω_i either by equation (4) or (6), depending on whether $B_m < B_m^{(c)(i)}$ or $> B_m^{(c)(i)}$, respectively.

In Fig. 1 we have shown the phase diagram (n_B vs T diagram) for such a mixed phase of quark-gluon plasma and hadronic matter. The dotted curve is for $B_m = 0$, whereas the solid curve is for $B_m = 10^3 \times B_m^{(c)(e)}$. This figure shows that the phase diagram changes significantly in the presence of a strong magnetic field.
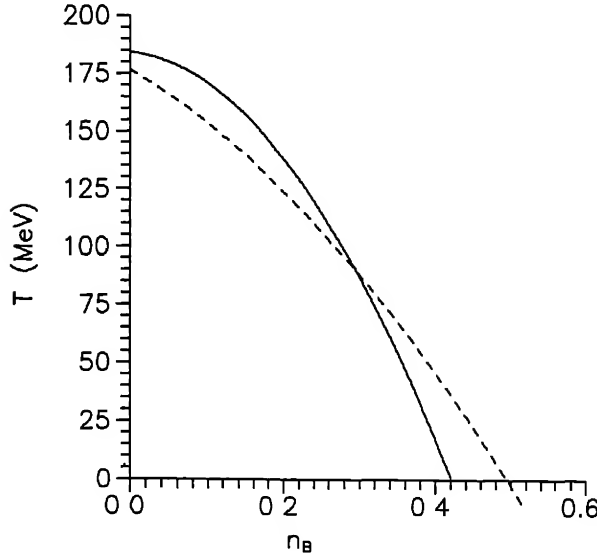
Figure 1. Phase diagram ($T - n_B$ plot) for a mixture of QGP and hadronic matter The dotted curve is for $B_m = 0$ and the solid one is for $B_m = 10^3 \times B_m^{(c)(e)}$.

4. Baryon inhomogeneity

Before the quark-hadron phase transition in the early universe, the quark gluon plasma had almost an equal number of quarks and anti-quarks, since the baryon number of the universe is so small,

$$\frac{n_B}{n_\gamma} \sim 10^{-9}, \tag{14}$$

where n_B ad n_γ are respectively the net baryon number and photon number densities in the early universe This ratio is too small to affect the dynamics or the evolution of the early universe. Since the present universe is matter dominated, all the anti-baryons must have been annihilated with their counterparts

Now in the quark gluon phase, the baryon number is carried by the quarks, which are almost massless (except s-quark, whose mass is ~ 150 MeV) On the other hand, in the hadronic sector, the lightest baryons are nucleons of mass ~ 940 MeV. Therefore the baryon number prefers to reside in the quark gluon phase during phase transition (Witten 1984), or in other words, the baryon number solubility of primordial quark soup is much higher than that of hadronic phase at T_c We can estimate the ratio of baryon number densities in these two phases at T_c, given by

$$R = \frac{n_q^{(B)}}{n_h^{(B)}}. \tag{15}$$

A simple non-relativistic thermodynamic calculation (Witten 1984) shows that $R \sim \exp(M_h/T_c)$, where M_h is the hadronic mass $\gg T_c$. Therefore the ratio R is a large

Table 1.

$B_m/B_m^{(c)(e)}$	T_c(MeV)	$n_q^{(B)}/n_h^{(B)}$
0 0	100	455 4
	150	33·4
	180	14 7
	200	9 9
10^2	100	2732 69
	150	200 66
	180	88 49
	200	59 21
10^3	100	2783 01
	150	201 39
	180	89 03
	200	61 35
10^5	100	51908 2
	150	1695 85
	180	520 75
	200	285 51

number. It has been shown that $R \approx 6$ or 100 for $T_c = 200$ or 100 MeV respectively (Kurki-Suonio 1988, 1991; Fuller *et al.* 1988; Kapusta & Olive 1988)

Since the net baryon number of the universe is small, $\mu_B = 3\mu_q \to 0$. Then the ratio R is given by

$$R = \lim_{\mu_q \to 0, \mu_B \to 0} \frac{1}{3} \frac{(\partial \Omega_q / \partial \mu_q)_{T=T_c}}{(\partial \Omega_B / \partial \mu_B)_{T=T_c}}. \tag{16}$$

Using the explicit form of $\Omega_i (i = q$ or $B)$, it is very easy to show that in the limiting condition $n_B \to 0$, the ratio R reduces to 0/0 form. Then by L'Hospital's theorem, we have

$$R = \lim_{\mu_q \to 0, \mu_B \to 0} \frac{1}{3} \frac{(\partial^2 \Omega_q / \partial \mu_q^2)_{T=T_c}}{(\partial^2 \Omega_B / \partial \mu_B^2)_{T=T_c}}, \tag{17}$$

which is not in the 0/0 form. Using the explicit form of the second derivatives as written above we have calculated R for four different values of $T_c (= 100, 150, 180$ and 200 MeV) and for $B_m = 0, 10^2 \times B_m^{(c)(e)}, 10^3 \times B_m^{(c)(e)}$ and $10^5 \times B_m^{(c)(e)}$ In Table 1 we have shown the variation of R with T_c and B_m. The variation of R with T_c has already been reported and the results presented here are consistent with those of old published data. The variation of R with B_m has not been done before. If $B_m > 10^2 \times B_m^{(c)(e)}$, R changes significantly from zero field values. If this is true for the early universe, this could possibly lead to a very high baryon number inhomogeneity, which could modify the picture at the end of the quark-hadron phase transition. It is also obvious that the presence of a strong magnetic field favours the formation of quark nuggets during the early universe quark-hadron phase transition, which is expected to be one of the natural candidates for baryonic dark matter.

5. Conclusions

We have seen that in the presence of a strong magnetic field greater than the corresponding critical field, the phase diagram for a mixture of quark gluon plasma and hadronic matter differs significantly from that for zero magnetic field case.

The other interesting observation is that the baryon number inhomogeneity in the early universe increases by a few orders of magnitude if the magnetic field strength becomes greater than $10^2 \times B_m^{(c)(e)}$.

If this theoretical prediction is correct, then it may have some effect on the primordial nuclear abundances and also on the formation of quark nuggets during the first order quark hadron phase transition in the early universe, which in turn affects the Big Bang nucleo-synthesis.

Here we have given a very simplified picture of the baryon number transport during the first order cosmic quark hadron phase transition in the presence of a strong magnetic field. Such calculations should only be used to indicate the order of magnitude of the baryon number penetrability and a rough comparison with zero magnetic field case.

References

Chakrabarty, S. 1994, *Astr. Space Sci.*, **213**, 121.
Chakrabarty, S., Goyal, A 1994, *Mod. Phys Lett*, A9, 3611.
Chakrabarty, S 1995a, *Phys Rev.*, **D51**, 4591.
Chakrabarty, S 1995b, *Ann Phys* (submitted).
Cheng, B., Schramm, D N, Truran, J. W 1993, *Phys Lett*, **B316**, 521.
Cheng, B, Schramm, D N, Truran, J. W 1994, *Phys. Rev*, **D49**, 5006
Danielsson, Ulf, H, Grasso, D 1995, Preprint UUITP-2/95
Elliot, Lieb, Michael, Loss, Jan Philip, Solovej 1995, GATECH, Preprint.
Fuller, G M, Mathews, G J, Alcock, C. R 1988, *Phys Rev*, **D37**, 1380.
Fushiki, I *et al* 1992, *Ann Phys*, **216**, 29.
Grasso, D, Rubinstein, H R 1994, Preprint Uppsala-UUITP 14/1994 (to appear in *Astro-particle Phys*)
Kaminker, A D *et al* 1991, *Soviet Astr Lett*, **17**, 450
Kaminker, A. D. *et al.* 1992, *Phys Rev.*, **D46**, 3256
Kapusta, J I., Olive, K A 1988, *Phys. Lett*, **209B**, 295
Kurki-Suonio, H. 1988, *Phys. Rev*, **D37**, 2104
Kurki-Suonio, H. 1991, *Nucl. Phys*, **B24**, 67
Persson, D., Zeitlin, V. 1994, Preprint FIAN/TD/94-01
Shul'man, G A 1991, *Soviet Astr*, **35**, 50, 492
Vachaspati, T 1991, *Phys Lett.*, **B265**, 258.
Vshivtsev, A S, Serebryakova, D V 1994, *JETP*, **79**, 17
Witten, E 1984, *Phys. Rev*, **D30**, 272
Zeitlin, V 1994, Preprint FIAN/TD/94-10

VV Orionis – Improved Elements

M. B. K. Sarma & P. Vivekananda Rao *Centre for Advanced Study in Astronomy, Osmania University, Hyderabad 500 007, India*

Abstract. The *UBV* light curves obtained by Duerbeck (1975) and $H\alpha$ (wide) and $H\alpha$ (narrow) light curves obtained by Chambliss & Davan (1987) of the detached eclipsing binary VV Orionis (VV Ori) were analysed using the Wilson-Devinney method fixing the two parameters T_h(25,000 K) and q(0 4172), resulting in the following absolute elements: $A = 13.605 \pm 0.031 R_\odot$, $R_h = 5.03 \pm 0.03 R_\odot$, $R_c = 2.43 \pm 0.02 R_\odot$, $M_{bol,h} = -5.18 \pm 0.11$, $M_{bol,c} = -1.54 \pm 0.06$, $m_h = 10.81 \pm 0.42 m_\odot$ and $m_c = 4.51 \pm 0.41 m_\odot$ The de-reddened colours obtained from applying the reddening corrections of $E(B-V) = 0^m.05$ and $E(U-B) = 0^m.04$, and the derived temperatures of the components, gave spectral types of $B1.5V$ for the primary and $B4-5V$ with an *UV* excess of $0^m.3$ for the secondary component. A comparison of the $\log L$ and $\log T_e$ of the components with the observed ZAMS shows the primary component to be a little above and the secondary component to be a little below/or on the ZAMS A comparison of the properties of the components of VV Ori and a few other detached systems with the normal stars in the $\log L$, $\log R$ and $\log T_e$ versus $\log m$ planes, indicated a need for either a readjustment of the scales of the above parameters or modifications in the theoretical models. From the position of the components on the evolutionary tracks of Pop I composition computed by Schaller *et al.* (1992) it is noticed that while the primary component of VV Ori had slightly evolved along the main-sequence, its secondary is still unevolved. The age of VV Ori is found to be 10 ± 1 million years and it is at a distance of 368 ± 10 pc.

Key words: Eclipsing binaries—detached—VV Ori—elements—individual.

1. Introduction

VV Orionis (HR 1868 = HD 36695, $P = 1^d.4854$) was first found to be a light variable by Barr in 1903 (Barr 1905). It is an eclipsing binary of type *EB* with both the components belonging to the main sequence of spectral type *B*. There were many spectroscopic and photometric investigations of this system. The spectroscopic studies of Struve & Luyten (1949) showed this system to be single-lined and they suggested a mass ratio of unity for the components. From their spectral studies, Beltrami & Galeotti (1970) estimated the mass ratio to be about 0.5. Using high dispersion spectra, Duerbeck (1975) could locate a few lines of the secondary component and was thus able to get an improved mass ratio of 0.45. However, the detection of the secondary lines had been questioned (Andersen 1976, Popper 1981) and the value of the mass-ratio remained ambiguous.
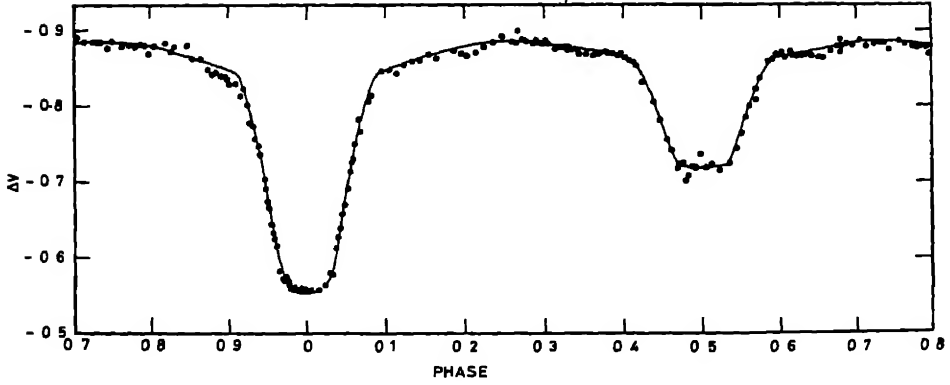
Figure 1a. VV Ori. Light curve in yellow. Filled circles represent observations (normals) and the solid line represents the theoretical curve obtained from the elements obtained from the combined V, B, $H\alpha$ (n) solution (Table 2, col. 2).
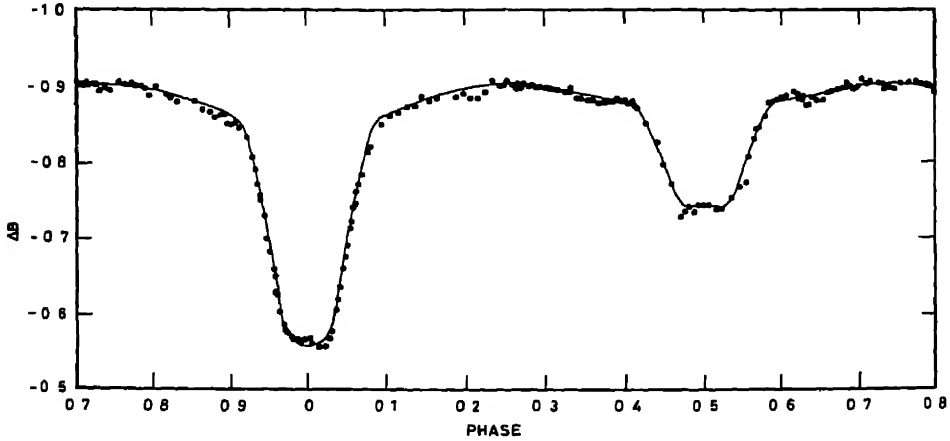
Figure 1b. VV Ori Same as in Fig. 1a, for blue

Popper (1993) reported the detection of the lines of the secondary component of VV Ori. His radial velocity curves of the two components yielded a mass-ratio of 0.4172. Even though the variation of the center of mass velocity V_0 is poorly determined, Popper (1993) suggests that "One can derive fundamental properties of VV Ori, making use of the results in (his) Table 3, that should be improvements over previously published work". Hence we felt it useful to re-analyse the published photometric data with the newly derived mass-ratio of 0.4172 and obtain reliable photometric elements for VV Ori The results of the analysis of a few published light curves of this system is given below.

2. Earlier analysis of the light curves of VV Ori

Of all the published light curves of VV Ori, the *UBV* data of Duerbeck (1975) is the most extensive. Duerbeck himself had analysed his data using the Russell-Merrill method (1952). Eaton (1975) analysed a series of OAO-2 light curves of this system
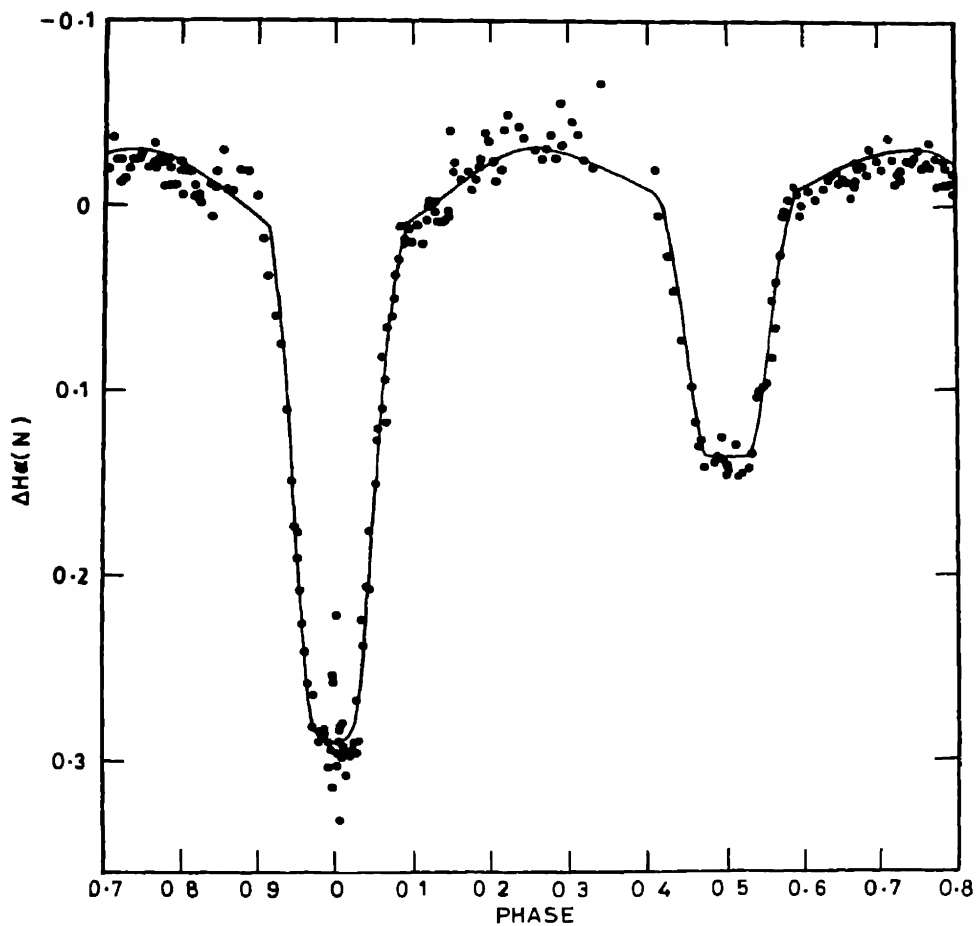
Figure 1c. VV Ori Same as in Fig 1a, for $H\alpha$ (n)
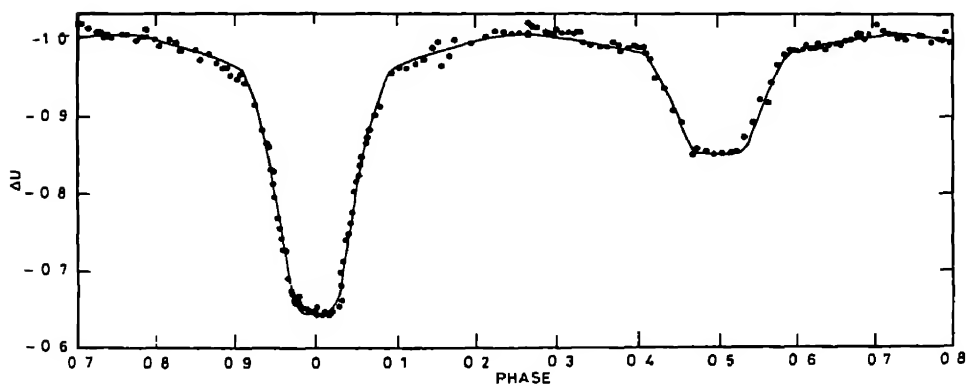
Figure 1d. VV Ori Same as in Fig 1a, for ultraviolet Here, the theoretical curve is calculated using the elements given in (Table 2, col 3)
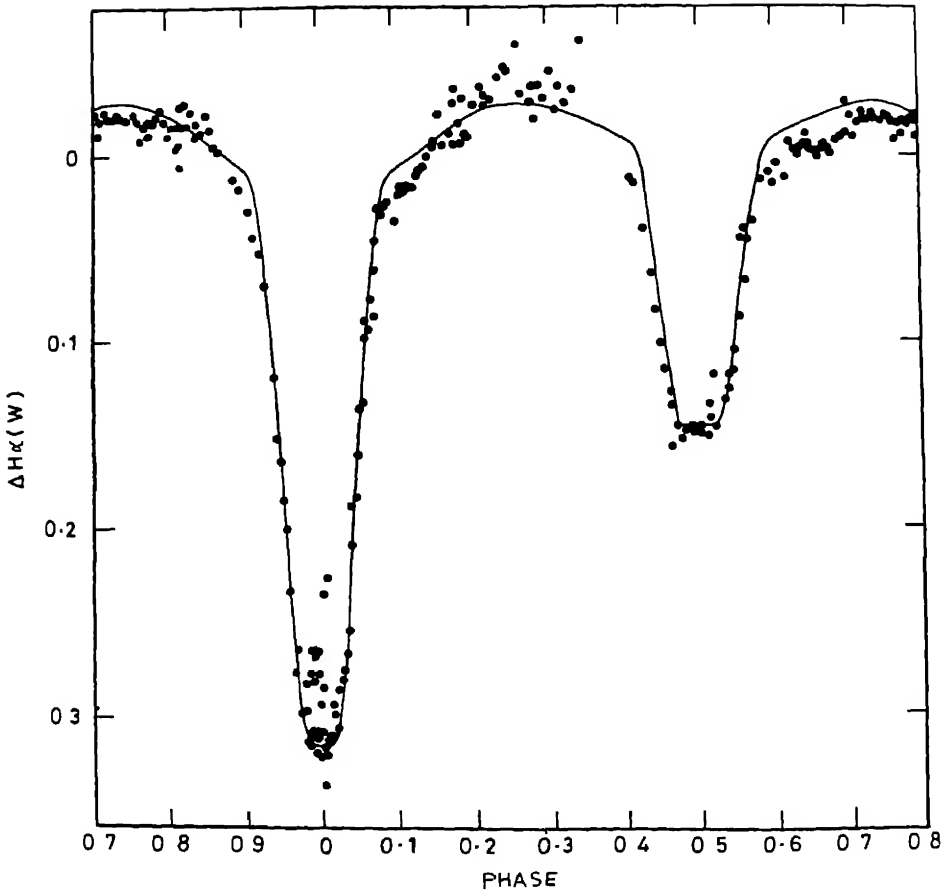
Figure 1e. VV Ori. Same as in Fig 1a for $H\alpha$ (w) Here, the theoretical curve is calculated using the elements given in (Table 2, col 4)

which covered the wavelength range of 1300–4300Å, using a computational model developed by Lucy (1968) Cester *et al.* (1978) analysed Duerbecks's data using Wood's WINK method. Budding & Najim (1980) analysed Eaton's (1975) data with Kopal's Frequency Domain method Chambliss & Leung (1982) solved their own *UBVuvby* light curves with the Wilson-Devinney method. Giuricin *et al.* (1983) and Chambliss (1983) analysed the data of Chambliss & Leung (1982) with Wood's WINK programme Chambliss & Davan (1987) analysed their $H\alpha$ (wide) and $H\alpha$ (narrow) band observations of this system using the WINK programme. All the above analyses, wherever needed, used a mass-ratio of 0.45.

3. Present study

3.1 *Data*

Since an improved mass-ratio for VV Ori (Popper 1993) is now available and as Wilson-Devinney (1971) synthetic light curve method (W-D) is regarded as the most reliable among

Table 1. VV Ori. Elements obtained from the solution of individual light curves using W-D method

Element		Initial parameter	U	B	V	$H\alpha\,(w)$	$H\alpha\,(n)$
	1	2	3	4	5	6	7
$*T_{e,h}K$			25,000	25,000	25,000	25,000	25,000	25,000
$T_{e,c}K$			15,550	15,667	15,544	15,544	15,560	15,571
$*q$			0 4172	0 4172	0 4172	0 4172	0 4172	0 4172
$i°$			86 0	86.050	86 108	86 128	86 078	86 108
r_h	pole point side back	0 368	0.3700	0 3630	0 3640	0 3572	0.3612
			0.4100	0 3989	0 4006	0 3901	0 3962
			0.3846	0 3765	0 3777	0 3698	0 3744
			0.3971	0 3879	0 3893	0 3804	0 3855
r_c	pole point side back	0 182	0 1859	0 1774	0 1774	0 1822	0 1774
			0 1936	0 1837	0 1837	0 1893	0 1837
			0 1879	0 1791	0 1791	0 1841	0 1792
			0 1922	0 1826	0 1826	0 1881	0 1827
	U	0.894	0 9194	0 9149	0 9082	0 8934	0 9010
	B	0 886					
$L_h/L_h + L_c$	V	0 878					
	$H\alpha\,(w)$	0 901					
	$H\alpha\,(n)$	0 903					
	U	0 106	0.0806	0 0851	0 0918	0 1066	0.0990
	B	0 114					
$L_c/L_h + L_c$	V	0 122					
	$H\alpha\,(w)$	0 099					
	$H\alpha\,(n)$	0 097					
l_3		0 0	0 0	0 0	0.0	0 0	0 0
$*x_h$	U	0 320					
	B	0.390					
	V	0 325					
	$H\alpha\,(w)$	0.240					
	$H\alpha\,(n)$	0.240					
$*x_c$	U	0 390					
	B	0.470					
	V	0 370					
	$H\alpha\,(w)$	0 250					
	$H\alpha\,(n)$	0 240					
$*A_h = A_c$		1 0					
$*G_h = G_c$		0 25					

*Fixed parameters

all the available synthetic light curve methods, we re-analysed the *UBV* light curves of Duerbeck (1975) and $H\alpha\,(w)$ and $H\alpha\,(n)$ light curves of Chambliss & Davan (1987) with this method using Popper's mass-ratio of 0.4172 The data published by Duerbeck (1975) contains $655U$, $675B$ and $668V$ observations of VV Ori As the memory of the computer available with the department is limited, to save computer time, we formed $163U$, $167B$ and $171V$ normal points from these observations. During the phases of the primary eclipse, observations within a phase range of about 0.003 (1°) and at the

Table 2. VV Orı Elements obtained from the combined solution of B, V & $H\alpha$ (n) light curves

Element		Combined solution for B, V & $H\alpha(n)$	Parameters used for fitting the U & $H\alpha$ (w) light curves	
			U	$H\alpha$ (w)
1		2	3	4
*$T_{e,h}K$		25,000	25,000	25,000
$T_{e,c}K$		$15,579 \pm 28$	15,579	15,579
*q		0 4172	0.4172	0 4172
ι		$86\,09 \pm 0\,05$	86 09	86.09
r_h	pole point	$0\,3582 \pm 0.0013$	$0.3633 \pm 0\,0016$	$0\,3554 \pm 0\,0033$
	side back	$0.3916 \pm 0\,0012$	$0\,3994 \pm 0\,0017$	$0.3875 \pm 0\,0034$
		$0\,3709 \pm 0\,0013$	$0.3768 \pm 0\,0016$	$0\,3677 \pm 0\,0034$
		0.3816 ± 0.0012	$0\,3883 \pm 0\,0017$	$0\,3781 \pm 0\,0034$
r_c	pole point	$0\,1762 \pm 0\,0012$	$0\,1838 \pm 0\,0018$	$0\,1807 \pm 0\,0034$
	side back	$0\,1823 \pm 0\,0013$	$0.1912 \pm 0\,0018$	$0.1875 \pm 0\,0035$
		$0\,1778 \pm 0\,0012$	$0\,1858 \pm 0\,0018$	$0\,1826 \pm 0\,0036$
		$0\,1813 \pm 0\,0013$	$0\,1899 \pm 0\,0019$	$0\,1864 \pm 0\,0035$
	B	$0\,9077 \pm 0\,0015$	$0\,9147 \pm 0\,0017$	$0\,8938 \pm 0\,0284$
$L_h/L_h + L_c$	V	$0\,9023 \pm 0\,0015$		
	$H\alpha$ (n)	$0\,9005 \pm 0\,0270$		
	B	0.0923	0 0853	0.1062
$L_c/L_h + L_c$	V	0 0977		
	$H\alpha$ (n)	0 0995		
l_3		0 0	0.0	0 0

*Fixed parameters

remaining portions of the light curve points within a phase range of 0 01 (4°) were combined to form one normal point By using the normal points instead of the actual observations, the distortions in the light curve, if any, might have been obliterated, but the final results will not be affected (Chambliss 1983) The $H\alpha$ (w) and $H\alpha$ (n) data of Chambliss & Davan (1987) contain 692 $H\alpha$ (w) and 686 $H\alpha$ (n) observations. All these observations were also formed into 209 $H\alpha$ (w) and 213 $H\alpha$ (n) normal points. For our analysis these normal points were used and the number of points in each normal was taken as its weight. These normal points are shown as filled circles in Fig. 1(a–e).

3 2 *Methodology*

As already mentioned, the Wilson-Devinney (1971) method was used for solving the above light curves For initiating the W-D method, one needs reliable preliminary elements. For this purpose we used the values of the inclination, ι, fractional radii, r_h and r_c and the luminosities, L_h and L_c for the UBV pass bands given by Duerbeck (1975). The luminosities for $H\alpha$ (w) and $H\alpha$ (n) pass bands were taken from Chambliss & Davan (1987). The values of temperatures $T_{e,h}$ and $T_{e,c}$ and the mass-ratio are from Popper (1993) The limb-darkening coefficients for UBV pass bands were from Gryger (1972) and for $H\alpha$ (w) and $H\alpha$ (n) were from Chambliss & Davan (1987). These preliminary elements are given in Table 1, col. 2

Table 3a. VV Ori Elements obtained from the *UBV* data of Duerbeck (1975)

Element Method		Duerbeck (1975) R-M	Cester *et al* (1978) WINK	Present studies W-D
$*T_{e,h}K$		—	25,000	25,000
$T_{e,c}K$		—	16,190	15,580
$*q$		0.450 ± 0.014	0.45	0.417
$\imath°$		86.1 ± 0.2	86.3 ± 0.5	86.09 ± 0.05
r_h		0.368 ± 0.002	0.364 ± 0.003	0.3702 ± 0.0012
r_c		0.182 ± 0.002	0.177 ± 0.002	0.1784 ± 0.0012
L_h	U	0.894	0.952	0.915
	B	0.886	0.968	0.908
	V	0.878	0.965	0.902
L_c	U	0.106	0.048	0.085
	B	0.114	0.032	0.092
	V	0.122	0.035	0.098
m_h/m_O		7.60	7.6	10.81
m_c/m_O		3.42	3.4	4.51
R_h/R_O		4.47	4.44	5.03
R_c/R_O		2.21	2.13	2.43
$M_{h,v}$		-2.58	—	-2.59
$r(pc)$		372	—	368

*Assumed parameter.

Table 3b. VV Ori Elements obtained from the $H\alpha(w)$ & $H\alpha(n)$ data of Chambliss & Davan (1987).

Element Method Wavelength	Chambliss & Davan (1987) WINK		Present studies (individual solutions) W-D	
	$H\alpha(w)$	$H\alpha(n)$	$H\alpha(w)$	$H\alpha(n)$
$*T_{e,h}K$	25,000	25,000	25,000	25,000
$T_{e,c}K$	$15,690 \pm 150$	$15,760 \pm 170$	$15,560 \pm 50$	$15,571 \pm 54$
$*q$	0.45	0.45	0.4172	0.4172
$\imath°$	83.6 ± 0.5	85.5 ± 0.8	86.078 ± 0.140	86.108 ± 0.150
r_h	0.367 ± 0.003	0.361 ± 0.004	0.3691 ± 0.0035	0.3737 ± 0.0036
r_c	0.179 ± 0.003	0.173 ± 0.004	0.1848 ± 0.0036	0.1798 ± 0.0038
L_h	0.901	0.903	0.893	0.901
L_c	0.099	0.097	0.107	0.099
l_3	0.0	0.0	0.0	0.0

*Assumed parameter

According to the principles of the W-D method we adjusted the following parameters. the inclination $\imath$, the surface potentials Ω_h and Ω_c, the relative monochromatic luminosity L_h, the temperature of the secondary $T_{e,c}$ and the third light l_3. The temperature of the primary component, $T_{e,h}$ (25,000 K) and the mass-ratio $q(0.4172)$

Table 3c. VV Ori Elements obtained from the *UBVubvy* data of Chambliss & Leung (1982)

Element Method		Chambliss & Leung (1982) W-D	Giuricin et al. (1983) WINK	Chambliss (1983) WINK
$*T_{e,h}K$		21,000	26,000	25,000
$T_{e,c}K$		12,835	17,017	15,957
$*q$		0 4568 ± 0 0012	0 40	0 45
i°		90 ± 0.49	86 3	85 60 ± 0 17
r_h		0 3530 ± 0.0004	0 362 ± 0 003	0 3627 ± 0 0017
r_c		0 1709 ± 0 0004	0.177 ± 0 004	0 1764 ± 0 0014
L_h	U	0 9446	0 924	0 925
	B	0 9115	0 907	0 895
	V	0 9026	0 904	0 891
L_c	U	0 0554	0 076	0 075
	B	0 0885	0 093	0 105
	V	0 0974	0 096	0 109
l_3		0.0	0 0	0 0

*Assumed parameter

Table 3d. VV Ori. Elements obtained from the OAO-2 data

Element Method	Eaton (1975) Computational method of Lucy (1968)	Budding & Najim (1980) Kopal's frequency domain
$*T_{e,h}K$	21,000	—
$T_{e,c}K$	11,800 ± 500	—
$*q$	0 458 ± 0 050	—
i°	84 5 ± 0 5	87 5 ± 1.3
r_h	0 3790 ± 0.0040	0.3708 ± 0.0026
r_c	0 1745 ± 0 0040	0 1748 ± 0 0080

*Assumed parameters

were treated as fixed parameters. It is expected that analysis of the light curves with fixed T_h and q at known values should yield most reliable elements The limb-darkening coefficients x_h and x_c, the albedos A_h and A_c and the gravity darkening coefficients G_h and G_c were also kept constant. From our earlier studies we noticed that the choice of these coefficients had negligible effect on the derived elements. As it is now well established that VV Ori is a detached system, we used code-2 of the W-D method meant for detached systems. A sufficient number of runs of the DC programme was made till the sum of the residuals $\sum \omega \, (O\text{-}C)^2$ showed a minimum and the corrections to the parameters became smaller than their probable errors In order to check the internal consistency of the results (Popper 1984) separate solutions for each of the $UBVH\alpha$ (w) and $H\alpha$ (n) light curves were made. These results are given in cols. 3, 4, 5, 6 and 7 of Table 1. In none of the solutions was the third light l_3 present.

From the results of the above analysis, it is noticed that the relative fractional sizes r_h and r_c derived from the U solution, are slightly larger than those derived from B, V and $H\alpha$ (n) pass bands. Since only a small discrepancy exists between the r_h and r_c values derived from the $H\alpha$ (w) and $H\alpha$ (n) pass bands, and that the r_h and r_c values of $H\alpha$ (n) solution are almost identical with those of B and V solutions and in order not to combine many light curves and complicate the analysis, it was decided to get a combined solution only for B, V and $H\alpha$ (n) and as before, keeping $T_{e,h}$ and q as fixed parameters, another solution was made for the combined B, V and $H\alpha$ (n) light curves. These results are given in Table 2, col. 2 The third light l_3 is absent in this solution also. Using these elements, we have fitted the U and $H\alpha$ (w) light curves. In doing so we had kept all the parameters except L_h as fixed parameters The final parameters used for fitting the U and $H\alpha$ (w) light curves are given in Table 2, cols 3 and 4 For calculating the absolute elements, we used the elements obtained from the combined solution only However for obtaining the $(U\text{-}B)$ colours of the components, we used the $L_{h,u}$ and $L_{c,u}$ values given in Table 2, col 3

The theoretical curves obtained from the elements given in Table 2 for the $UBVH\alpha$ (w) and $H\alpha$ (n) light curves are shown as solid lines in Fig 1(a–e) The fit of the theoretical curves to the observed normals is quite satisfactory. In Table 3a we have given for comparison the elements derived from the UBV data of Duerbeck (1975) Table 3b gives the elements obtained by Chambliss & Davan (1987) from the analysis of their $H\alpha$ (w) and $H\alpha$ (n) data In Tables 3c and 3d we have compiled the elements obtained by various investigators using the same data but different methods of solution It can be noticed that the values of the derived parameters depend only on the method of analysis and not on the underlying data. In such analysis the most significant differences exist between the parameter i and L The high value of 90° obtained for i from the $UBVuvby$ data using the W-D method by Chambliss & Leung (1982) (Table 3c) may be attributed to their combining many light curves which might have complicated the solution.

4. Spectral types

From the derived luminosities of V and B pass bands for the combined solution (Table 2, col. 2) and U pass band (Table 2, col 3) and using the corresponding differential magnitudes for unit luminosity at the quadrature [$\Delta V = -0^m 885$, $\Delta B = -0^m 902$, $\Delta U = -1^m.006$] and the standard magnitudes and colours of $V = 6^m.24$, $(B\text{-}V) = -0^m.18$ and $(U\text{-}B) = -0^m.81$ for the comparison, C_1, (Duerbeck 1975) we obtained the following magnitudes and colours for the individual components of VV Ori:

	Hot component	Cool component
V	5.46	7.88
$(B\text{-}V)$	−0 21	−0 14
$(U\text{-}B)$	−0 92	−0.82

According to Eaton (1975) an interstellar reddening correction of $E(B\text{-}V) = 0^m 05$ is applicable to VV Ori. Assuming the law of interstellar reddening (Allen 1976) to be

holding good, this reddening in $E(B\text{-}V)$ corresponds to a reddening of $E(U\text{-}B) = 0^m 04$ and $A_v = 0^m.16$. Correcting the above derived magnitudes and colours for the reddening, one gets

	Hot component	Cool component
V_0	5.30	7 72
$(B\text{-}V)_0$	-0.26	$-0 19$
$(U\text{-}B)_0$	-0.96	-0.86

The above corrected $(B\text{-}V)_0$ of the primary component corresponds to a spectral type of either $B2$ V (Allen 1976) or $B1$ V (Popper 1980), giving it an average spectral type $B1.5$ V. For such a star the $(U\text{-}B)_0$ would be $-0 96$ (Allen 1976; Schmidt-Kaler 1982) which is the same as that obtained above. Hence both the derived $(B\text{-}V)_0$ and $(U\text{-}B)_0$ colours give a consistent spectral type of $B1.5$ V to the primary component The average temperature of a $B1 5$ V star would be $25,500 \pm 800$ K (Allen 1976, Popper 1980; Schmidt-Kaler 1982), which is the same as the fixed parameter, $T_{e,h}(25,000\,\text{K})$ used for solving the light curves. This confirms that our analysis with fixed $T_h(25,000\,\text{K})$ and $q(0\ 4172)$ yielded results akin to the reddening free data.

The derived $(B\text{-}V)_0$ of $-0^m.19$ of the secondary component corresponds to a spectral type of $B4$ V (Allen 1976), and its derived temperature of $15,580$ K suggests a spectral type of $B5$ V (Allen 1976, Popper 1980). Thus both the $(B\text{-}V)_0$ colour and temperature give a consistent spectral type of $B4\text{-}5V$ to the secondary component. However, for such a star, the $(U\text{-}B)_0$ should be $-0^m.60$ (Allen 1976, Schmidt-Kaler 1982), but its derived $(U\text{-}B)_0 = -0^m.86$ Hence the secondary component appears to be a $B4\text{-}5V$ star with a UV excess of about $0^m 3$ In view of their small sizes and low luminosities (section 5) the possibility of the colours of these components corresponding to those of supergiants is not considered According to Popper (1993) the properties of the components of VV Ori correspond well with those of the main-sequence stars of types $B1$ and $B5$. Eaton (1975) classified the primary as $B0$ V to $B1.5$ V while the secondary in the middle B range and concludes that 'VV Ori seems to be a reasonably normal main-sequence pair'. Chambliss (1983) suggested that VV OriA is a $B1$ V star Duerbeck (1975) derived a spectral type of $B1$ V for the primary and $B5\text{-}9$ V for the secondary components. Hence our derived spectral types of the components $(B1.5$ $V + B4\text{-}5$ $V)$ agree quite well with those of other investigators except that the secondary appears to have a UV excess of $0^m.3$. Since the standard magnitudes and colours of the comparison star used by Chambliss & Davan (1987) are not available, we could not get the magnitudes and colours of the components of VV Ori in $H\alpha$ pass bands.

5. Absolute elements

Taking the amplitudes of the radial velocity curves as $K_1 = 136 \pm 6$ and $K_2 = 326 \pm 7$ km/sec from Popper (1993) and $i = 86.09°$ from the present study (Table 2, col. 2) one gets the masses of the individual components of VV Ori as $m_h/m_\odot = 10.81 \pm 0.42$ and

$m_c/m_\odot = 4.51 \pm 0\,41$ and $A/R_\odot = 13.605 \pm 0\,031$ Combining these values with those of r_h, r_c, T_h and T_c, we obtained the following sizes, luminosities, bolometric and visual magnitudes

	Hot component	Cool component
$R/R_\odot$	$5.03 \pm 0\,03$	2.43 ± 0.02
$\log L/L_\odot$	$3.948 \pm 0\,044$	$2.493 \pm 0\,023$
M_{bol}	-5.18 ± 0.11	-1.54 ± 0.06
M_v	-2.59 ± 0.11	-0.10 ± 0.06

In calculating M_v, we used the bolometric correction of $-2^m 59$ and $-1^m.44$ for the hot and cool components respectively (Popper 1980). Applying the interstellar absorption of $A_v = 0^m.16$, the distance of VV Ori was found to be $368 \pm 10\,pc$

6. Component properties and comparison with other similar systems

From a plot of the positions of the two components on observed ZAMS in Fig 2 (Morton & Adams 1968) it is noticed that the primary component lies slightly above and the secondary component slightly below or on the ZAMS. Chambliss (1984) found the larger component (primary) to be normal for a spectral type of $B1\ V$ and found it to be fairly close to the ZAMS Eaton (1975) concludes that VV Ori seems to be a reasonably normal main-sequence pair and when plotted on the observational ZAMS the primary lies a little above the main-sequence and the secondary lies slightly below.

In order to compare the above properties of VV Ori with other detached systems having B type components, we plotted in Fig 2 the positions of a few systems as given in tables 2 and 4 of Popper (1980) From this we notice that except a few primaries, notably no. $14\ (\chi^2\,Hya)$, all the other components lie either on the ZAMS or very near to it. A little adjustment in the scale of either the derived parameters or the observed ZAMS in the $\log T_e$ range of 4.3 to 4 05 may make most of the systems to fall on the ZAMS. For ready reference, the list of systems given by Popper (1980) and used in this study are given in Table 4

In Figs 3, 4 and 5 (solid lines) we have plotted the relations of $\log L$, $\log R$ and $\log T_e$ with respect to log mass of the normal main-sequence stars (Allen 1976) In these figures, in addition to the positions of the components of VV Ori, we have also plotted the positions of other detached systems given in Table 4. From these plots one can see that the primary component of VV Ori is overluminous, hotter and a little undersized for its mass. In the case of the secondary component it is seen that while its luminosity is consistent with its mass, its radius is smaller and the temperature is higher for its mass. However from a comparison of the positions of the other detached systems in these plots, it is apparent that in addition to getting more accurate elements, there is a need for either refixing the scales of the observed $\log L$, $\log R$ and $\log T_e$ or modifying the models and getting new theoretical relations. Unless this is done, one cannot come to any conclusion regarding the properties of the components of VV Ori and compare them with other detached systems.
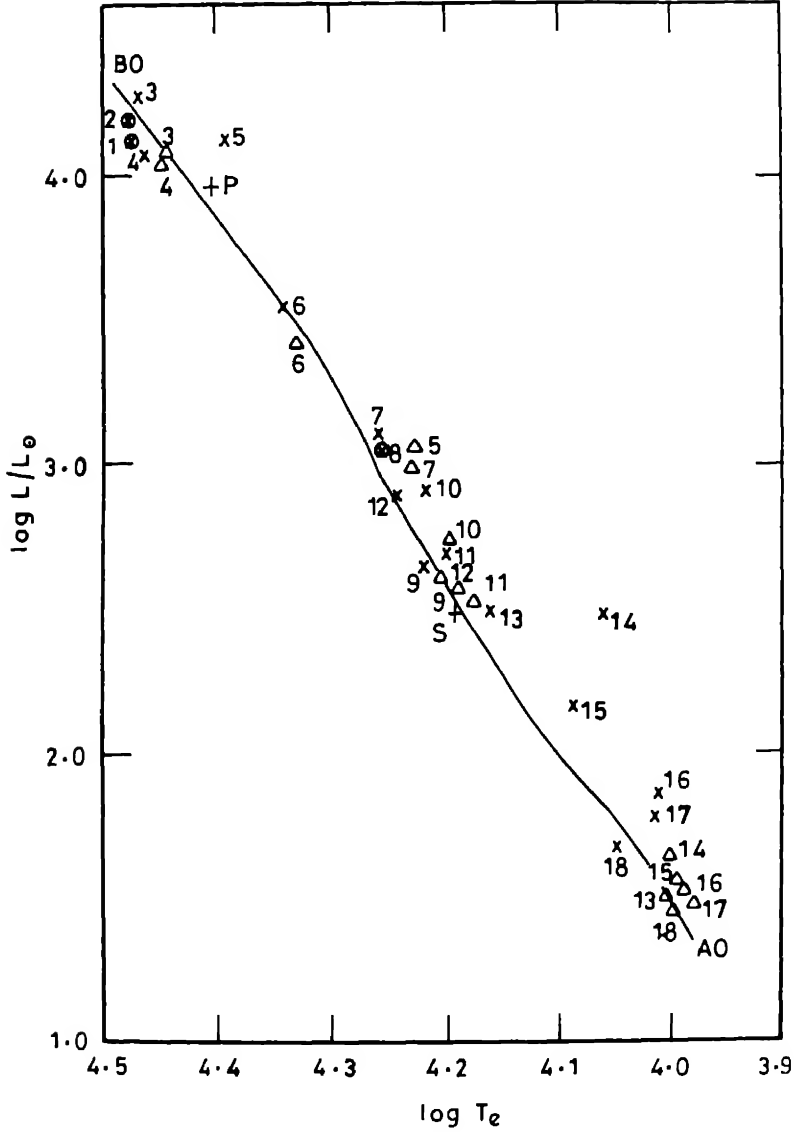
Figure 2. VV Ori Plot of log $L/L_\odot$ versus log T_e. The solid line represents the observed ZAMS (Morton & Adams 1968). The primary (P) and secondary (S) components of VV Ori are indicated as '+' Components of other detached systems are shown as 'x' (P) and 'Δ' (S) Numbers represent the names of the systems given in Table 4 '⊗' represent both the primary and secondary components of a system

7. Evolution

With a view to study the evolutionary status of the components of VV Ori, we used the evolutionary tracks computed by Schaller *et al.* (1992) for stars of Pop I composition. These evolutionary tracks for stars of initial masses of 10 8 and 4.5 in solar units are

ble 4. VV Ori List of detached systems used in Fig. 2

ɔ	Name	$\log m_1$	$\log L_1$	$\log R_1$	$\log T_1$	$\log m_2$	$\log L_2$	$\log R_2$	$\log T_2$
	Y Cyg	1.220	4 45	0.780	4.485	1 220	4.45	0 780	4 485
	V478 Cyg	1 190	4 62	0.860	4.485	1 190	4 62	0 860	4 485
	V453 Cyg	1.160	4 69	0.930	4 470	1 050	4 20	0 730	4 445
	CW Cep	1 070	4 28	0 730	4 470	1 040	4 13	0.700	4 445
ɪ	α Vir	1 030	4 33	0 910	4 390	0 830	3 16	0 640	4 230
ɪ	QX Car	0 960	3 59	0 630	4.340	0 930	3.48	0 600	4 330
ɪ	V539 Ara	0 790	3 26	0 640	4 255	0 720	3 02	0.570	4 230
℥	CV Vel	0 780	3 19	0 610	4 255	0.780	3 19	0.610	4 255
ɪ	DI Her	0 720	2 65	0 410	4.220	0.660	2.52	0 410	4 190
ɪ	U Oph	0 710	2 90	0 540	4.220	0.660	2 74	0.490	4 200
ɪ	V760 Sco	0 700	2 71	0.480	4 200	0.670	2 53	0 430	4 18
℥	AG Per	0.660	2 89	0.480	4 245	0 610	2 62	0 410	4 210
℥	ξ Phe	0 593	2 50	0 455	4 160	0 405	1 51	0 267	4 005
℥	χ^2 Hya	0 558	2 49	0 642	4.063	0 422	1 64	0 334	4.005
℥	AS Cam	0 520	2 17	0 431	4 088	0 400	1 56	0 301	4.001
℥	V451 Oph	0 444	1 86	0.423	4.015	0 373	1 54	0 326	3.985
℥	RX Her	0 439	1.79	0 387	4.015	0 367	1 48	0 292	3 985
℥	AR Aur	0.394	1 67	0.262	4 048	0 360	1 46	0.262	3 997

hown in Fig. 6, which is a plot of $\log L/L_{\odot}$ versus T_e. In the same diagram, the sochrone for an age of 10 million years is also shown This isochrone was obtained by nterpolation between the evolutionary tracks of Schaller *et al.* (1992) based on points f corresponding evolutionary status One can see from this figure that the primary has volved from its initial position along the $10.8 m_{\odot}$ track The secondary component is till unevolved and lies at the foot of the track of a 4 5$m_{\odot}$ star with a slightly lower uminosity. Both the components satisfactorily fit the isochrone of 10 million years and ience we conclude that the age of VV Ori is 10 ± 1 million years

8. Discussion

The *UV* excess of about $0^m.3$ found for the secondary component may be explained is due to hot gases surrounding this component, the source of which might be the gases xpelled by the primary during its present evolution. Comparing the observed fracional radii of 0.370 and 0.178 of the primary and secondary components with their critical Roche lobes of 0.457 and 0.299 respectively, (for a mass-ratio of 0.42) (Plavec & Kratochvil 1964), it is found that these components are filling 80% and 60% of their respective Roche lobes. Even though any stellar activity like gas streams etc., are not generally expected in detached systems, a slightly bigger fractional radius (of about).01) obtained for *U* pass band in our analysis suggests some form of gases or gaseous streams in the system From their studies of VV Ori light curves, Duerbeck (1975) and Giuricin *et al.* (1983) had also arrived at similar conclusions.

Even though the geometrical and absolute elements of VV Ori are now well established, a few peculiarities are still left unexplained. The influence of mutual interactions on the evolution of the system should be carefully estimated.
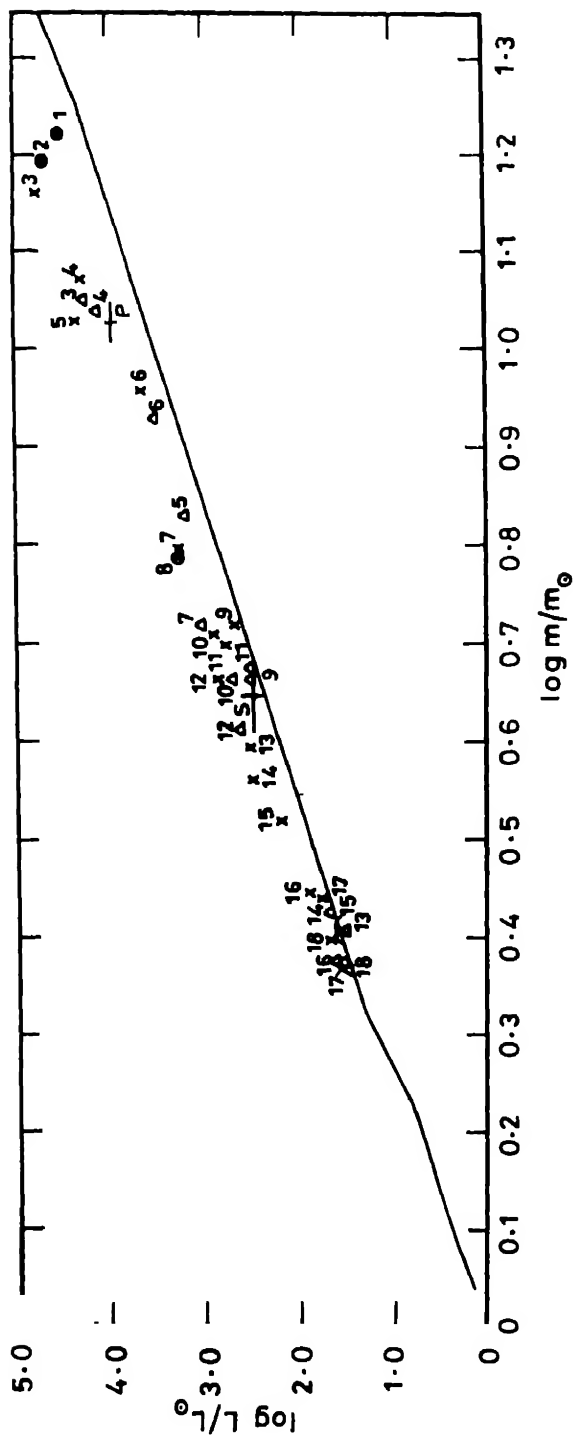
Figure 3. VV Ori Plot of $\log L/L_\odot$ versus $\log m/m_\odot$ The solid line represents the relation for normal stars (Allen 1976) The primary (P) and secondary (S) components of VV Ori are shown in the figure with error bars Other details are the same as for Fig 2
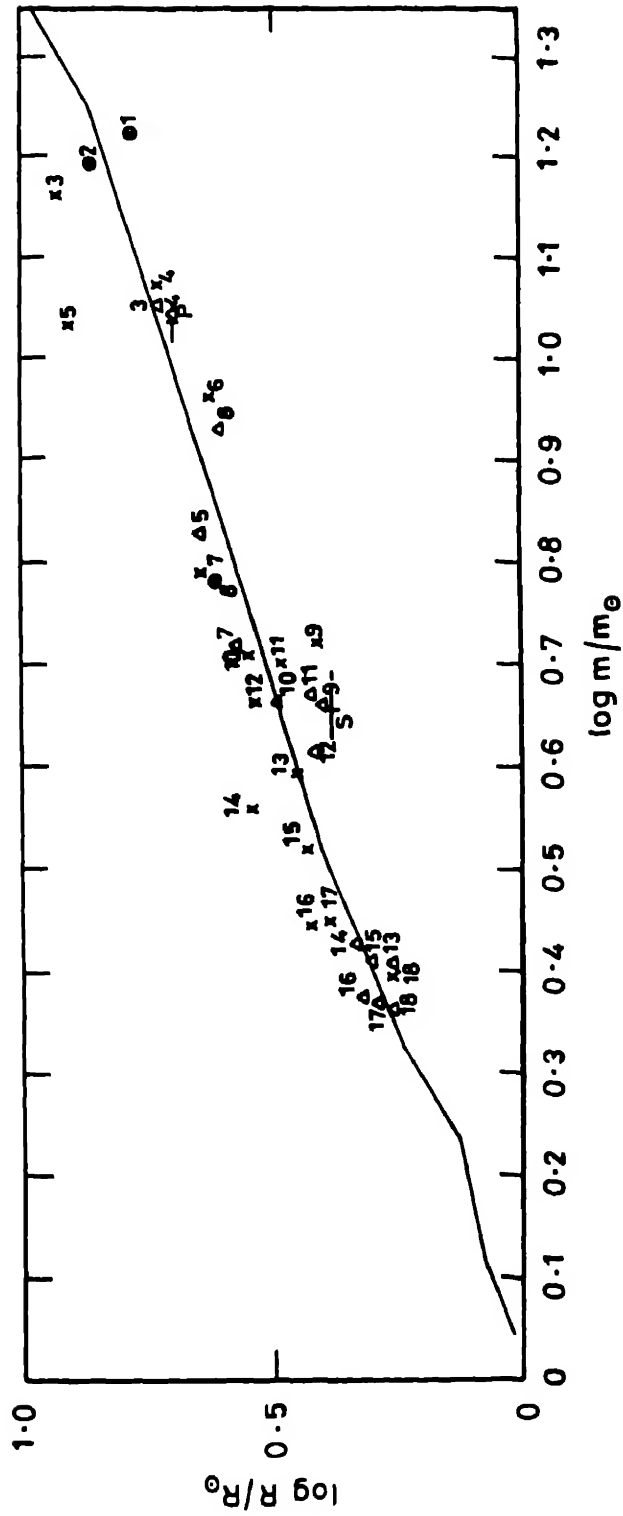
Figure 4.   VV Ori. Plot of $\log R/R_{\odot}$ versus $\log m/m_{\odot}$. Details are the same as for Fig 3

M. B. K. Sarma & P Vivekananda Rao
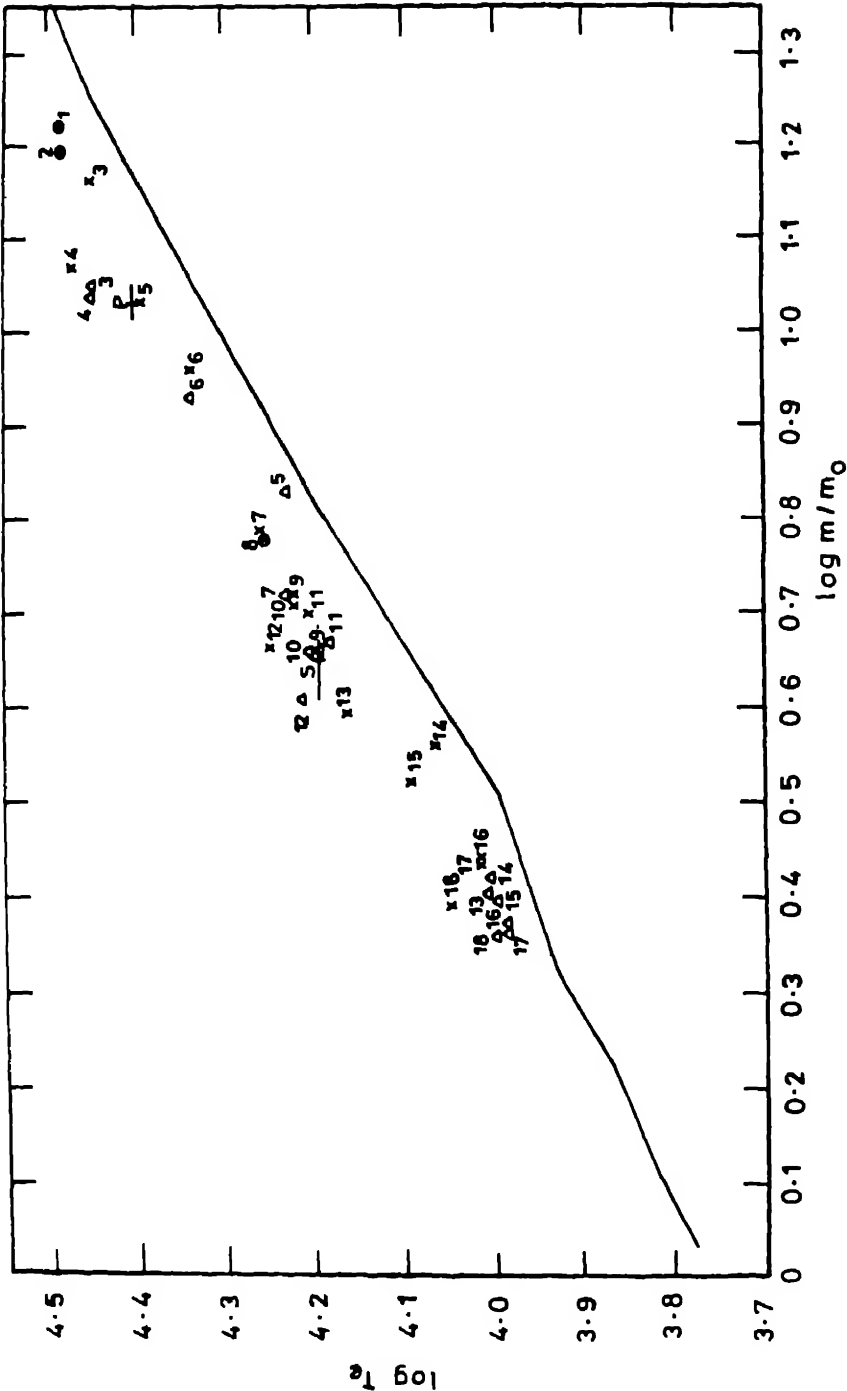
Figure 5. VV On Plot of $\log T_e$ versus $\log m/m_O$ Details are the same as for Fig 3
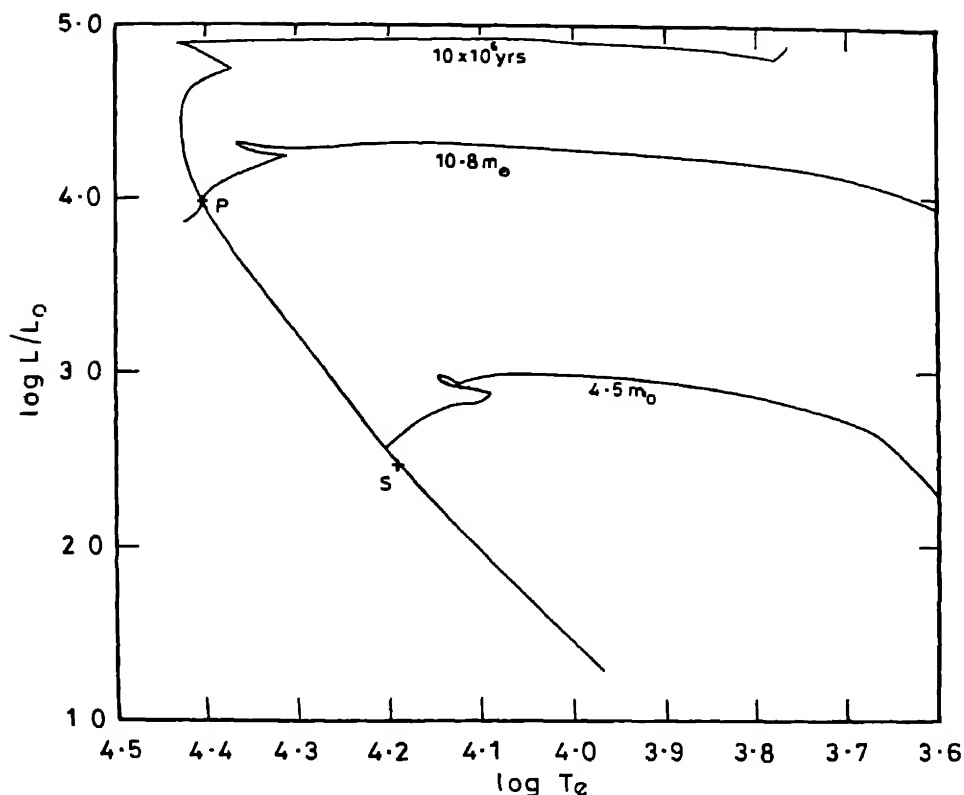
Figure 6. VV Ori Evolutionary tracks of stars of initial masses 10.8 and 4 5 in solar units. These tracks were computed by Schaller *et al* (1992) for stars of Pop I composition The isochrone for 10×10^6 yrs is also shown in the diagram, the positions of the primary (P) and secondary (S) components of VV Ori are shown as '+'

Acknowledgements

References

Allen, C. W 1976, *Astrophysical Quantities*, 3rd edn., (London The Athlone Press)
Andersen, J 1976, *Astr Astrophys*, **47**, 467
Barr, J. M 1905, *Selected papers, Proc. R Astron. Soc Canada, 1904*, 42
Beltrani, G, Galeotti, P. 1970, *Mem. Soc Astron Ital*, **41**, 167
Budding, E, Najim, N. N. 1980, *Astrophys Space Sci*, **72**, 369
Cester, B., Fedel, B, Giuricin, G, Mardirossian, F., Mezzetti, M. 1978, *Astr Astrophys Suppl*, **33**, 91
Chambliss, C. R., Leung, K. C. 1982, *Astrophys J Suppl*, **49**, 531.

Chambliss, C R 1983, *Astrophys Space Sci* , **89**, 15.

Chambliss, C R 1984, *Astrophys Space Sci.*, **99**, 163

Chambliss, C R , Davan, B M 1987, *Astr. J* , **93**, 950

Duerbeck, H. W 1975, *Astr Astrophys Suppl.*, **22**, 19

Eaton, J A 1975, *Astrophys J* , **197**, 379.

Giuricin, G., Mardirossian, F , Mezzetti, M , Chambliss, C. R 1983, *Astr. Astrophys Suppl* , **51**, 111.

Gryger, J. 1972, *Bull astr Inst Csl* , **23**, 157

Lucy, L. B 1968, *Astrophys J.*, **153**, 877.

Morton, D C , Adams, T F 1968, *Astrophys J* , **151**, 611

Plavec, M , Kratochvil, P 1964, *Bull astr Inst. Csl* , **15**, 165

Popper, D. M. 1980, *A. Rev Astr Astrophys* , **18**, 115.

Popper, D. M. 1981, *Astrophys. J Suppl* , **47**, 339

Popper, D. M 1984, *Astr J* , **89**, 132

Popper, D M 1993, *Publ Astr Soc. Pacific*, **105**, 721.

Russell, H N , Merrill, J E 1952, *Contr Princeton Univ Obs* , *No. 26.*

Schaller, G., Schearer, D , Meynet, G., Maeder, A. 1992, *Astr Astrophys Suppl* , **96**, 269

Schmidt-Kaler, Th 1982, in *Landolt/Bornstein, Numerical data and functional relationship in Science and Technology*, Eds K Scaifers & H H. Voigt, (Berlin: Springer-Verlag), New Series, Group VI, Volume 2(b), p 453

Struve, O , Luyten, W. J 1949, *Astrophys J* , **110**, 160

Wilson, R E., Devinney, E J. 1971, *Astrophys J* , **166**, 605

Author Index

Subject Index

Journal of Astrophysics and Astronomy

Volume 16

1995

Journal of Astrophysics and Astronomy

Subscription Rates
(Effective from 1989)

All countries except India	1 year	3 years	5 years
(Price includes AIR MAIL charges)	US$75	$200	$300
	1 year	10 years	
India	Rs 75	Rs 400	

All correspondence regarding subscription should be addressed to **The Circulation Department** of the Academy

Editorial Office

Indian Academy of Sciences, C V Raman Avenue,
P B No 8005, Bangalore 560 080, India

Telephone (080) 3342546
Telex   0845-2178 ACAD IN
Telefax   91-80-3346094

Contents—Volume 16

Number 1

Number 2

429

Numbers 3 & 4

Journal of Astrophysics and Astronomy

Instructions to Authors

Journal of Astrophysics and Astronomy publishes papers on all aspects of Astrophysics and Astronomy, including instrumentation. Papers should contain results of original research not previously published nor under consideration for publication elsewhere All papers are refereed. There are no page charges.

Three copies of each paper should be submitted Manuscripts should be typewritten double-spaced on one side of the paper, with a margin of 3 cm on the left side. Authors must ensure that annotation of the typescript is such as to give the printer sufficient guidance in setting the paper, with special reference to ambiguous and unusual symbols, sub- and superscripts and the placing in the text of diagrams and tables. Each paper should be provided with a concise abstract and appropriate key words. The first page of the manuscript should contain the title, the name(s) and the institutional affiliation(s) of the author(s), a running title and an address to which the proofs are to be sent

References should be typed on a separate sheet at the end of the text and arranged alphabetically and chronologically They should follow the format prescribed by the International Astronomical Union, which is set out in I A. U Trans XIIC

Tables and figures should be numbered consecutively and have self-contained headings and legends Each table should be typed on a separate page and numbered in sequence with Arabic numerals Line drawings must be made in Indian ink and should not exceed twice the final size. Authors are requested to pay adequate attention to thickness of lines, sizes of points and adequate spacing of shaded and dotted areas The words on a drawing should be in upper and lower case characters

Photographs for preparation of half-tone plates, should be glossy prints of high contrast These should be unmounted and trimmed precisely at right angles. Copies of such prints are required for the use of the referees and editors

Authors are requested to exercise utmost care in preparation of the manuscripts so that there is little need to incorporate alterations at the proof-reading stage. Proofs should be returned within three days of receipt

Contents